CHALMERS
UNIVERSITY OF TECHNOLOGY

SAAB

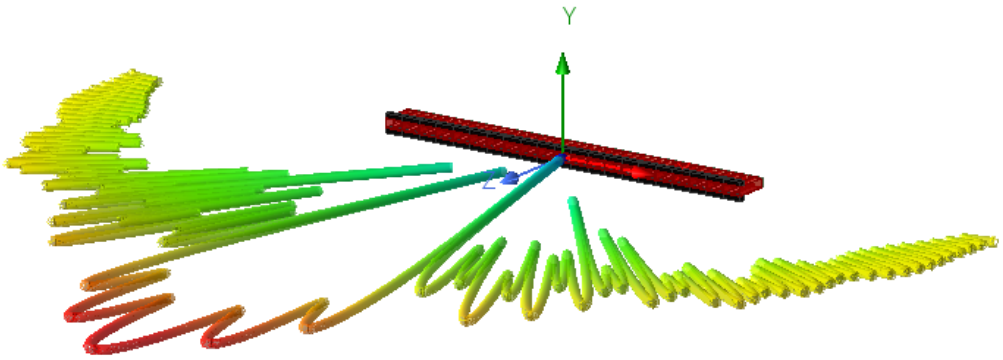

Antenna Obstruction Cloaking

Theoretical Study of Electromagnetic Cloaking and Anti-Scattering Methods on Cylindrical Antenna Obstructions @ X-Band

Master's Thesis Project Report in Electrical Engineering

DENNIS LUNDQVIST AND AGNES WILHELMSSON

DEPARTMENT OF ELECTRICAL ENGINEERING
CHALMERS UNIVERSITY OF TECHNOLOGY
Gothenburg, Sweden 2024
www.chalmers.se

Master's thesis project report 2024

Antenna Obstruction Cloaking

Theoretical Study of Electromagnetic Cloaking and Anti-Scattering Methods on Cylindrical Antenna Obstructions @ X-Band

Master's Thesis Project Report

DENNIS LUNDQVIST AND AGNES WILHELMSSON

CHALMERS
UNIVERSITY OF TECHNOLOGY

Department of Electrical Engineering
Chalmers University of Technology
Gothenburg, Sweden 2024

Antenna Obstruction Cloaking
Theoretical Study of Electromagnetic Cloaking and Anti-Scattering Methods on Cylindrical Antenna Obstructions @ X-Band
DENNIS LUNDQVIST AND AGNES WILHELMSSON

Supervisor: Andreas Wikström, Saab AB
Examiner: Rob Maaskant, Electrical Engineering

Master's thesis project report 2024
Department of Electrical Engineering
Chalmers University of Technology
SE-412 96 Gothenburg
Sweden
Telephone +46 31 772 1000

Cover: Realized gain of a 1×21 element open-ended ridge waveguide antenna with uniform taper in HFSS as a 10 cm diameter metal pole directly in front of the antenna at a distance of 1 m obstructs it.

Typeset in LaTeX
Gothenburg, Sweden 2024

Antenna Obstruction Cloaking
Theoretical Study of Electromagnetic Cloaking and Anti-Scattering Methods on Cylindrical Antenna Obstructions @ X-Band
DENNIS LUNDQVIST AND AGNES WILHELMSSON
Department of Electrical Engineering
Chalmers University of Technology

Abstract

This report theoretically investigates different techniques of electromagnetic cloaking and anti-scattering on a cylindrical metallic object, e.g. a cord or a pole, along the vertical axis obstructing a vertically polarized antenna (i.e. a worst case scenario in terms of scattering) at 9.5 GHz/X-band. Multiple 'shells' around the pole obstructions have been designed with different materials and shapes, for simulations around metallic poles of diameters 5 cm and 10 cm at different distances from the antenna. A total of 4 designed shells have been simulated in Ansys 3D High Frequency Simulation Software (Ansys HFSS) in order to evaluate their performance in terms of realized gain and average sidelobe level in the antenna's forward direction for different steering angles in the H-plane/azimuth plane. The evaluated shells around the poles were 1) a layer of thin radiation absorbent material made out of ferrites (narrowband absorbent), 2) a rhomb made out of PEC, 3) a rhomb made out thick radiation absorbent material with increasing conductivity (wideband absorbent) and 4) a rhomb made out of PEC (e.g. shell 2) supplemented with a dielectric outer edge and PEC strips around the circumference of the structure. Additionally, the project evaluated the requirements of meta-material cloaks and how to design them in practice. Although meta-materials have been a hot topic the recent years for electromagnetic cloaking, the thesis concluded after investigation that far more simple solutions that yield promising results exist. In terms of average sidelobe level in the antenna's forward direction shell 2 of the PEC rhomb performed the best, with the second best realized gain behind shell 4 that successfully guided electromagnetic waves around the obstruction to the price of average sidelobe level. For solving the described problem scenario, the thesis recommends to slightly redesign shell 4 such that its outer dielectric rhomb point tips have a relatively lower permittivity as this likely will both effectively reduce the average sidelobe level and increase the realized gain for steering angles in the H-plane.

Keywords: antenna obstruction cloaking, 9.5 GHz, X-band, electromagnetic cloak, anti-scattering, radiation absorbent, meta-material.

Acknowledgements

For providing us with indispensable counsel and recommendations during the thesis, we would like to thank our examiner Rob Maaskant. Further, on behalf of the continuous help throughout the thesis including project advice and invaluable guidance regarding antennas, absorbents and Ansys HFSS, we would like to direct a big thank you to our supervisor Andreas Wikström. We would also like to thank our employer Mats Högberg and Saab AB as a whole for granting us the opportunity to pursue this project, for hosting us and for providing us with the required equipment in order to succeed with the thesis. Additionally, we would like to express gratitude towards the colleagues at the Kallebäck office for showing an interest in our project and coming with useful suggestions, and to Ansys' Alireza Kazemzadeh for on multiple occasions providing us with software support.

Dennis Lundqvist
Agnes Wilhelmsson
Gothenburg, May 2024

List of Acronyms

Below is the list of acronyms that have been used throughout this thesis listed in alphabetical order:

ABS	Absorbent
AESA	Actively electronically steered array
Ansys HFSS	Ansys High Frequency Simulation Software
ASLL	Average sidelobe level
CPU	Central processing unit
E-field	Electric field
FE-BI	Finite element boundary integral
H-field	Magnetic field
IE	Integral equation
IL	Insertion loss
MATLAB	Matrix Laboratory software
PEC	Perfect electric conductor
PML	Perfectly matched layer
Radar	Radio detection and ranging
RAM	Random access memory
RF	Radio frequency
RG	Realized gain
RL	Return loss
S-parameter	Scattering parameter
SRR	Split ring resonator
TE	Transverse electric
TM	Transverse magnetic

Contents

1
Introduction

In today's radar systems, antennas are integrated in structures where objects in the antenna's vicinity affect its gain, sidelobes and overall performance. Antenna cloaking is a technique where objects in the antenna's locality are bypassed through smart designs to reduce the object's affect on the antenna's electromagnetic field. These designs usually aim to achieve anti-scattering and invisibility cloaking characteristics. The interest in invisibility cloaks has been growing in recent years, as material manufacturing has become more sophisticated and papers on realizable invisibility cloaks have been published [1][2]. An implementation of anti-scattering is the use of multi-layer structures or absorbent materials for scattering cancellation. When cloaking an object the incident electromagnetic waves are, instead of being scattered on the obstructed surface, guided around the obstruction with meta-materials. Meta-materials posses electromagnetic properties which can not be found in nature, but can be fabricated with the use of dielectrics and metals [3][4]. Previous works of anti-scattering and invisibility cloaking techniques [1][2][5] have shown promising approaches to reduce the affect of obstructing objects, where scattering is reduced and cloaking introduced.

1.1 Background

The specific problem scenario that has been investigated in this project is a cord or a pole obstructing the view of an array antenna. For instance, obstructing cords and/or poles are often problematic on ships, as shown in Figure 1.2, and in cases where they can not be removed it is desirable to remove the obstructions' negative impact in terms of loss of realized antenna gain and scattering at the obstruction. Hence, in order to evaluate advantageous solutions for cloaking of thin cylindrical obstructions, different techniques have been theoretically investigated for cloaking of metallic poles of diameters 5 cm and 10 cm at different distances from an antenna. Figure 1.1 specifies the simulated setup in this report, showing the problem setup with a metallic pole placed in the vicinity of an array antenna to the left and an investigated possible solution where some designed material coverage has been placed around the obstruction to the right. For different cases of material, distance, angles and antenna tapers, interesting results were the antenna realized gains and average sidelobe levels for different beam steering angles. In order to investigate a worst case scenario in terms of scattering at the obstruction, the simulation setup shown in Figure 1.1 with the vertical pole was evaluated using a designed vertically polarized array antenna and scanning in the H-plane/azimuth plane. However, for

more general results of how to solve the specific problem scenario in practice, the different cloaking techniques were somewhat evaluated for horizontal polarization as well. Further, as it was desired to obtain knowledge about the cloaking performances at X-band frequencies, simulations were made for the frequency 9.5 GHz.

Figure 1.1: Top view schematic of the situations to be analyzed, e.g. an obstruction without or with material coverage in the vicinity of an array antenna.

Figure 1.2: Visualization of cords/poles mounted on a ship such that an antenna's view will be obstructed. The image shows Saab AB's Visby-Class Corvette K35 [6].

1.2 Purpose

The master's thesis sought to theoretically examine different possibilities for antenna obstruction cloaking for cylindrical obstructions such as cords and/or poles. Different solutions were evaluated using Ansys' electromagnetic simulator "3D High Frequency Simulation Software" (Ansys HFSS) and "Matrix Laboratory" (MAT-

LAB). The work was carried out in collaboration with Saab AB during 15 Jan 2024 to 2 June 2024, and the following stages were included in the thesis:

- Literature study of relevant theory and previous works
- Choice of methods for antenna obstruction cloaking
- Modeling and simulation in Ansys HFSS
- Coding/post-processing of data in MATLAB
- Report writing and presentations

1.3 Goals

The aim of the project was to theoretically analyze different cloaking techniques on cylindrical objects obstructing an X-band antenna in terms of antenna realized gain and average sidelobe level as both tapering and lobe steering is applied on an array antenna, in order to gain knowledge about how to cloak cords and/or thin poles from an antenna most efficiently in practice.

1.4 Limitations / Demarcations

A limitation of the project is that it was performed with software and simulations such that the obtained results may not be entirely reliable as no physical measurements were done to verify them. Any demarcations apart from this are described below.

- The antenna performance was evaluated through analysis of the realized gain and antenna pattern only in a single plane, e.g. only in the elevation angle $\phi = 0°$ as the antenna beam was steered in the azimuth plane, because the analysis would have become complicated and immense if done for all angles/in 3D. Additionally, data was only gathered in one slice/plane as it greatly reduced the time of simulation, data export and post-processing. Intuitively, this demarcation would still allow for the general problem to be evaluated, as investigation of another elevation angle $\phi \neq 0°$ mostly would imply that the obstruction is hit at an angle by a slightly lower realized gain radiation pattern compared to the main beam at $\phi = 0°$. Hence, relative to the unobstructed or uncloaked cases the results would likely be similar.
- For analysis of the effect of changing the antenna excitation only a uniform taper and a Taylor taper were implemented as the aim was to investigate the performance without and with reduced sidelobes, e.g. and *not* to calibrate or fine-tune the antenna to obtain max realized gain or, perhaps, an excitation null in a desired direction.
- In order to significantly reduce simulation time, simulations were made with the pole obstruction directly in front of the antenna (e.g. not at an angle) after which the antenna beam was steered over the pole in MATLAB. More interesting data could have been collected if the pole was simulated at different angles (as, for instance, having the pole at a certain angle from the antenna centre vs steering the beam away from the pole by the same angle will not

yield the same results due to the changing antenna pattern as the beam is steered), however it was determined that the general idea would be obtained. To specify, simulating the pole at different angles in Ansys HFSS would require new simulations, whereas steering of the beam in MATLAB could be done in an instance.
- For calculations of the average sidelobe level for different steering angles in the H-plane, only the antenna diagram in the forward direction, i.e. for the angles $-90° \leq \theta \leq 90°$, was used as it was determined that it would be sufficient to analyze the behaviour around the obstruction. However, more interesting results could have been obtained if the simulated data had been exported for the full H-plane. Instead, the report investigates the results for the full H-plane only for some simulated data in order to visualize the effect in the back direction.

1.5 Ethical considerations

This master's thesis mainly focused on the functionality and performance of antennas and their use in radar systems. Radar systems are today in widespread service in the arms, cars and geoscience industries, to name a few. As radar systems are used for both defensive and offensive purposes in the arms industry, one could argue for positive and negative consequences from an ethical viewpoint, in the case of further development. From a sustainability perspective, obstruction cloaking can prevent changes or reconstruction of the surrounding environment of an antenna, and thereby save resources.

1.6 Project overview

In this report, Chapter 2 describes the relevant theory for the project, including the fundamentals of antennas and radiation absorbents as well as a short introduction of the implemented software Ansys HFSS. Next, Chapter 3 details the methodologies of the different stages of the project, including the design of a 1×21 waveguide element array antenna in Ansys HFSS and the setup of the implemented antenna and obstruction environment for simulation of metal pole obstructions with diameters 5 cm and 10 cm at the distances 1 m, 2 m, 3 m, 4 m, 5 m, 10 m, 20 m and 30 m from the array antenna without and with cloaking shells placed around the obstructions. Further, Chapter 3 details the designs of the different implemented shells employed for electromagnetic cloaking and anti-scattering and a description of the extensive amount of MATLAB code that was written for post-prossesing and presentation of the many variations of simulated embedded array antenna realized gain radiation patterns in order to obtain the results of interest. Lastly, Chapter 4 analyzes the results of the different designed shells and compares them to each other, the uncloaked case and the unobstructed case, and Chapter 5 presents the final conclusions of the thesis.

2

Theory

In this chapter, theory relevant for the project is explained. More specifically, Section 2.1 describes the fundamentals of antennas, Section 2.2 describes the relevant theory for the implemented radiation obstruction cloaking and anti-scattering techniques in this project, and Section 2.3 gives a short introduction of the used simulation software Ansys HFSS.

2.1 Antenna fundamentals

Antennas transmit or receive electromagnetic waves propagating at the speed of light. Electromagnetic waves are created by accelerating electrically charged electrons and they transport energy in terms of electromagnetic radiation or light. Radiation refers to the part of an electromagnetic field that radiates into infinite space, decreasing inversely in intensity by the square law of power. There is a link between electromagnetic waves and electricity and magnetic waves and magnetism. For instance, electromagnetic waves can be induced and formed by a changing magnetic field (and vice versa), or electricity and magnetism can be static, e.g. like the energy making a persons hair stand on end as a balloon is rubbed on it, or the energy that makes a magnet stick to the refrigerator, respectively. The electromagnetic waves move similar to mechanical waves, e.g. like waves in water with crests and troughs, however they differ as they do not require a physical medium to propagate and instead move through air, solid materials and vacuum. This is possible as the electromagnetic radiation is a stream of the mass-less particles called photons, such that the momentum is carried through physical media. For instance, visible light is a small part of the electromagnetic spectrum and it has both particle-like and wave-like properties [7].

In this section, the fundamentals of antennas are explained, including the basics about radar, frequencies and applications in Section 2.1.1, the definitions of an antenna's radiation pattern, sidelobes, grating lobes and beamwidth in Section 2.1.2 and the theory of an antenna's far field and near field in Section 2.1.3. Further, Section 2.1.4.1 specifies an antenna's coordinate system and mathematically describes how to perform lobe steering and beamforming on an array antenna. Additionally, Section 2.1.5 defines an antenna's realized gain and Section 2.1.6 gives examples of typical antenna designs and details how an open-ended waveguide antenna can be designed.

2.1.1 Radar, frequencies and applications

Radar (Radio Detection and Ranging) is a means to detect surrounding objects using radio waves. Through implementing one transmit and one receive antenna, or iteratively transmitting and receiving using the same antenna, reflected/returned radio waves pulsed/sent in a specific direction can be measured and information can be gained about the distance to adjacent objects, and through measuring multiple echos knowledge can be obtained of the velocities and directions of objects [8]. Multiple frequency bands of the electromagnetic spectrum are used for different radar applications. The implemented radio wave frequency depends on the specific requirements of an application, as there is a trade-off between resolution and detection range. As the radio wave frequency is increased, the range resolution of the radar is increased (e.g. its ability to distinguish between adjoining objects is improved), whereas the detection range is decreased due to attenuation in the atmosphere (negatively affecting higher frequency signals more). Hence, lower frequency radars are generally more suitable if a long detection range is required, whereas higher frequency radars are better implemented for more precise measurements (however, the required range resolution can be very application specific). Further, lower frequency signals can penetrate/travel through thicker surfaces than higher frequency signals, which also makes lower frequency radars suitable for applications requiring obstacle penetration (and vice versa) [8].

Table 2.1: IEEE classification of microwave frequencies [9].

Name	**Bandwidth**
HF-band	3–30 MHz
VHF-band	30–300 MHz
UHF-band	300–1000 MHz
L-band	1–2 GHz
S-band	2–4 GHz
C-band	4–8 GHz
X-band	8–12 GHz
Ku-band	12–18 GHz
K-band	18–27 GHz
Ka-band	27–40 GHz
V-band	40–75 GHz
W-band	75–110 GHz
mm-band	110–300 GHz

Another reason for implementing a higher frequency radar is to decrease the required antenna size. For instance, given that an L-band antenna has the same gain as an X-band antenna, the lower frequency L-band antenna will have a larger physical size. Hence, not only is it required to select radar frequency band to obtain the desired range resolution, but also to obtain an acceptable antenna size for its intended application. There are many denoted radar frequency bands ranging from the frequency 3 MHz to 300 GHz, as described by Table 2.1, that are used for different applications. In the frequency range of several hundred megahertz (MHz), the radars have long detection ranges and good obstacle penetration and, hence, are often used for surveillance and air defence. Instead, higher frequency bands

such as the X-band (8–12 GHz) allows for higher range resolutions and can penetrate thin walls, and are thus more suitable for precision applications and simple industrial applications. The highest radar frequencies are often referred to lie in the mm-band (110–300 GHz) as the radars implementing those higher frequencies only can detect objects within millimeter (mm) distances from the radar, although they yield very fine resolution.

2.1.2 Radiation pattern, sidelobes, grating lobes and beam widths

The radiation pattern defines the variation of the power radiated by an antenna with respect to the angle from the from the antenna center in far field. That is, it visualizes the radiation from the antenna as a function of angular coordinates, dominating at greater distances from the antenna unlike the near field radiation which behaviours dominate closer to it. By studying an antenna's radiation pattern it can be visualized where it transmits or receives power. Figure 2.1 shows an example of an antenna radiation pattern in both 2D and 3D, from which the main lobe and the sidelobes of the antenna radiation can be seen, especially by studying the 2D plot in Figure 2.1a obtained as a slice in the xz-plane from the 3D visualization (at elevation angle $\phi = 0°$, following the notation in this report). Sidelobes are created as the contributions from each element in an array antenna are added, and are typically referred to as unwanted radiation in undesired directions, unlike the field strength in the main lobe which is designed to be larger. For array antennas with element spacing of more than (or less than) half a wavelength, some sidelobes will become significantly larger in amplitude and approach the level of the main beam due to spatial aliasing. The grating lobes, as they are denoted, can generally be said to be copies of the main beam, and they can be avoided at the antenna design stage through element spacing of half a wavelength.

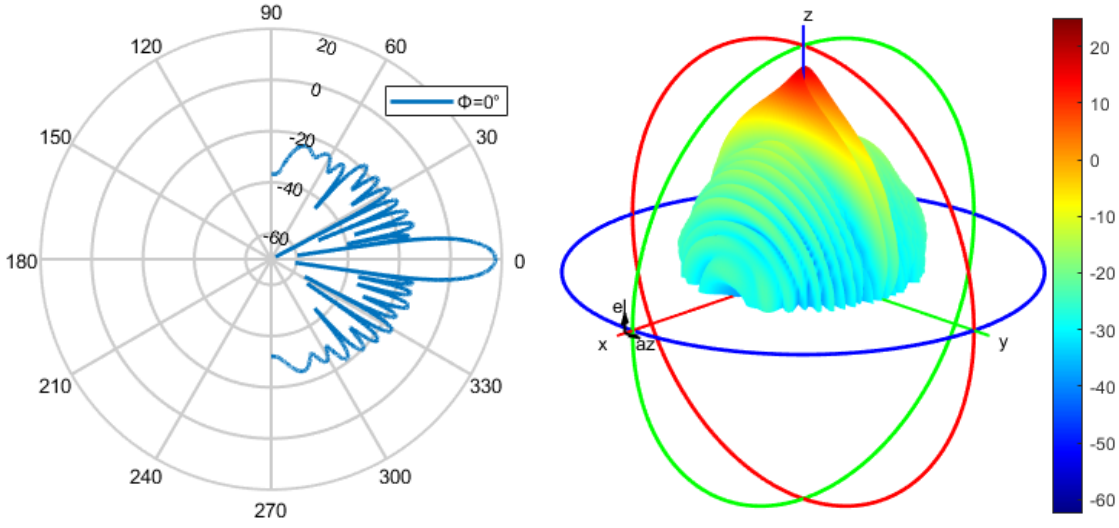

a) 2D. b) 3D.

Figure 2.1: Polar radiation pattern plot in 2D for a slice in the xz-plane (for the elevation angle ϕ=0°) and in 3D (for all elevation angles ϕ).

The main lobe and the sidelobes of an antenna pattern are more clearly defined in Figure 2.2 of the relative realized gain [dB] for the slice $\phi = 0°$, showing the main lobe in blue and the sidelobes in red. Additionally, Figure 2.2 shows the average sidelobe level (ASLL) [dB] which is simply defined as the average of the realized gain for all azimuth angles θ of interest outside of the main lobe. Further, Figure 2.2 shows how the 3 dB beamwidth $\theta_{3\text{dB}}$ [°] is defined, which is simply the width of the main beam as the power of the main lobe has decreased with 3 dB, e.g. the 3 dB beam width $\theta_{3\text{dB}}$ is where the main beam has decreased to half its power in natural values. Typically, as a taper is applied to an array antenna, the width of the main beam increases as the average sidelobe level of the excitation is suppressed/decreased. Hence, the desired average sidelobe level needs to be determined such that the beamwidth is acceptable for a specific application, and vice versa.

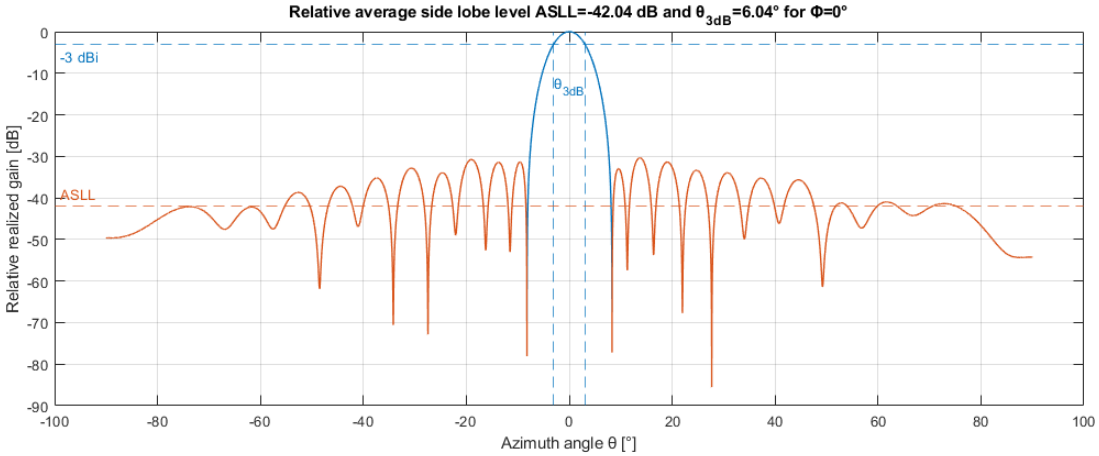

Figure 2.2: Rectangular relative realized gain plot for the slice in the xz-plane (for elevation angle $\phi = 0°$) showing how the average sidelobe level ASLL [dB] and the 3-dB beamwidth $\theta_{3\text{dB}}$ [°] are defined.

2.1.3 Far field and near field

Electromagnetic fields created by a radiating structure (e.g. an antenna) can be categorized into three different field regions. These field regions are the reactive near field, the radiating near field (Fresnel) and the far field (Frauenhofer) which are visualized in Figure 2.3. The boundary or difference between the near field and the far field is loosely defined. However, by defining the radiated electromagnetic waves with a Poynting vector $\vec{S}$ as

$$\vec{S} = \frac{\vec{E} \times \vec{H}^*}{2} \tag{2.1}$$

where $\vec{E}$ is the electrical field and $\vec{H}$ is the magnetic field (and where '$\times$' denotes the cross product and '*' denotes the complex conjugate), the difference between the regions can be seen as the imaginary part and the real part of the Poynting vector are dominant in the near field and far field, respectively. The reactive near field is only in the immediate surroundings of the antenna, typically within a wavelength or two from its center, in which the fields change very quickly, do not propagate and

lose energy very rapidly. Instead, in the radiating near field region, the radiated waves propagate and the angular field distribution depends on the distance R from the antenna centre. Lastly, in the far field region the radiating electromagnetic fields dominate and, in order to simplify calculations, the waves can often be assumed to move as plane waves. The extent R_{NF_1} [m] of the reactive near field region for an antenna can be calculated by

$$R_{NF_1} < 0.62 \cdot \sqrt{\frac{D^3}{\lambda}} \tag{2.2}$$

where R_{NF_1} [m] is the distance between the center of the antenna to the outer boundary of the region, D [m] is the largest dimension of the antenna in meters (e.g. its length) and λ [m] is the wavelength of the radiated electromagnetic waves. Similarly, the region R_{NF_2} [m] of the radiating near field and the region R_{FF} [m] of the far field can be calculated as

$$0.62 \cdot \sqrt{\frac{D^3}{\lambda}} < R_{NF_2} < \frac{2D^2}{\lambda} \tag{2.3}$$

and

$$R_{FF} > \frac{2D^2}{\lambda} \tag{2.4}$$

respectively [10].

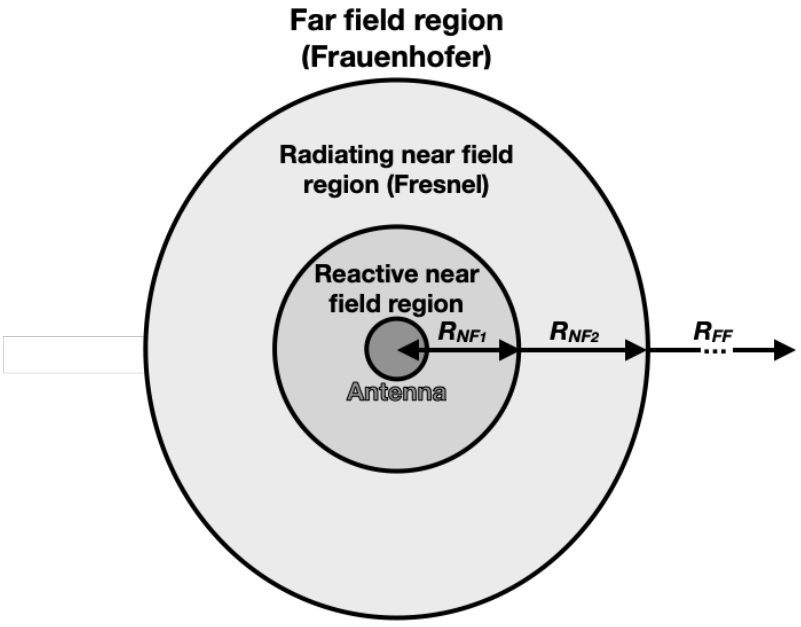

Figure 2.3: Visualization of the three different field regions.

2.1.4 Array antennas, lobe steering and beamforming

An array antenna is an antenna with elements spread out in one or more dimensions. As it is implemented, the direction of the main beam of the antenna can be steered through applying phase shifts between the elements in the array. Additionally, it is possible to shape the antenna beam through modifying the power along the array as desired. Both phase and amplitude modification can be applied electronically on array antennas, in which case the system often is referred to as an actively electronically steered array (AESA). In this section, the coordinate system of an antenna and the polarization of electromagnetic waves are explained, followed by the theory for phase and amplitude modification of array antennas in order to steer the main beam and to shape the radiation pattern, respectively.

2.1.4.1 Coordinate system

Figure 2.4 shows how the coordinate system of an antenna is defined. For $\phi = 0°$, the steering angle $\varnothing$ of the main beam is simplified to $\varnothing = \theta$, i.e. the beam is steered solely in the xz-plane, as visualized in Figure 2.5. As azimuth angles correspond to scanning angles in the horizontal plane, the angle θ can be referred to as azimuth angle and the angle ϕ can be referred to as elevation angle if the coordinate system is rotated such that the xz-plane is parallel to/is aligned with the horizontal plane (which is the chosen rotation of the coordinate system in this project, explained more thoroughly in Section 3.1.2).

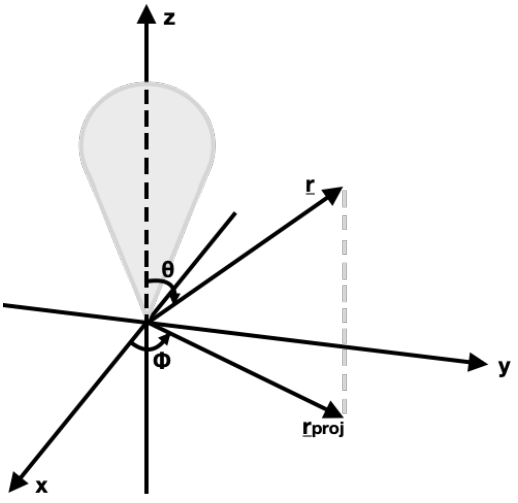

Figure 2.4: Definition of the angles ϕ and θ for an antenna lobe.

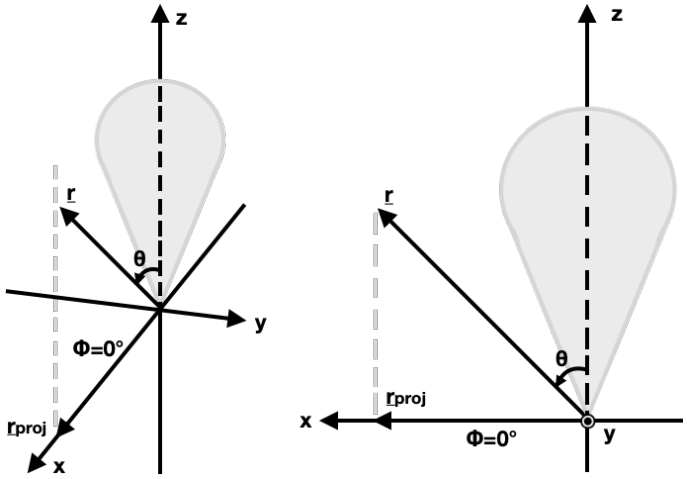

Figure 2.5: Visualization of the antenna lobe steering angle $\varnothing$ of $-90° \leq \varnothing = \theta \leq 90°$ in the xz-plane as the angle $\phi = 0°$. As $\phi = 0°$, the steering angle $\varnothing = \theta$ is defined to be zero as the center of the antenna beam aligns with the z-axis, and $\varnothing$ is defined to increase and decrease as antenna beam moves towards the positive and negative x-axis, respectively. The equivalent illustrations show the situation from two different views.

2.1.4.2 Polarization

Polarization is a measurement of the alignment of the electromagnetic field, for antennas defined as the direction of the electromagnetic field as energy is radiated from it. An antenna receiving polarized electromagnetic waves must employ the same polarization as the signal/as that of the transmit antenna, which can be resembled with throwing a Frisbee at a picket fence, i.e. in one direction it will go through and in another it will be blocked [7]. Hence, it is important to consider the intended orientation of an antenna to be used and, especially, which polarization it should work in and should be designed for. Electromagnetic waves can be linearly or circularly polarized, or anywhere in between, and the desired polarization depends on the application of the antenna system. For instance, linearly polarized antenna systems are cheap to manufacture and typically used for television and communication between stationary users (e.g. two communicating senders/receivers), while circularly polarized systems often are used for communication between moving users as a circularly polarized antenna can receive a circularly polarized signal independent of the rotation of the sender (distinct from linearly polarized antennas and signals). Figure 2.6 visualizes the propagation of electromagnetic waves with linear and circular polarization, which further can be modified and rotated in the coordinate system depending on the application. For the circular polarization shown in Figure 2.6, it should be noted that the actual electric field is a superposition of the visualized linearly polarized fields (e.g. it rotates circularly).

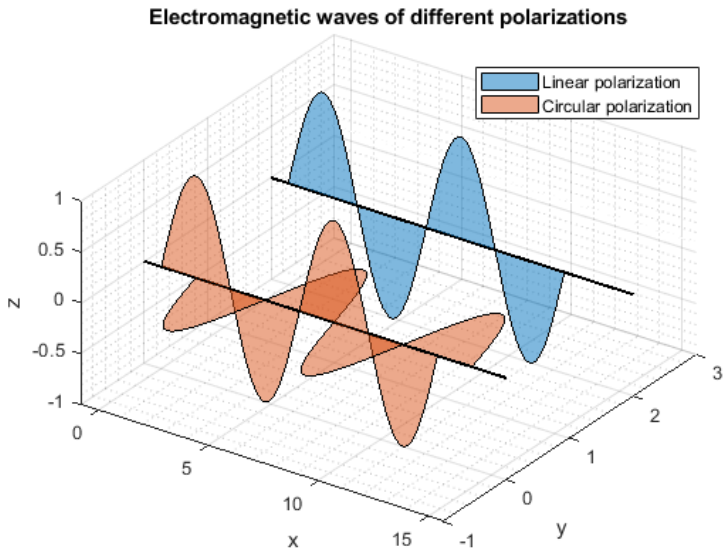

Figure 2.6: Visualization of the propagation of linearly and circularly polarized electromagnetic waves. The x-axis represents time passed as the waves propagate, the shown linear polarization is vertical and the shown circular polarization is right handed (e.g. the wave rotates to the right over time, with a 90° phase shift between the points where the wave lies horizontally and vertically in the coordinate system).

2.1.4.3 Phase and power control of antenna arrays

Figure 2.7 visualizes an array antenna with $M \times N$ elements, where the steering angle $\varnothing$ of the main beam is equal to the azimuth angle θ due to an antenna setup of the main beam centered at elevation angle $\phi = 0°$, as described in Section 2.1.4.1. For beamforming, it is trivial that the same array vector $\vec{A}_{\text{vec}}$ of length N should be applied to all the M rows of elements in an antenna. That is, for an $M \times N$ antenna the array vector should be of length N and should be applied to all M rows (or vice versa, depending on the orientation/definition of the element matrix). Through modifying the array vector $\vec{A}_{\text{vec}}$ in phase and amplitude and applying it to the antenna elements, it is possible to both steer the direction of the main beam and control the gain and sidelobe level of the antenna excitation. As beamforming is explained in this section for a transmitting (Tx) antenna, it follows that similar, or reverse, methods can be used for a receiving (Rx) antenna.

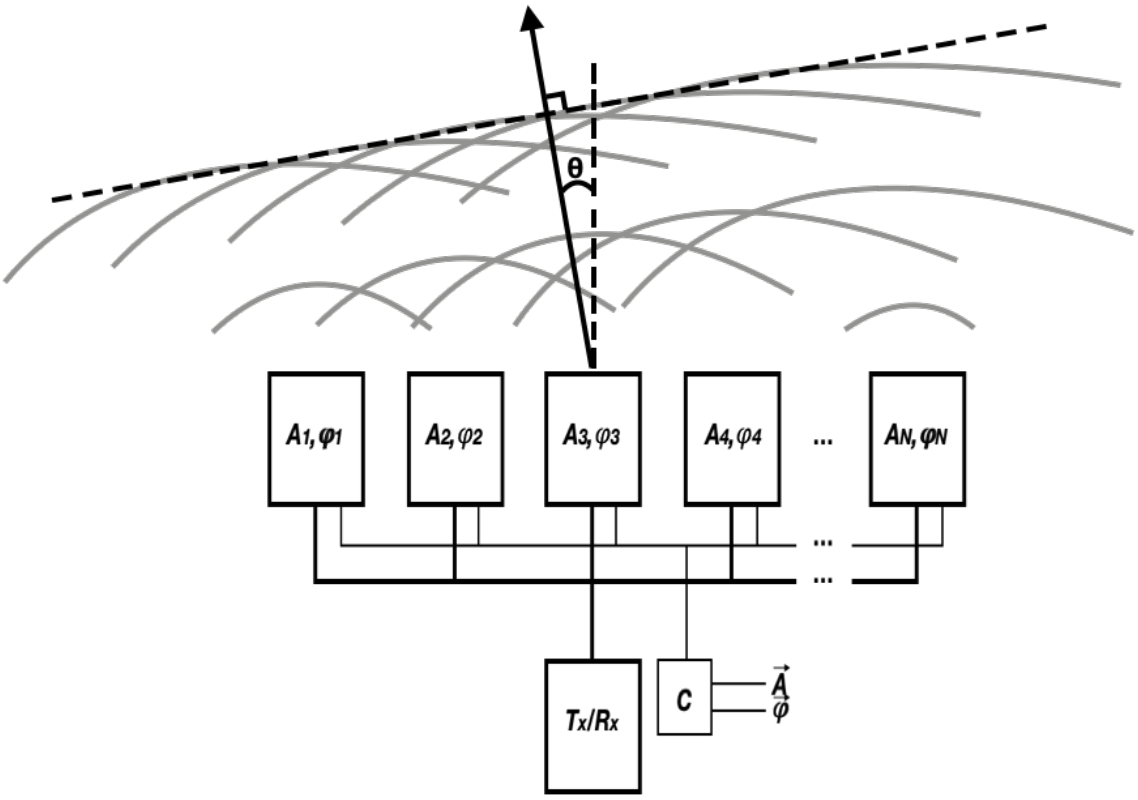

Figure 2.7: Visualization of an array antenna with elements $n = 1, 2, 3, 4, ..., N$ for which each element's amplitude A_n [$W^{1/2}$] and phase φ_n [rad] can be controlled such that the desired steering angle and radiation pattern is obtained.

As visualized by Figure 2.7, the amplitude vector $\vec{A}$ and the phase vector $\vec{\varphi}$ of an $M \times N$ antenna are

$$\vec{A} = [A_1,\ A_2,\ A_3,\ A_4,\ ...,\ A_N]\ [W^{1/2}] \tag{2.5}$$

and

$$\vec{\varphi} = [\varphi_1,\ \varphi_2,\ \varphi_3,\ \varphi_4,\ ...,\ \varphi_N]\ [\text{rad}] \tag{2.6}$$

respectively, for M rows, where P_n and φ_n for elements $n = 1, 2, 3, 4, ..., N$ are the amplitude [$W^{1/2}$] (e.g. the square root of the power [W]) and phase [rad] values for element n, respectively. There are multiple known/popular methods for selecting the antenna amplitude vector $\vec{A}$. For instance, the amplitude vector can be selected as a uniform taper, e.g. with amplitude 1 $W^{1/2}$ for all elements, or it can be designed as a type of Taylor taper [11] allowing the sidelobe levels to be suppressed while keeping a high gain (though, with some loss in the main beam due to the suppression of sidelobe levels). For lobe steering, the phase of each element can be obtained through a linear phase shift across the elements. In order to steer the antenna main beam to the steering angle $\varnothing$ [rad], the required difference in phase $\Delta\varphi$ can be calculated as

$$\Delta\varphi = \frac{2\pi d}{\lambda} \cdot \sin(\varnothing)\ [\text{rad}] \tag{2.7}$$

where d [m] is the element spacing in the array antenna and λ [m] is the wavelength, after which the required phase for element n can be calculated as

$$\varphi_n = \Delta\varphi \cdot (n-1) \tag{2.8}$$

for all N elements. Further, having obtained/selected both the amplitude A_n [W] and phase φ_n [rad] of element n, an initial element value $A_{\text{vec},n}$ of the antenna array vector can be obtained as

$$A_{\text{vec},n} = A_n \cdot \exp\left(j \cdot \varphi_n\right) \tag{2.9}$$

after which the array vector $\vec{A}_{\text{vec}}$ can be obtained after amplitude normalization. The scalar for amplitude scaling can be obtained as

$$A_{\text{scale}} = \left(\sum_{n=1}^{N} |A_n|^2\right)^{-1/2} \tag{2.10}$$

such that the relation

$$\vec{A}_{\text{vec}} = [A_{\text{vec},1},\ A_{\text{vec},2},\ A_{\text{vec},3},\ A_{\text{vec},4},\ ...,\ A_{\text{vec},N}] \odot A_{\text{scale}}\ [\text{W}^{1/2}] \tag{2.11}$$

where '$\odot$' denotes elementwise multiplication can be used to calculate the values of the antenna array vector $\vec{A}_{\text{vec}}$. By using the element amplitude and phase values in the antenna array vector $\vec{A}_{\text{vec}}$ an array antenna's radiation pattern can be controlled in practice. However, it is also possible to apply beamforming in theory on simulated embedded antenna radiation patters (e.g. an array with radiation pattern solutions for each antenna element). For an array with N embedded antenna radiation pattern complex scalar values as

$$\vec{E}_{\text{vec}} = [E_{\text{vec},1},\ E_{\text{vec},2},\ E_{\text{vec},3},\ E_{\text{vec},4},\ ...,\ E_{\text{vec},N}]\ [\text{W}^{1/2}] \tag{2.12}$$

for a certain polarization, azimuth angle θ and elevation angle ϕ, the resulting amplitude and phase values for one θ value and one ϕ value can be calculated by summation of the product of the two arrays in Equations (2.11) and (2.12). For more information on post-processing beamforming, please refer to the explicit beamforming MATLAB code in Appendix A.6.

2.1.5 Realized gain

The directivity D of an antenna defines the concentration of radiated power in a particular direction, whereas the gain of an antenna defines the concentration of input power in a particular direction. In an ideal case, the realizable gain of an antenna would be equal to its directivity (as steering is not applied). This, however, is not possible due to an antenna's gain being a combination of directivity and electrical efficiency (and there will in practice always be some electrical losses). The maximum directivity D_{max} of an antenna can be calculated as

$$D_{max} = \frac{4\pi}{\lambda^2} A \tag{2.13}$$

where λ [m] is the wavelength and A [m^2] is the area of the antenna. By introducing some loss variables, the realized gain of an antenna can be understood as

$$G_{realized} = \epsilon_{rad}\epsilon_{grt}\cos(\varnothing)\epsilon_{pol}\epsilon_{ill}D_{max} \tag{2.14}$$

where the maximum directivity D_{max} is multiplied with the radiation efficiency ϵ_{rad}, the grating lobe efficiency ϵ_{grt}, the cosine scalar of the steering angle $\varnothing$, the polarization efficiency ϵ_{pol} and the illumination efficiency ϵ_{ill} [12]. For instance, if the efficiencies in Equation (2.14) together make up a scalar of 0.5 in natural values, it would cause a $10\log_{10}(0.5) = 3.0$ dB decrease in gain from the maximum directivity to the antenna realized gain.

2.1.6 Typical antenna designs

Typical antenna designs that are used in array antennas are wire antennas, slot antennas, waveguide antennas, microstrip/patch antennas, horn antennas and reflector antennas [13]. Relevant theory regarding waveguide antennas is described in Section 2.1.6.1 as this antenna type was utilized in the project.

2.1.6.1 Open-ended waveguide antenna

A rectangular open-ended waveguide has a shell made of metal of width a and height b, which can be filled with a material with any permittivity $\epsilon = \epsilon_r \cdot \epsilon_0$. However, the metallic shell is often assumed to be a perfect electric conductor (PEC) as for the ideal case, e.g. to reduce simulation time in many software environments, and it is often filled simply with air or vacuum. Further, the operating frequencies of a waveguide can be adjusted by changing the value of the width a, but also through utilizing various methods of altering the shapes and sizes of the walls. In waveguides either transverse electric (TE) or transverse magnetic (TM) modes can be created. The first mode that propagates in a rectangular waveguide is TE_{10} which has the lowest cut-off frequency $f_{c_{mn}}$ (e.g. the fundamental mode is the one with the lowest cut-off frequency). More generally, the cut-off frequency $f_{c_{mn}}$ of a rectangular open-ended waveguide with width a and height b can be calculated as

$$f_{c_{mn}} = \frac{c}{2\pi\sqrt{\epsilon_r}}\sqrt{\left(\frac{m\cdot\pi}{a}\right)^2 + \left(\frac{n\cdot\pi}{b}\right)^2} \tag{2.15}$$

where c is the speed of light in vacuum, ϵ_r is the relative permittivity, and m and n specify the waveguide mode. From Equation (2.15) it can be seen that the width a controls the dominant mode and that the height b only starts to matter at the higher modes TE_{01}, TE_{11} and TM_{11} [14]. A method used to tune the input impedance and power throughput is placing ridges in the waveguide [14]. By placing two ridges of an arbitrary size in the waveguide, the cut-off frequency of the waveguide can be lowered such that the electromagnetic waves start to propagate earlier. Further, this enables the impedance to be better matched and to be made more constant over a wider bandwidth, and makes it possible to obtain a higher power throughput at the operating frequency f_c. The added ridges to the waveguide, however, do reduce the total amount of power that the waveguide can operate with. Figure 2.8 shows

a rectangular waveguide with width a, height b, permittivity ϵ and permeability μ. Additionally, the added ridges in dashed lines in Figure 2.8 visualize how the inside of a waveguide can be modified in order to lower the cut-off frequency and obtain better matching, bandwidth and power throughput.

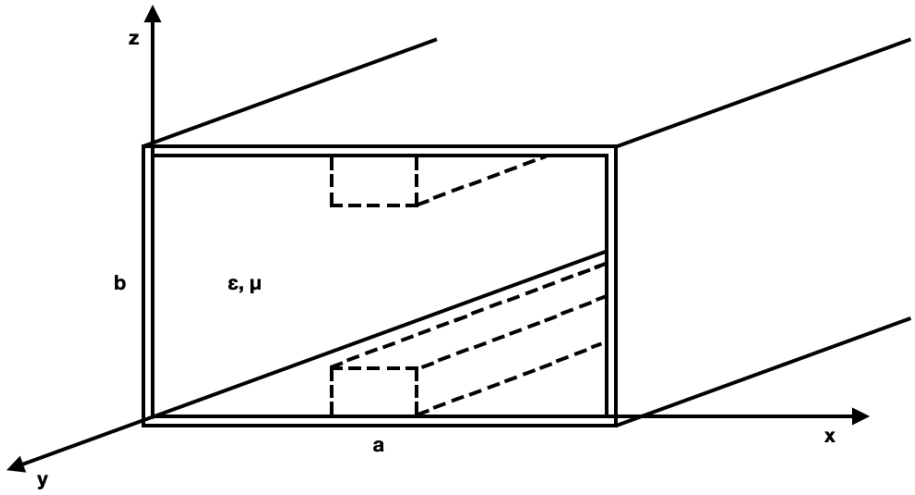

Figure 2.8: Visualization of an open-ended waveguide antenna, and (in dashed lines) added ridges to it.

2.2 Radiation obstruction cloaking and anti-scattering techniques

In this section, the relevant theory for the implemented radiation absorbent cloaking and anti-scattering techniques is explained, including the basics about refraction, reflection and diffraction of electromagnetic waves in Section 2.2.1, the general theory regarding the conventional narrowband and wideband absorbents in Section 2.2.2 as well as examples of both types that were implemented in the project, and lastly the mathematical requirements for coordinate transformation using meta-materials for bending electromagnetic waves around cylindrical obstructions in Section 2.2.3.

2.2.1 Refraction, reflection and diffraction

Refraction is when electromagnetic waves are bent as they travel at an angle from one medium into another with a different refractive index, and it is what makes for instance lenses, glasses, prisms and rainbows possible. The change of refractive index causes the light to change speed and, thus, also change the angle/direction. Figure 2.9 shows how light is refracted as it travels with the velocity v_1 and the incidence angle θ_1 ($<\theta_c$) from a medium with the refractive index n_1 into a substrate with refractive index n_2. As can be seen in Figure 2.9, the change of medium and refractive index causes the light ray to change velocity to v_2 and to bend to the refraction angle θ_2 from the normal plane perpendicular to the medium interference plane [15].

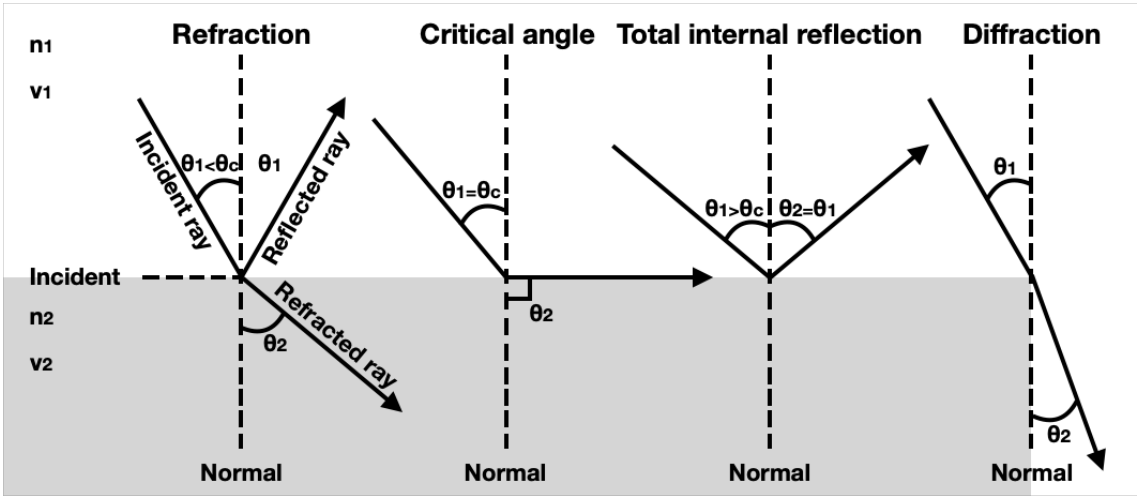

Figure 2.9: Visualization of refraction and reflection of a light ray moving from one medium into another, or diffraction/bending of the light ray as it hits the edge of the different medium object.

The refraction angle of a light ray as it travels from one medium to another can be calculated with Snell's law

$$\frac{\sin(\theta_1)}{\sin(\theta_2)} = \frac{n_2}{n_1} = \frac{v_1}{v_2} \tag{2.16}$$

where θ_1 is the incident angle of the light ray (from the normal, as defined in Figure 2.9), θ_2 is the reflection angle (again, defined from the normal), n_1 and n_2 are the refractive indices of the two mediums, respectively, and v_1 and v_2 are the light ray's velocities in the two different materials. As shown in Figure 2.9, refraction and reflection occurs when the incident angle θ_1 is smaller than the critical angle θ_c ($\theta_1 < \theta_c$). The critical angle depends on the two mediums. For air and water as the two mediums, for instance, the critical angle is θ_c =48.6°. At the critical angle, the refracted wave lies in the incident plane, or equivalently is perpendicular to the normal plane with the refraction angle of $\theta_2 = 90°$, and after the critical angle there will be total internal reflection, i.e. no light rays will refract into the second medium as everything is reflected back in the first one. Further, as visualized by the rightmost case in Figure 2.9, as a light ray hits the edge of a medium of different refractive index, diffraction/bending around it will occur.

2.2.2 Conventional radar absorbent materials

A radar absorbent material (RAM) is a material specifically designed to absorb electromagnetic radiation. Electromagnetic absorbents are application oriented and work for a specific bandwidth and, generally, the two different types are resonant or narrowband absorbents and broadband absorbents. The conventional radar absorbent materials are either based on the Salisbury screen absorbent or the Dallenbach layer absorbent, both operating by absorbing incident electromagnetic energy and converting it to heat, or on their multi-layer counterparts [16][17]. Both the

Salisbury screen absorbent and the Dallenbach layer absorbent are resonant absorbents that are simple in their structure, low-cost and highly efficient, but they yield relatively narrow working bandwidths because of the frequency-dependency as a specific wavelength is required for the desired resonance in the layered material. However, more broad frequency ranges can be employed as the absorbents are designed with multiple layers. Instead, broadband absorbents are more or less frequency-independent (e.g. they often have a lower limit set by their thickness, after which they are somewhat frequency independent) and effective over a broad range of frequencies, however they are relatively less efficient than the narrowband absorbents over a shorter range and, especially, they are much thicker than the equivalent resonant absorbents. In this section, the concepts of narrowband and wideband radiation absorbents are explained, and examples of both types of absorbents that were implemented in this project are given.

2.2.2.1 Narrowband radiation absorbents

In this section, the two conventional types of electromagnetic resonant narrowband absorbents are described more in detail, and an example is given of a narrowband absorbent made out of ferrites (later used in this project). Synoptically, the difference between the Salisbury screen and the Dallenbach layer is that the Dallenbach absorbent employs a lossy homogeneous layer on the metal to be cloaked while the Salisbury absorbent employs an inhomogeneous screen with a low loss/lossless dielectric in between.

2.2.2.1.1 Salisbury screen and Dallenbach layer absorbents

A Salisbury absorbent is an inhomogeneous structure that consists of a resistive screen placed in front of a dielectric spacer (ideally) without losses over a metallic surface to be cloaked [17]. It was one of the early electromagnetic absorbents for radar applications and is a resonant absorbent that converts electromagnetic radiation in a narrow band of frequencies into heat through destructive interference of the incident wave and the reflected radiation from the metal surface, phase shifted by 180° because of the quarter wavelength space between the screen and the metal. Figure 2.10 visualizes the Salisbury absorbent with the Salisbury resistive screen placed a quarter wavelength from the metallic surface with a low loss/lossless spacer in between such that the waves reflected from the metal in total travel half a wavelength from and back to the Salisbury screen. The resistive screen is typically much thinner than the wavelength of the desired incident waves to absorb, and the spacer between the first and second incident plane can be air or another dielectric with a low dielectric constant and a low relative admittance [18].

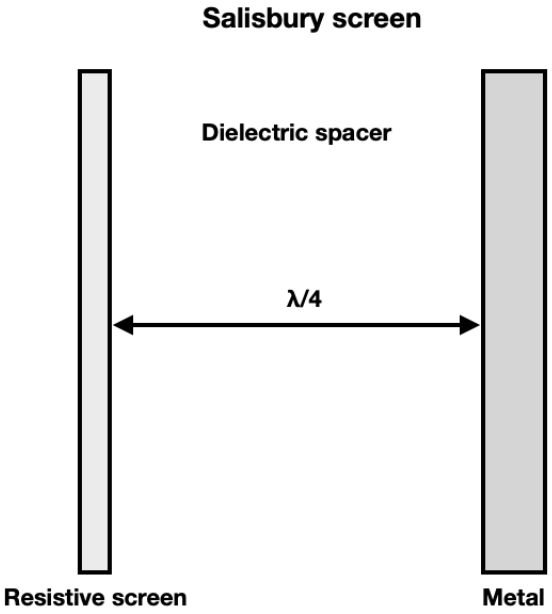

Figure 2.10: Visualization of the Salisbury screen absorbent.

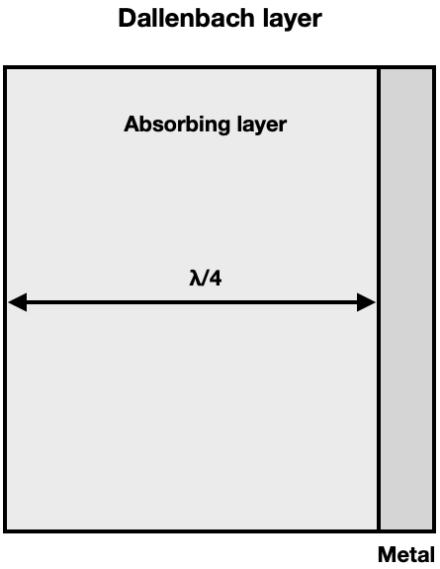

Figure 2.11: Visualization of the Dallenbach layer absorbent.

A Dallenbach absorbent is a homogeneous absorbing layer placed on the metallic surface to be cloaked such that electromagnetic radiation in the desired frequency range is converted to heat through destructive interference. Its absorption performance directly depends on the electromagnetic properties and thickness of the lossy layer [17]. Figure 2.11 visualizes the Dallenbach absorbent with the Dallenbach layer with a thickness of a quarter wavelength placed on the metal such that the waves in total travel a half wavelength before being cancelled through destructive interference. That is, as the electromagnetic waves hit the Dallenbach layer, some is reflected and some is transmitted through the incident plane and reflected on the metal. Further, as the Dallenbach layer is designed to be a quarter wavelength in thickness the waves reflected back from the metal surface to the incident plane of the Dallenbach layer are phase shifted with 180° such that destructive interference occurs and the electromagnetic radiation (that is not reflected at the first incident plane) is cancelled out [19]. Generally, for a single layer material the electric wavelength λ_r inside it can be calculated as

$$\lambda_r = \frac{c}{f_c\sqrt{\epsilon_r}} \tag{2.17}$$

where c is the speed of light in vacuum, ϵ_r is the relative permittivity of the material and f_c is the center frequency. Hence, it can be understood that the Salisbury screen absorbent and the Dallenbach layer absorbent can employ a dielectric spacer and an absorbing layer, respectively, of thicknesses smaller than a quarter wavelength of the signal to be absorbed.

2.2.2.1.2 Ferrite material absorbents

An example of a Dallenbach layer is a ferrite electromagnetic wave absorbent, where a quarter wavelength thick single layer of ferrite with magnetic loss properties is applied to the surface to be cloaked. Ferrite absorbents can for example be made out of sintered ferrite, rubber ferrite, resin ferrite, or a mix of ferrite and dielectrics (e.g. for higher frequency applications). The term ferrite comes from the Latin word for iron "Ferrum" as they are known as magnetic materials [20]. Further, ferrites are usually manufactured by using ceramic processing techniques and as they are easily molded and shaped they are very flexible in their application areas [21]. An example of a ferrite absorbent material is FGM-125 [22] manufactured by Eccosorb, which is evaluated in Section 3.3.1.

2.2.2.2 Wideband radiation absorbents

With the use of multi-layer electromagnetic wave absorbents, e.g. absorbents with two or more layers where each layer has its own material constants and thickness, multiple types of wideband radiation absorbents can be realized [23]. An example of a two layer wideband absorbent is an absorbent constructed of an outer layer of ferrite and an inner layer (e.g. the layer closest to the surface to be cloaked) of dielectric material. Such an absorbent can yield a wideband solution of large magnetic and dielectric losses compared to an absorbent consisting of just a quarter wavelength layer of ferrite, as described in Section 2.2.2.1.2. Another method of creating a wideband absorbent is constructing a multi-layer absorbent with increasing conductivity throughout the absorbent, the theory for which is explained in Section 2.2.2.2.1.

2.2.2.2.1 Absorbent with increasing conductivity

An example of a wideband radiation absorbent is a multi-layered absorbent with increasing conductivity going into the absorbent. Such an absorbent was implemented in this project through layering sheets with different conductivity, which layers are visualized in Figure 3.17 in Section 3.3.3. The resulting layered material acts as an absorbent as the field attenuation increases into the material along with the conductivity. Attenuation is a function of the permittivity ϵ, the conductivity σ and the frequency f_c. According to the wave propagation theory and Maxwell's equations, the attenuation constant α for an electromagnetic plane wave can be calculated as

$$\alpha = 2\pi f_c \left(\frac{\mu\epsilon}{2} \left(\sqrt{1 + \left(\frac{\sigma}{2\pi f_c \epsilon} \right)^2} - 1 \right) \right)^{1/2} \text{ [Np/m]} \tag{2.18}$$

where f_c is the frequency of the wave, $\epsilon = \epsilon_r \cdot \epsilon_0$ and $\mu = \mu_r \cdot \mu_0$ are the permittivity and permeability of the medium, respectively, and σ is the electrical conductivity. Hence, as the attenuation factor α in Equation (2.18) will become large rapidly as the conductivity σ increases but the values of the frequency f_c, permittivity ϵ and permeability μ stay constant, it can be understood that the attenuation factor α can be controlled by modifying the conductivity σ as desired (e.g. increasing σ throughout a medium will yield an increasingly lossy material).

2.2.3 Meta-material radiation cloaking

The Virtual Institute for Artificial Electromagnetic Materials and Metamaterials (the METAMORPHOSE VI AISBL, in short) defines meta-materials as "an arrangement of artificial structural elements, designed to achieve advantageous and unusual electromagnetic properties" [24]. Simply put, meta-materials are artificially made out of usual materials that can be found in nature such that they obtain unusual but advantageous properties. Through changing sub-wavelength details of electromagnetic materials, as supposed to their chemical composition, meta-materials with properties that are difficult or impossible to find in nature can be created [25]. Meta-materials that have not yet been found in nature are materials with relative permittivity $\epsilon_r < 1$ and/or relative permeability $\mu_r < 1$, which in theory can yield a variation of useful properties. For instance, if the relative permittivity ϵ_r and the relative permeability μ_r are simultaneously negative (e.g. $\epsilon_r < 0$ and $\mu_r < 0$), the result will be a left-handed orthogonal material (as opposed to the regular right-handed one) with negative refractive index n bending waves as shown in Figure 2.12. Instead, if they are non-simultaneous the result will be evanescent waves with an exponential decay of the wave vector due to the wave number k becoming complex. Further, a meta-material with the properties $0 < \epsilon_r < 1$ and $0 < \mu_r < 1$ will yield a right-handed orthogonal system (as regular), however with an increased phase velocity v_p. This can be seen through studying the relations

$$v_p = \frac{2\pi f_c}{k} = \frac{c}{n} \tag{2.19}$$

and

$$k = \begin{cases} -\frac{2\pi f_c}{c}\sqrt{\epsilon_r \mu_r} & \text{if } \epsilon_r < 0 \text{ and } \mu_r < 0 \\ +\frac{2\pi f_c}{c}\sqrt{\epsilon_r \mu_r} & \text{otherwise} \end{cases} \tag{2.20}$$

where v_p is the phase velocity, f_c is the frequency of the wave, k is the wave number, c is the speed of light in vacuum, n is the refractive index, ϵ_r is the relative permittivity and μ_r is the relative permeability. With the use of different kinds of meta-materials, different types of electromagnetic cloaks with exotic properties can be constructed. For instance, electromagnetic cloaks using meta-materials can be achieved through coordinate transformation, visualized in Figure 2.13, which is described more in detail in Section 2.2.3.1.

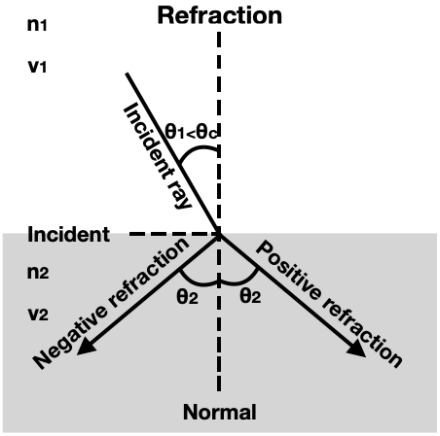

Figure 2.12: Visualization of negative refraction of a left-handed material, which can occur if the relative permittivity ϵ_r and the relative permeability μ_r of the material hit by the incident ray simultaneously are negative over a range of frequencies.

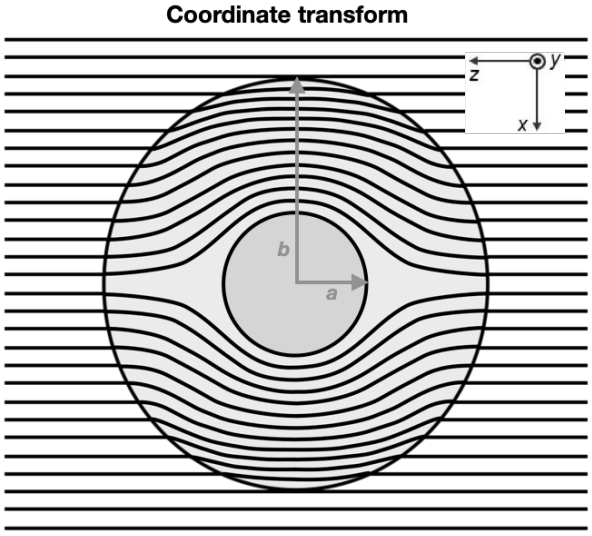

Figure 2.13: Top view visualization of coordinate transformation, where the incident rays (shown as in far field, as a plane wave front) are bent around a cylinder obstruction of radius a because of a controlled refractive index n in the meta-material of thickness $(b - a)$ around it. The lines show the direction of power flow, i.e. the Poynting vector, and the coordinate system specification refers the illustration to the rotation used in this project.

2.2.3.1 Coordinate transformation/ray bending

The coordinate transformation technique means to guide electromagnetic waves around the obstructing object, e.g. a cylindrical or spherical volume, through the use of the controlled ray bending properties of meta-materials. This technique is beneficial as it, if successful, makes the cloaked object entirely invisible in the electromagnetic spectrum [26]. Hence, even though it is difficult to obtain the required material properties in practice, previous works suggest that it is possible to obtain coordinate transformation cloaks for cylindrical obstructions both for vertically and horizontally polarized electromagnetic waves at radar frequencies [25][27].

In order to steer electromagnetic waves around a cylindrical obstruction of radius a within a cloaking shell of radius b (defined from the centre of the cylindrical obstruction such that the cloak thickness is $b - a$) as defined in Figure 2.13 using coordinate transformation, all the electromagnetic fields in the region $r < b$ have to be compressed into the cloak region $a < r < b$. Please note that the cylinder obstruction is defined to be extended along the z-axis throughout this section, while Figure 2.13 specifies the implemented rotation for the setup in this project. In theory, this transformation results in the anisotropic permittivity and permeability requirements

$$\epsilon_r = \mu_r = \frac{r-a}{r} \ , \ \epsilon_\theta = \mu_\theta = \frac{r}{r-a} \ , \ \epsilon_z = \mu_z = \Big(\frac{b}{b-a}\Big)^2 \cdot \frac{r-a}{a} \tag{2.21}$$

within the region $a < r < b$ of the cloaking shell, where the subscripts r, θ and z denote the radial, azimuth and z-axis alignments, respectively [27]. For TE illumination where the incident electric field is polarized along the z-axis (e.g. vertical polarization, following the notation in this report), the only remaining requirements from Maxwell's equations are

$$\mu_r = \frac{r-a}{r} \ , \ \mu_\theta = \frac{r}{r-a} \ , \ \epsilon_z = \Big(\frac{b}{b-a}\Big)^2 \cdot \frac{r-a}{a} \tag{2.22}$$

which have been reported to have been achieved in practice by varying the dimensions of split-ring resonators (SRRs) placed in series in rings around cylindrical obstructions [1]. As can be seen in Equation (2.22), a cloak for vertically (TE) polarized electromagnetic waves can be achieved through designing a material with radially changing values of the permittivity in the z-axis and constant permeability values in the radial and azimuth alignments. Instead, for TM illumination where the incident magnetic field is polarized along the z-axis (e.g. horizontal polarization, following the notation in this report), only the requirements

$$\epsilon_r = \frac{r-a}{r} \ , \ \epsilon_\theta = \frac{r}{r-a} \ , \ \mu_z = \Big(\frac{b}{b-a}\Big)^2 \cdot \frac{r-a}{a} \tag{2.23}$$

have to be satisfied.

2.3 Simulation software

For this report, the programming language and numeric computing environment MATLAB was implemented for post-processing of results obtained using Ansys High Frequency Simulation Software (Ansys HFSS). In this section, a short introduction is given of the used simulation software Ansys HFSS which is a 3D electromagnetic simulation software which makes it possible to design and simulate high-frequency electronic products such as antenna elements, array antennas and RF or microwave components [28]. Given that the user has defined a geometry with some material properties over a specified range of frequencies, and correctly prepared a suitable solver method, Ansys HFSS's various finite element method solvers automatically handle the simulations yielding results that, depending on the implemented method, can be expected in practice. The software is used worldwide to design for instance communication systems, satellites and internet-of-things (IoT) products [29]. In this project, Ansys HFSS's 'Lattice Pair' boundary, 'PML' (perfectly matched layer) boundary and 'FE-BI' (finite element boundary integral) boundary functions as well as its 'IE' (integral equation) region function were used for simulations. The different region and boundary implementations each have strengths and weaknesses and they are thus suitable for different cases. More information about the different Ansys HFSS implementations can be found in Section 3.2 which describes the methods' strengths (and weaknesses) and how they can be implemented, and in Appendix B which details how to employ the different techniques in Ansys HFSS.

3
Methods

In this chapter, the methodologies of the different stages of the project are described. The design of an array antenna intended to work with vertical polarization for scanning in the H-plane/azimuth plane at 9.5 GHz (X-band) is described in Section 3.1. Further, Section 3.2 details the antenna and obstruction simulation in Ansys HFSS implemented for later evaluation of the realized gain and average sidelobe level for the antenna for a range of steering angles in the H-plane without and with an obstruction in front of it. For analysis of different electromagnetic cloaking and anti-scattering techniques, the designed shells detailed in Section 3.3 were examined. Lastly, Section 3.4 describes the post-processing of the simulated array antenna radiation patterns in MATLAB performed in order to evaluate the different obstruction cloaking solutions.

3.1 Design of an X-band array antenna in HFSS

For later configuration of a 1×21 element antenna, a single open-ended ridge waveguide element was designed and simulated in Ansys HFSS. Section 3.1.1 describes the design and performance of the constructed ridge waveguide element, and Section 3.1.2 shows the obtained realized gain radiation pattern for the designed 1×21 element array antenna with uniform taper and with Taylor taper. When designing the element in Ansys HFSS and metal was required, the material was in most cases set to be a perfect electrical conductor (PEC) such that the simulations in Ansys HFSS would be faster (e.g. it is possible to select another material but the large increase in simulation time is often not worth the small gain in accuracy, and it was decided that it was not in this case). The antenna element was designed to work at and around 9.5 GHz (e.g. to be realistic), even though simulation results would only be gathered for the single centre frequency $f_c = 9.5$ GHz. More specifically, the antenna element was designed for a low insertion loss IL (within $0.5 - 1$ dB of the minimum insertion loss) and for a high return loss RL (more than 10 dB return loss for the working bandwidth of the element), which was achieved through studying the active S-parameters obtained from the Ansys HFSS simulations of the element. Further, as the antenna element was designed with TE polarization, with its incident electric field polarized along the z-axis, the array antenna was extended in the x-dimension such that the highest gain and otherwise best performance would be achieved as the beam was steered in the H-plane/azimuth plane. This intended working rotation of the designed waveguide element is specified by Figure 3.1 in Section 3.1.1. Further, as described above, Section 3.1.2 shows the rotation and size

of the antenna (designed and selected such that the best realized gain was obtained for $\phi = 0°$) as it visualizes the obtained realized gain as a polar 3D plot over the 1×21 element antenna for the two different tapers.

3.1.1 Waveguide antenna element

In order to design an array antenna out of waveguide elements about the centre frequency 9.5 GHz, the single open-ended ridge waveguide element in Figure 3.1 was designed in Ansys HFSS. The waveguide element was designed to operate with the TE_{10} mode and the procedure for producing the waveguide element followed the theory in Section 2.1.6.1. That is, the dimensions for the waveguide element were chosen using Equation (2.15), after which ridges [14] were added and their dimensions tuned (simply by trial and error) in order to obtain the desired functionality about the frequency 9.5 GHz. In Ansys HFSS, the element was set to be fed from a waveport at the bottom of the open-ended waveguide. Further, PEC boxes were added to the sides of the waveguide element (e.g. the black boxes that can be seen in Figure 3.1) such that the elements would be spaced by half a wavelength ($\lambda/2$) in all directions if the design was extended into a matrix (e.g. later array antenna designs were simplified at this early stage). To specify, an element spacing of $\lambda/2$ was desired as it does not introduce periodically repeating peaks/copies of the main lobe of the antenna excitation, i.e. grating lobes, as described in Section 2.1.2. Further, the actual waveguide was set to be a PEC, as well as the ridges added inside in order to move the working frequency of the element, as described in Section 2.1.6.1. Other than this, the inside of the waveguide was set to consist of vacuum.

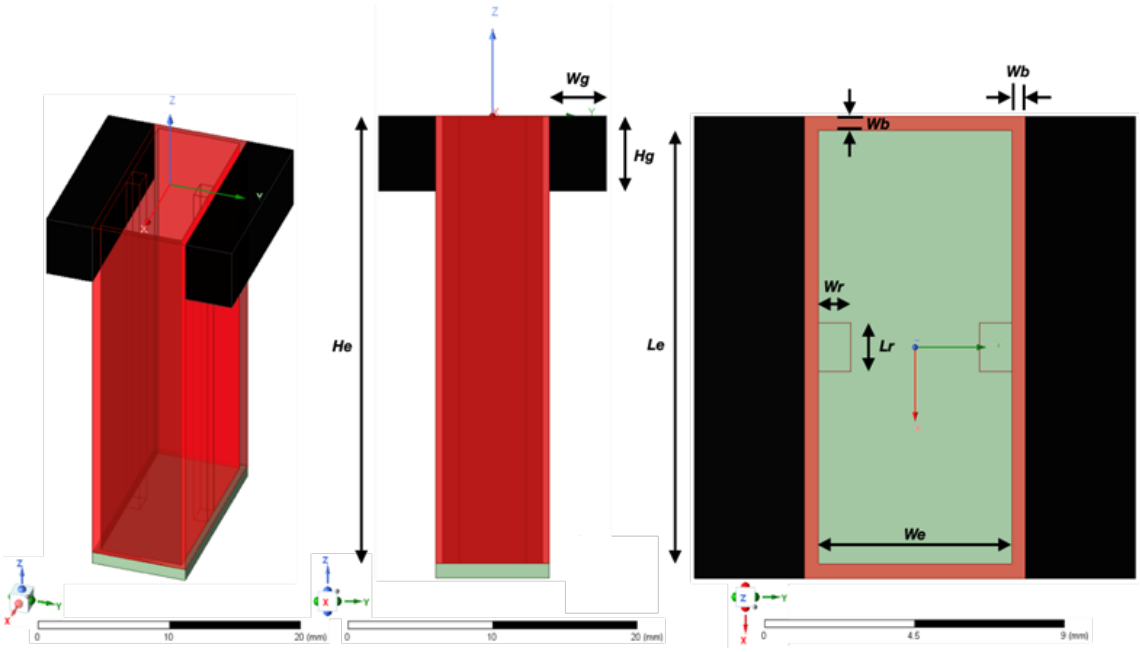

Figure 3.1: Definition of the designed ridge waveguide antenna element's dimensions, further specified in Table 3.1.

The defined dimensions in Figure 3.1 are specified in Table 3.1, where the subscript 'e' refers to the inside dimension of the waveguide, 'r' refers to a ridge dimension and 'g' refers to the PEC boxes added to properly space the elements in an array.

Table 3.1: Specification of the designed ridge waveguide antenna element's dimensions.

Variable	L_e	L_r	W_e	W_g	W_r	W_b	H_e	H_g
Value [mm]	15.0	1.67	7.00	8.00	1.17	0.50	30.0	5.00

Figure 3.2a shows the relative S-parameters for the designed open-ended ridge waveguide antenna element for different steering angles $\varnothing = \theta$ in the H-plane/azimuth plane, obtained through simulating the element as an infinite array in Ansys HFSS using Lattice Pairs and a Flouqet port such that the results would be comparable with a larger array antenna (e.g. an antenna with multiple elements such as the designed waveguide). As can be seen by the lower curves in Figure 3.2a, the waveguide element yielded a rather high return loss RL=$|S_{11}$ [dB]| of more than 10 dB within the frequency range 9.15–9.95 GHz (e.g. there were low reflections at the antenna's in-port), while still offering approximately the minimum insertion loss IL=$|S_{21}$ [dB]| (e.g. the relative output effect of the element was high), as can be seen by the top curves of S_{21}. The designed waveguide element was not evaluated for more steering angles than $\varnothing = \theta = 30°$ at this stage because it was decided that this steering range was sufficient for a realistic antenna design. Additionally, only positive steering angles were evaluated at this stage due to the antenna element's symmetric design, e.g. the corresponding negative steering angles would yield approximately the same result.

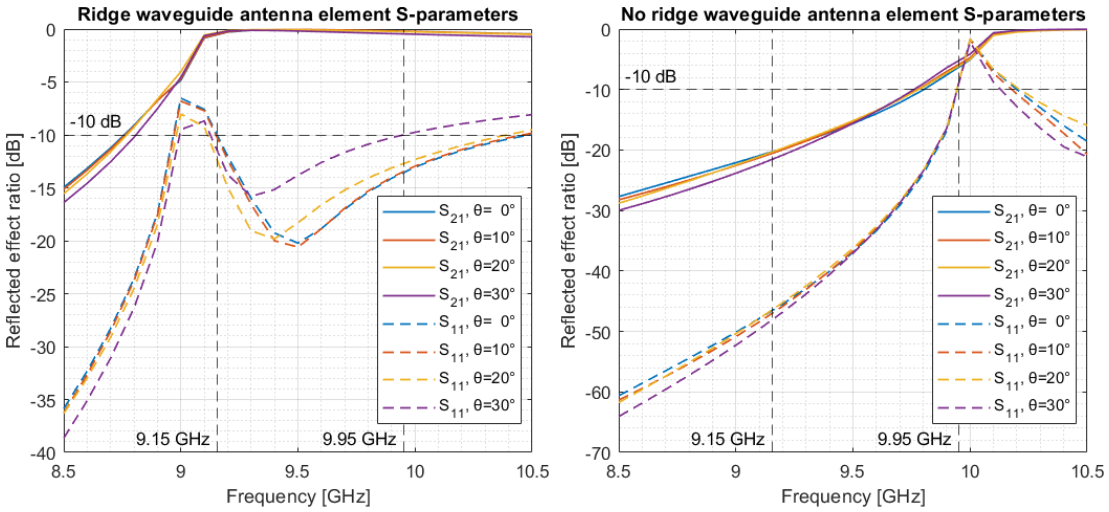

a) With ridges. b) Without ridges.

Figure 3.2: Reflected effect ratio [dB] showing the insertion loss IL=$|S_{21}$ [dB]| and return loss RL=$|S_{11}$ [dB]| of the designed waveguide antenna element, with and without ridges, obtained through infinite array antenna simulations in HFSS. To specify, for an effective antenna element it is desired that S_{21} and S_{11}, respectively, are large and small (e.g. for a low insertion loss and high return loss, respectively).

In order to visualize the effect of the added ridges inside the open-ended waveguide, Figure 3.2b shows the relative S-parameters for the element *without* ridges. As can be seen by the lower S_{11} curves, the return loss at the in-port was sufficiently high without the ridges, however the top curves of S_{21} suggested that the insertion loss was quite high as well and, hence, that the relative output effect of the designed element would be very low in the desired frequency range.

3.1.2 Designed array antenna - performance and coordinate system specification

By extending the designed open-ended ridge waveguide described in Section 3.1.1 the 1×21 element array shown in Figure 3.3 was created. It was decided to design the array antenna with 21 elements such that the resulting main beam was thin enough in relation to the thickness of the pole obstructions (e.g. to ensure that easily comparable results would be obtained), however such that the resulting antenna was small/short enough such that it was possible to simulate in the antenna and obstruction simulation described in Section 3.2 with regards to simulation time and required computer power (e.g. required RAM). Figure 3.3 visualizes the realized gain of the antenna for different tapers both in 3D for the slice $\phi = 0°$ which was exclusively investigated in this project due to the set limitations and (as an overlay, in order to see the general performances of the antenna) for all ϕ. The TE_{10} mode waveguide elements were rotated in the array such that the highest gain was achieved, which was for the ϕ-polarization. Hence, with the antenna elements placed along the x-axis and the direction of the electric fields inside the elements along the y-axis, the antenna was designed to operate with vertical polarization (here equivalent to ϕ-polarization) for scanning in the H-plane, e.g. for steering angles $\varnothing = \theta$ in the azimuth plane. That is, the excitations in the slice $\phi = 0°$ shown in Figure 3.3 will be steered in the xz-plane as the antenna is steered in the H-plane/azimuth plane. Hence, for a worst case scenario of a pole obstruction in front of the antenna, a metallic pole should be (and was) placed aligned with the y-axis at a positive z-coordinate such that the pole lies at steering angle $\varnothing = 0°$ in the H-plane/azimuth plane in front of the antenna yielding short circuits along the pole and the largest amount of scattering. Distinct from this, having a horizontally polarized antenna with the same setup of the pole would yield much less scattering as the horizontally polarized waves would go around the pole somewhat with ease, relatively.

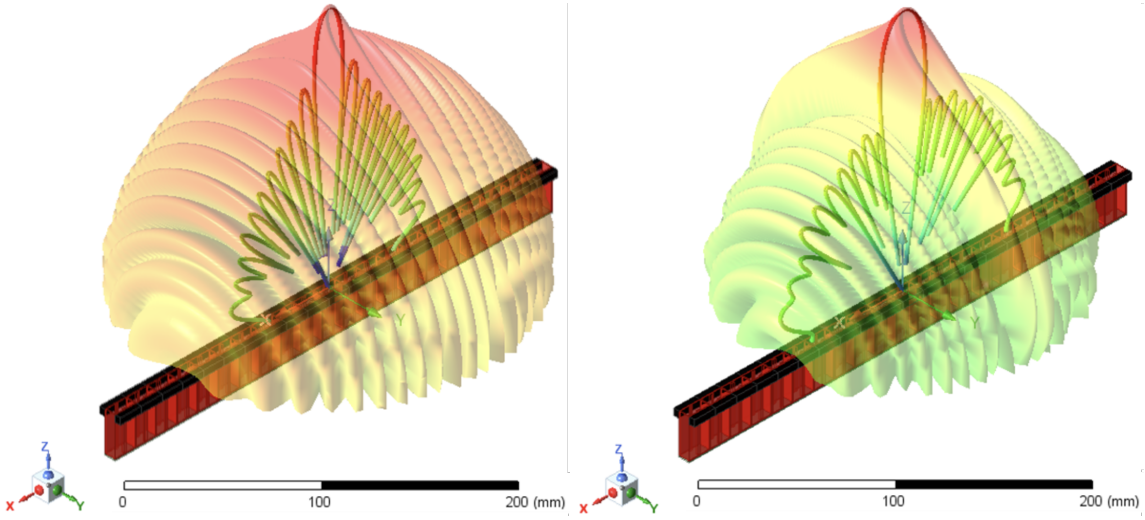

a) Uniform taper excitation. b) Taylor taper excitation.

Figure 3.3: Realized gain of the designed 1x21 element waveguide antenna, shown as a 3D polar plot in the Modeler Window in Ansys HFSS for the elevation angle slice $\phi = 0°$ and (as an overlay) for all ϕ, as a uniform taper and a Taylor taper is applied, respectively. For the uniform taper and Taylor taper excitations, the realized gain in the main beam were 18.29 dB and 17.54 dB in the slice $\phi = 0°$, respectively, as shown in figure 3.4.

By the specified waveguide dimensions in Figure 3.1 and Table 3.1 in Section 3.1.1 the largest antenna length L_{ant} and the antenna area A_{ant} can be calculated as

$$\begin{aligned} L_{ant} &= 21 \cdot (L_e + 2W_b) \ \ [\text{m}] \\ A_{ant} &= L_{ant} \cdot (W_e + 2W_b) \ \ [\text{m}^2] \end{aligned} \tag{3.1}$$

to $L_{ant} = 33.6$ cm and $A_{ant} = 26.9$ cm^2. Further, using Equation (2.4) and the antenna length L_{ant}, the array antenna's far field can be calculated to begin at approximately a distance of 7 m from the antenna. As can be seen in Figure 3.4, the designed antenna had a realized gain in the main beam of 18.3 dBi and 17.5 dBi with uniform and Taylor taper, respectively, as steering was not applied (e.g. in $\phi = 0°$ and $\theta = 0°$). Additionally, by studying Figure 3.4 it can be seen that the Taylor taper excitation yielded a slightly wider beam compared to the uniform taper as the price for the reduced sidelobe level in the forward direction's azimuth angle range.

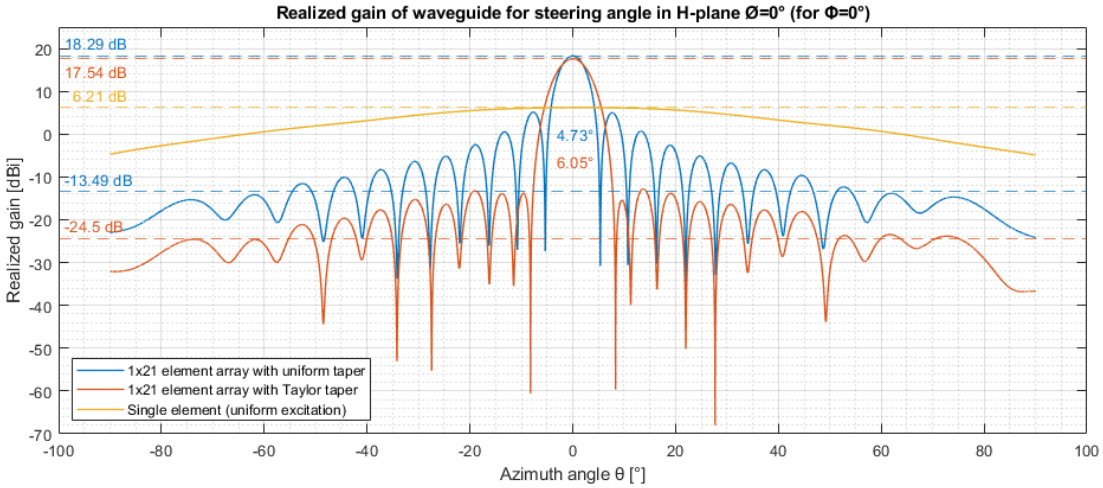

Figure 3.4: Realized gain of the 1×21 element waveguide antenna with a uniform taper and a Taylor taper as steering was not applied (e.g. for $\phi = 0°$ and $\varnothing = 0°$), constructed of the designed element in Section 3.1.1, and the realized gain of the single element. The figure also specifies the tapers' respective highest realized gain, ASLL and 3 dB beamwidth.

3.2 Antenna and obstruction simulation in Ansys HFSS

In this section, the general setup of the array antenna and pole obstruction simulation in Ansys HFSS is described, as well as the investigated scenarios (e.g. the investigated pole diameters and distances). As detailed in Section 3.1.2, the antenna was designed for scanning in the H-plane/azimuth plane/xz-plane with vertical polarization. Hence, with TE illumination where the incident electric field is polarized along the y-axis, for investigation of a worst case obstruction scenario in terms of scattering the pole should be (and was) extended along the y-axis as well and placed in front of the array antenna at a positive value of z. Hence, the array antenna and the pole obstruction were arranged in Ansys HFSS as described in Figure 3.5. As specified in Figure 3.5, the pole obstructions were placed only at $x = 0$, i.e. directly in front of the array antenna at the azimuth angle $\theta = 0°$, which was due to the set limitations of the project described in Section 1.4. Using this Ansys HFSS environment, simulations were run with all variations of the pole diameters 5 cm and 10 cm and pole distances 1 m, 2 m, 3 m, 4 m, 5 m, 10 m, 20 m and 30 m from the array antenna. As further described in Section 1.4, for all simulations the realized gain far field data was exported for the azimuth angles $-90° \leq \theta \leq 90°$ and, hence, the desired results of the average sidelobe level for different steering angles were calculated for the forward direction. Thus, unless otherwise stated, the calculated average sidelobe levels throughout the project refer to the results in front of the antenna. For all simulations, the pole was 5 m in length due to this being long enough such that the pole would have a large enough negative impact on the antenna, but short enough such that the simulations would not take an unreasonable amount of time to run or require too much computation power (e.g. computer or server RAM).

Further, the different designed cloaking "shells" described in Section 3.3 were placed around the pole obstruction in the same Ansys HFSS environment, for which all the same simulation variations were performed.

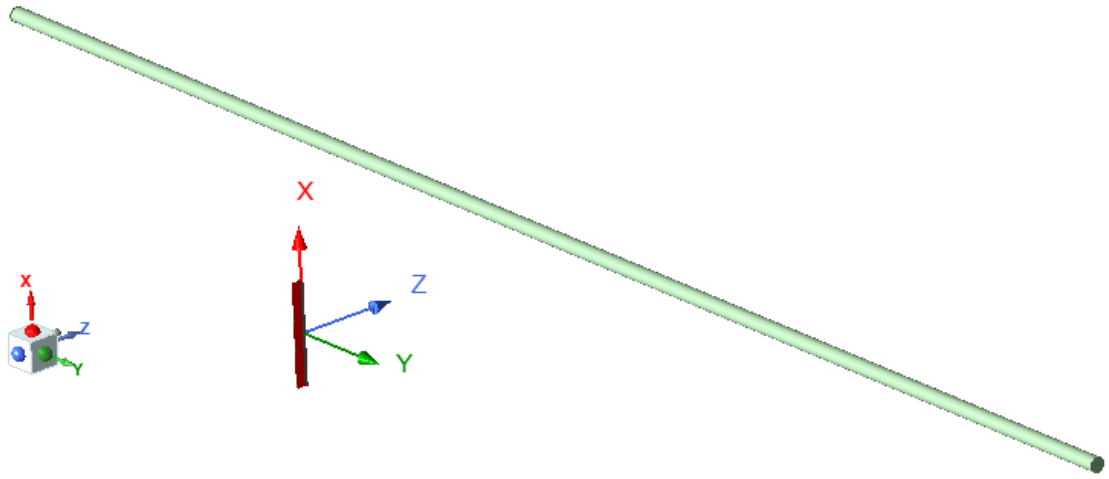

Figure 3.5: General setup of the 1×21 array antenna and pole obstruction simulation in HFSS, with a 5 m long PEC pole centered at x=0, aligned with the y-axis and at the distance z from the array antenna, and with the antenna designed for scanning in the H-plane/azimuth plane/xz-plane.

For all simulations in Ansys HFSS, unless otherwise stated, the mesh convergence was set to a maximum of 0.005 such that errors of less than $10 \cdot \log_{10}(0.005) = -23.0$ dB could be expected (which is very close to zero) without the simulation time or required computation power to become immense. Hence, the obtained simulation results were reliable and do not stray too much from the true values as the simulations also were set up with proper methods, e.g. with the use of FE-BI boundaries and/or IE regions. It was important to implement suitable measuring methods in Ansys HFSS in order to obtain accurate simulation data, e.g. results that can be compared to the corresponding outcomes in practice, and to reduce the required simulation time. In order to perform simulations with the designed array antenna, the whole antenna and at least a twentieth (1/20) of the simulation wavelength around it was covered with an air cell (due to it being a requirement for the FE-BI boundary) after which a FE-BI boundary was assigned to all the faces of the air box. This method was used because FE-BI boundaries are suitable for meshing designs containing a mix of components of different materials and varying sizes. Hence, both accurate and faster meshing was achieved for the array antenna. Instead, for meshing of the pole obstruction made out of PEC, an IE region was assigned to all the faces/surfaces of the pole because this method effectively meshes single large metallic objects. Further, for meshing of the pole obstruction as the different designed shells were added to the model, the implemented method depended on the material of the shell. For the cases where the shell was *not* made out of PEC, an air cell was added around the pole and shell such that at least a twentieth (1/20) wavelength of air edges was obtained, e.g. as done for the array antenna, after which the air box faces were assigned a FE-BI boundary. This method allowed for simula-

tions to be performed with all the shells, however for the cases where the shell was made out of PEC, the whole structure was simply assigned an IE region yielding an immensely faster simulation time than if the FE-BI method was implemented. For detailed descriptions of how to assign FE-BI boundaries or IE regions in Ansys HFSS, please refer to Appendix B.

3.3 Shell designs for pole obstruction cloaking

In this section, different 'shells' implemented for antenna obstruction cloaking are introduced. Section 3.3.1 explains the setup of a thin narrowband radiation material FGM-125 (shell 1) around the pole obstruction, and Sections 3.3.2 and 3.3.3 introduce a rhomb structure made out of PEC (shell 2) or wideband absorbent material (shell 3), respectively. In Sections 3.3.2 and 3.3.3, three rhomb point angles 30°, 37.5° and 45° were investigated, after which the design with rhomb point angle 45° was selected due to it performing among the best in terms of yielding large realized gain and low average sidelobe level in the far field behind the obstruction and due to this structure being possible to mesh and simulate in Ansys HFSS for the more complex design of shell 3. Further, Section 3.3.4 explains how shell 2 of the PEC rhomb was supplemented with a dielectric outer edge and PEC strips along the circumference of the structure (shell 4). Lastly, Section 3.3.5 investigates the required electromagnetic material characteristics of a layered meta-material cloak (shell 5) and how such a non-practical solution can be realized.

It was chosen to investigate the performance of the narrowband absorbent (shell 1) as it is a typical absorbent used for radar applications, and as it was not apparent if adding the absorbent around a thin pole would cause more harm than simply leaving the obstruction uncloaked. Further, the rhomb shaped shells (shells 2, 3 and 4) were designed due to the intuitiveness that the point of the structures splits electromagnetic waves propagating toward it and somewhat guides them along its sides. Hence, it was expected that the rhomb structures would result in decreased scattering at the obstruction and perhaps in increased realized gain in its direction as long as the rhomb point was facing the center of the antenna. To specify, though the problem scenario was only evaluated with the pole directly in front of the array antenna in this project, had the pole been placed at an angle in front of the antenna the point of the designed rhomb structures should, of course, be directed towards the array antenna center, which should yield similar cloaking characteristics. Lastly, it was chosen to investigate the characteristics of the meta-material cloak (shell 5) due to it being a hot topic and as previous works have reported its effectiveness, as described in Section 2.2.3.1. However, as later explained in Section 3.3.5 this non-practical solution was not evaluated further in the antenna and obstruction simulation described in Section 3.2 due to it being demanding to simulate in terms of required computer RAM, due to a practical solution being complex and time consuming to obtain and because other more simple solutions proved to be effective (e.g. the other evaluated shell designs).

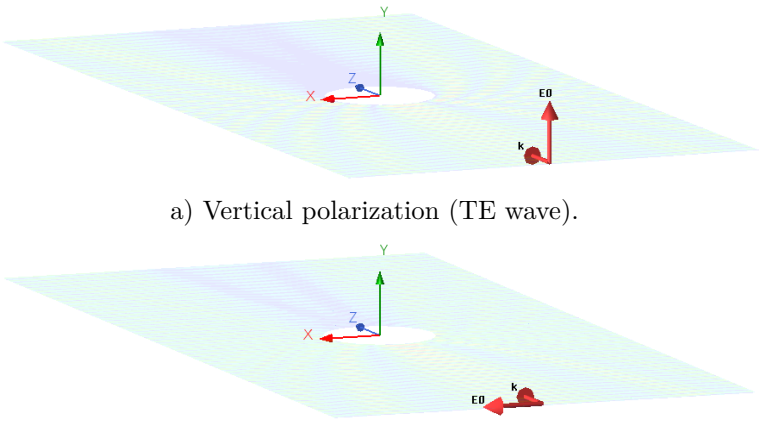

a) Vertical polarization (TE wave).

b) Horizontal polarization (TM wave).

Figure 3.6: Specification of coordinate system and incident waves for simulation of the total real electric field magnitude by propagating incident waves of different polarization toward a PEC pole/an obstruction.

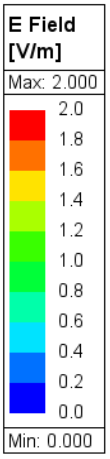

Figure 3.7: Specification of the real electric field magnitude color scale used for all the incident wave plots.

Throughout this section, the performances of the different designed shells are visualized by showing the resulting real electric field magnitudes $\Re(E)$ as incident waves hit them. Figure 3.6 defines the simulation setup as a plane wave of vertical polarization and horizontal polarization, respectively, was excited toward the pole/obstruction. The environment for simulating the resulting electric fields as incident plane waves were propagated against an obstruction was set up using PML boundaries and a Lattice Pair in Ansys HFSS, which is described in Section B.2 in Appendix B. For all shown electric field plots in this section, the figures show the total real electric field magnitude as an incident wave of vertical or horizontal polarization was propagated towards the pole without an angle, unless otherwise stated. Further, for all incident wave plots the scaling in Figure 3.7 of real electric field magnitude 0 to 2 [V/m] was used, and for all plots the electric fields are shown for the phase 0° (e.g. simply for snapshots taken at the time $t = 0$ s).

3.3.1 Shell 1: Thin narrowband radiation absorbent FGM-125 by Eccosorb™

The first shell investigated was a typical quarter wavelength thin radiation absorbent material 'FGM-125' manufactured by Eccosorb™. This absorbent of thickness 3.18 mm was selected due to its absorbent performance at 9.5 GHz. It can be understood that the absorbent is a type of Dallenbach layer through calculations for the absorbent's electrical wavelength, as described in Section 2.2.2.1.1. The relative permittivity of FGM-125 has been measured to be roughly $\epsilon_r \approx 7.16$ at 9.5 GHz, yielding an electrical quarter wavelength of

$$\frac{\lambda_{FGM-125}}{4} \approx \frac{c}{4 \cdot f_c \cdot \sqrt{\epsilon_r}} \approx 2.95 \text{ [mm]} \tag{3.2}$$

at 9.5 GHz using Equation (2.17), i.e. a value rather close to the manufactured absorbent thickness of 3.18 mm as could be expected. Figure 3.9 visualizes the setup of FGM-125 around the pole obstruction in Ansys HFSS. In order to verify the absorbent characteristics of FGM-125, the material was added in Ansys HFSS following the specifications in its data sheet [22] after which its S-parameters were measured using the Ansys HFSS model visualized in Figure 3.8. Figure 3.8 shows the absorbent material (in pink) placed in front of a PEC box (in green) corresponding to the obstruction. Through adding a longer air box and assigning a Floquet Port to its short end side, and Lattice Pairs on all side faces of sheets covering the whole model extending the air, absorbent and PEC boxes into infinity on all sides, the reflected effect from the absorbent could (due to the usage of the Floquet Port and Lattice Pairs) be accurately and quickly measured through propagating incident waves with different incident angles toward it. The defined dimensions in Figure 3.8 are specified in Table 3.2, and Appendix B.3 details the setup of the model using the Floquet Port and the Lattice Pairs.

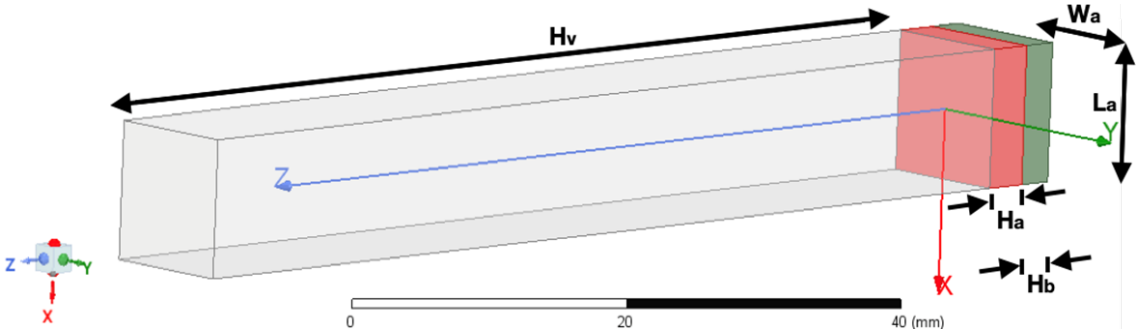

Figure 3.8: Visualization of the HFSS setup for simulating the reflected effect in the air box (in transparent white) from the absorbent FGM-125 (in pink) in front of a PEC box (in green). The defined dimensions are specified in Table 3.2.

Table 3.2: Specification of the FGM-125 absorbent reflected effect simulation's dimensions, defined in Figure 3.8.

Variable	L_a	W_a	H_a	H_b	H_v
Value [mm]	10.0	10.0	3.18	2.70	80.0

Figure 3.10 shows the resulting S-parameters for the absorbent FGM-125 for the frequencies 2–18 GHz, which agreed well with the absorbent characteristics given in the data sheet. The different curves in Figure 3.10 show reflected effect as the absorbent was hit with a plane wave of ϕ-polarization, i.e. vertical polarization, for different incident angles. Hence, as lower reflections suggested more absorption by the material and the reflected effect was lower than -10 dB for the incident angle range of interest (e.g. a rather high return loss RL of 10 dB), the absorbent could be expected to work well for scattering cancellation at (and around) 9.5 GHz.

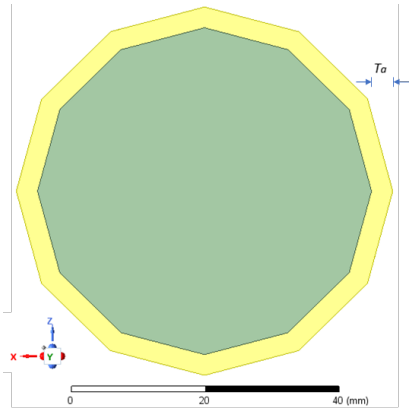

Figure 3.9: Setup of the thin radiation absorbent material FGM-125 of thickness $T_a = 3.18$ mm (in yellow) around the pole (in green, which is extended along the y-axis) in the simulation environment described in Section 3.2.

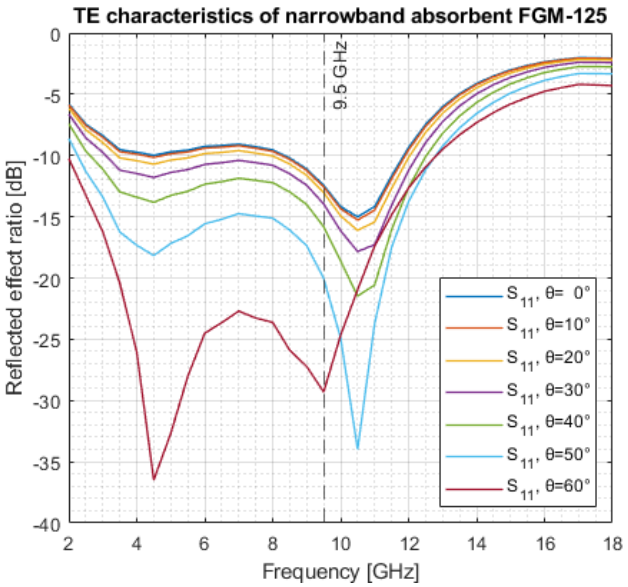

Figure 3.10: Reflected effect ratio [dB] of absorbent FGM-125 simulated in Ansys HFSS visualizing the reflections at the absorbent material for different incident angles/steering angles θ. Lower reflections suggest more absorption by the material.

Figure 3.11 shows the resulting electric fields as a vertically polarized incident wave with angle 0° was propagated toward the design of shell 1 around the pole obstructions of diameters 5 cm and 10 cm, and Figure 3.12 shows the corresponding results for horizontal polarization. As can be seen by comparing the electric fields for the simulations without and with shell 1 in Figure 3.11, the FGM-125 absorbent effectively reduced scattering at the pole surface for both of the pole thicknesses. However, due to both the increased total radius of the obstruction and the absorbent characteristics of shell 1, the real electric field magnitude "behind" the obstruction was reduced somewhat more. That vertical polarization yielded the most scattering as the propagating incident waves were short circuited along the vertically extended metallic pole can be seen by comparing Figure 3.11a) with Figure 3.12b) and Figure 3.11c) with Figure 3.12c), e.g. the results for the 5 cm and 10 cm diameter poles without shells, respectively, for vertical and horizontal polarization. Further, through studying Figure 3.12 it can also be seen that shell 1 happened to work well for horizontal polarization too. This was due to the FGM-125 absorbent yielding similar results for horizontal polarization as for vertical polarization at 9.5 GHz (though not shown in the report). That is, the FGM-125 yielded less than -10 dB reflected effect for all incident angles/steering angles up to $\theta = 60°$ for horizontal polarization too at 9.5 GHz (e.g. a rather high return loss RL of 10 dB), like the absorbent's vertical polarization results shown in Figure 3.10.

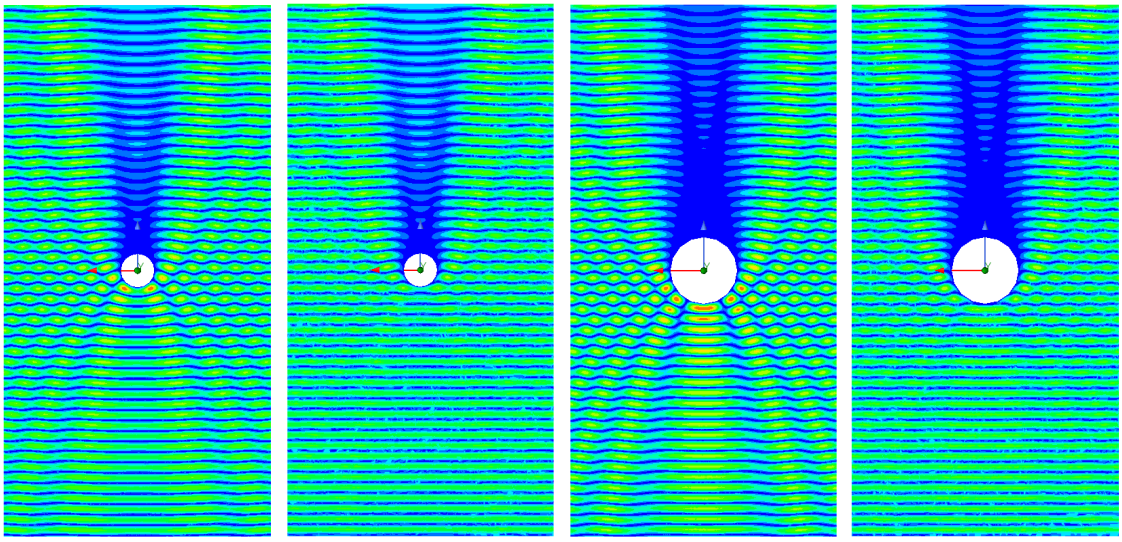

a) 5 cm pole. b) With FGM-125. c) 10 cm pole. d) With FGM-125.

Figure 3.11: Real electric field magnitude ($\Re(E)$) as an incident wave with vertical polarization hits 5 cm and 10 cm diameter poles, without and with FGM-125 (shell 1). The electric field magnitude color scale is shown in Figure 3.7.

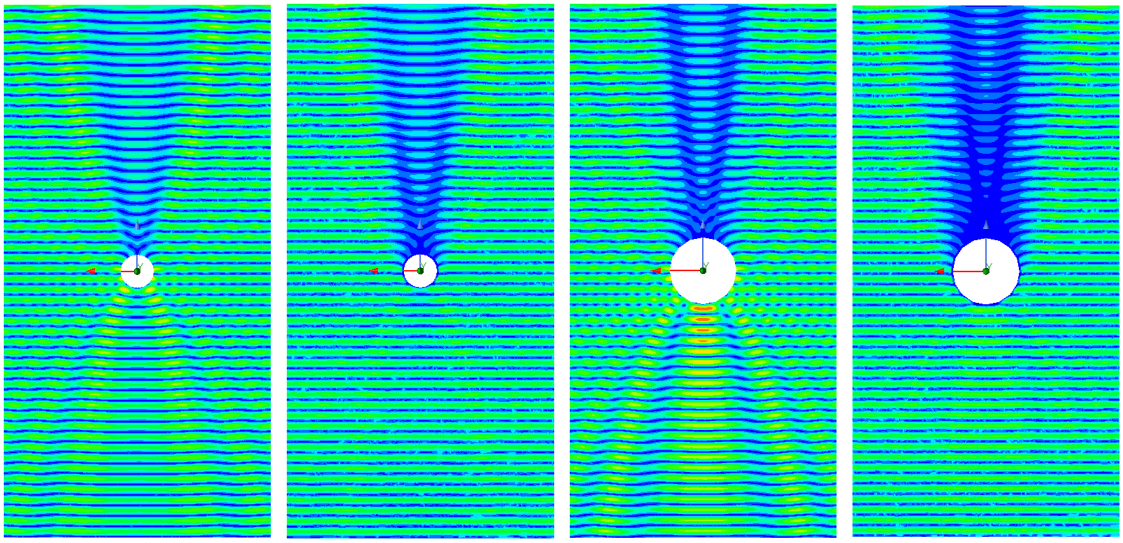

a) 5 cm pole. b) With FGM-125. c) 10 cm pole. d) With FGM-125.

Figure 3.12: Real electric field magnitude ($\Re(E)$) as an incident wave with *horizontal* polarization hits 5 cm and 10 cm diameter poles, without and with FGM-125 (shell 1). The electric field magnitude color scale is shown in Figure 3.7.

3.3.2 Shell 2: Rhomb made out of PEC

The second shell investigated was a rhomb structure made out of PEC. In order to investigate which rhomb design performed best in terms of realized gain and average sidelobe level, initial simulations were made for three different rhomb point angles $2\alpha = 30°$, $37.5°$ and $45°$, after which the most suitable one was selected and simulated further (which turned out to be the rhomb design with the point angle $2\alpha = 45°$, as is described later in this section and shown and motivated in Section 4.1.2). Figure 3.13 shows how the dimensions of the rhomb were calculated and defines the rhomb point angle 2α. In order to make the design realistic, the rhomb structure was designed to have a smallest edge of $R_1 = 0.5$ mm such that any designed rhomb shell could easily be mounted around the pole obstruction in practice. Hence, knowing the pole radius $R_{pole} = 25$ mm or 50 mm and the smallest edge $R_1 = 0.5$ mm the required height H_{abs} of the triangle structure and the required added distance R_2 could be calculated for any rhomb point angle 2α. That is, using basic trigonometrics the relations

$$\begin{aligned} \sin(\alpha) &= \frac{R_{pole} + R_1}{H_{abs}} \rightarrow H_{abs} = \frac{R_{pole} + R_1}{\sin(\alpha)} \\ \tan(\alpha) &= \frac{R_{pole} + R_2}{H_{abs}} \rightarrow R_2 = \tan(\alpha) \cdot H_{abs} - R_{pole} \end{aligned} \tag{3.3}$$

were used in order to generally calculate the dimensions of the triangles for any rhomb point angle 2α [rad] such that the rhomb structure could automatically/easily be modelled in Ansys HFSS for different variations. Figure 3.14 visualizes the PEC shells simulated in Ansys HFSS, with rhomb point angles $2\alpha = 30°$, $37.5°$ and $45°$, respectively.

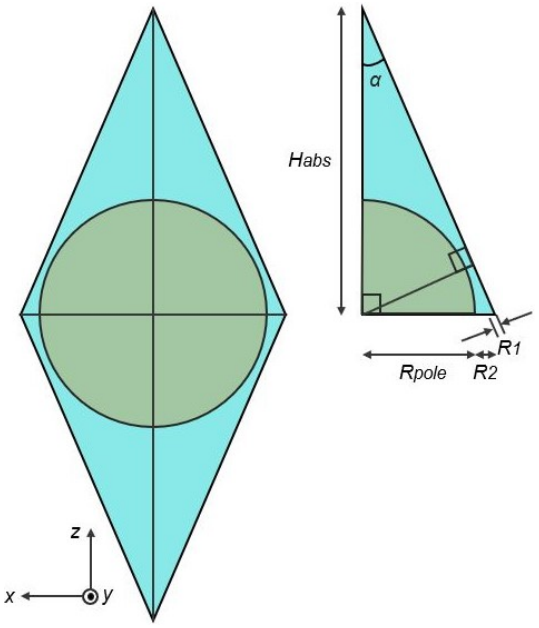

Figure 3.13: Specification of the dimensions of the designed rhomb structure(s) around the pole(s). The angle α denotes half the rhomb point angle.

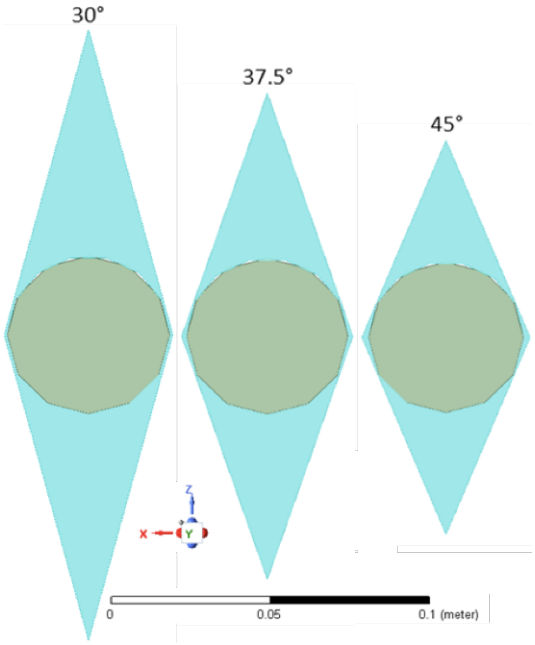

Figure 3.14: Setup of the rhomb made out of PEC around the pole (which was extended along the y-axis) in the simulation environment described in Section 3.2 for different rhomb point angles. The dimensions of the rhombs were calculated as described by Equation (3.3) and Figure 3.13 (where α denotes half of the described rhomb point angles).

Figure 3.15 shows the resulting real electric fields as a vertically polarized incident wave with angle 0° was propagated toward the designs of shell 2 with rhomb point angles 30°, 37.5° and 45°, respectively, around the pole obstructions of diameters 5 cm and 10 cm, and Figure 3.16 shows the corresponding results for horizontal polarization. By studying the electric fields it can be seen that the PEC rhombs effectively split the electric waves, causing much less back scattering than for the cases without shell 2, and that the different designs for shell 2 worked for both vertical and horizontal polarization (as expected, though, the shell did not perform as well for vertical polarization as it did imply the worst case scenario in terms in scattering). The back scattering was mostly due to the rhomb point being hit by the incident wave, and the red areas of higher real electric field magnitude in Figures 3.15 and 3.16 occurred as the electric waves were being steered/guided by the rhomb structure such that both constructive and destructive interference occurred in the forward direction. As can be seen by studying the electric fields "behind" the obstructions in Figure 3.15 for the different rhomb point angles, the design of shell 2 with the angle $2\alpha = 45°$ yielded a higher electric field for both thickness variations of the pole obstruction. Through simulations of the three different designs of shell

2 in the antenna and obstruction simulation environment in Ansys HFSS described in Section 3.2 for the distance 3 m (selected due to it being a medium distance from the antenna), it was confirmed that shell 2 with the rhomb point angle $2\alpha = 45°$ yielded the highest or high realized gain and, hence, it was selected as the final design for shell 2 as it also corresponded to the smallest rhomb structure and, thus, was the more suitable shape for the slightly more complicated design of shell 3 which was tough to simulate in Ansys HFSS in terms of computer power (e.g. required computer or server RAM). To specify, identical rhomb point angles for the different shells were desired for qualitative comparisons of the results. The obtained results for the three different designs of shell 2 as they were simulated in the antenna and obstruction simulation environment with the obstructions at the distance 3 m from the array antenna are shown in Figure 4.6 in Section 4.1.2.

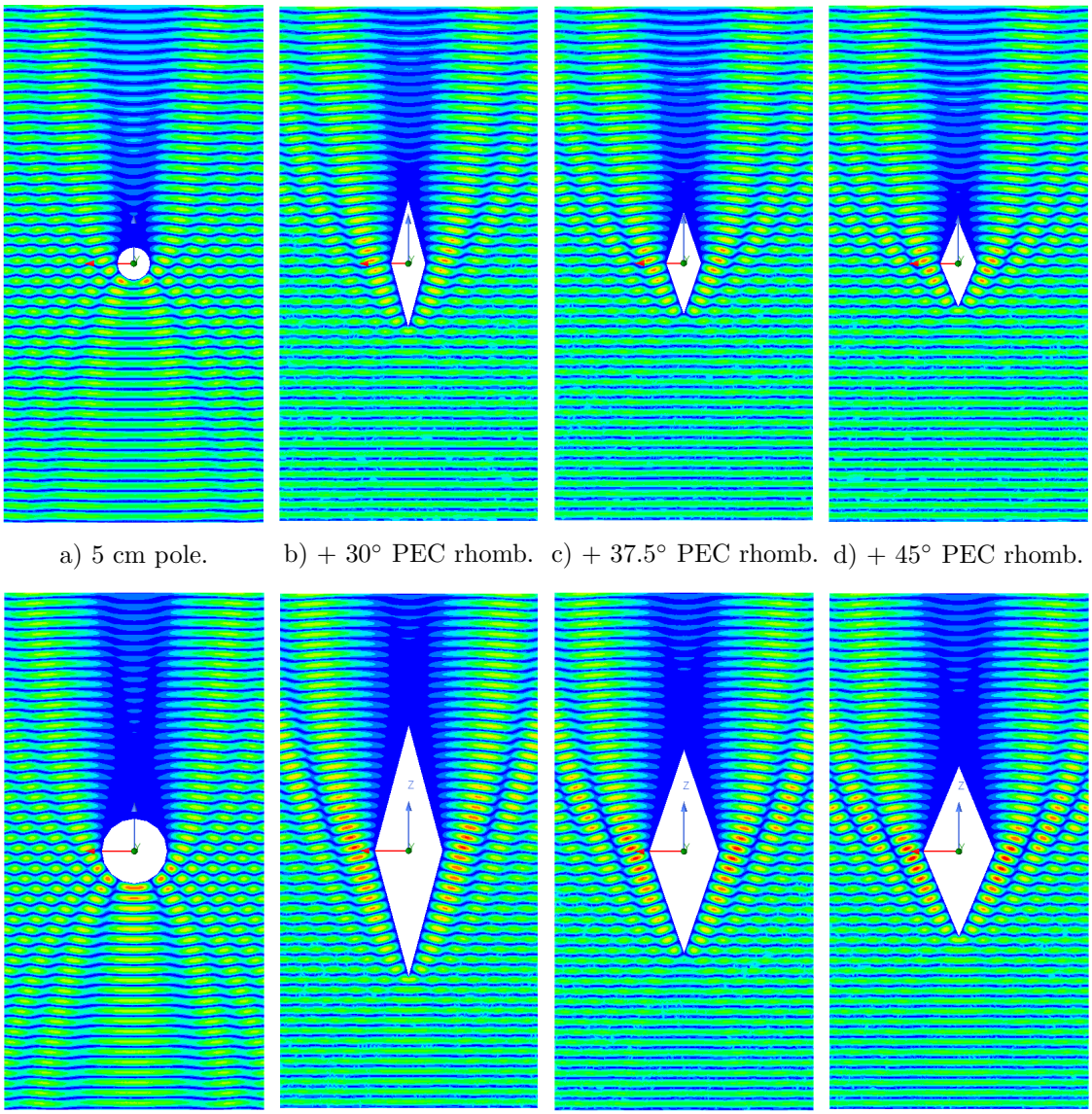

a) 5 cm pole. b) + 30° PEC rhomb. c) + 37.5° PEC rhomb. d) + 45° PEC rhomb.

e) 10 cm pole. f) + 30° PEC rhomb. g) + 37.5° PEC rhomb. h) + 45° PEC rhomb.

Figure 3.15: Real electric field magnitude ($\Re(E)$) as an incident wave with vertical polarization hits 5 cm and 10 cm diameter poles, without and with PEC rhombs (shell 2) with point angles 30°, 37.5° and 45°, respectively. The electric field magnitude color scale is shown in Figure 3.7.

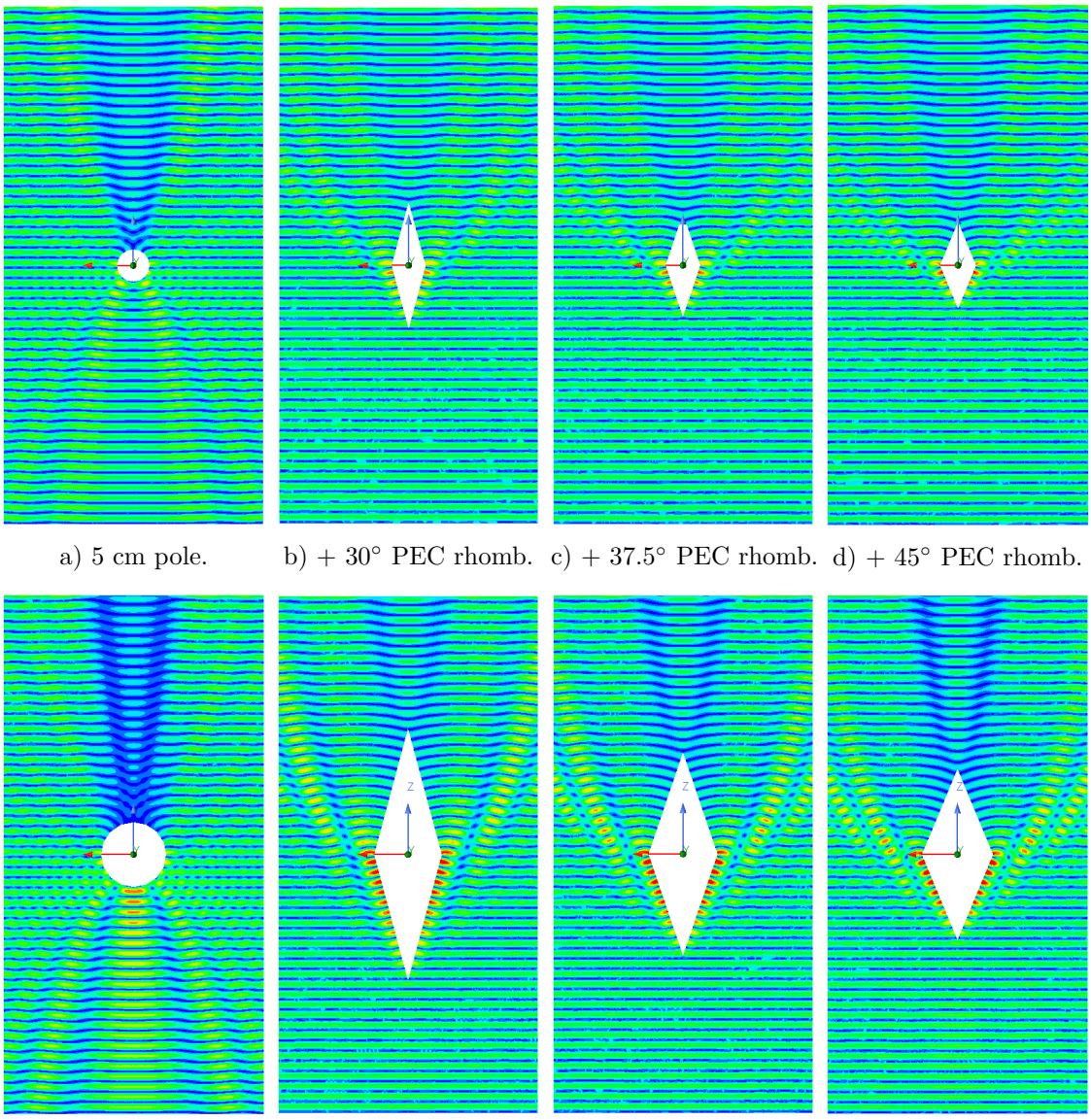

a) 5 cm pole. b) + 30° PEC rhomb. c) + 37.5° PEC rhomb. d) + 45° PEC rhomb.

e) 10 cm pole. f) + 30° PEC rhomb. g) + 37.5° PEC rhomb. h) + 45° PEC rhomb.

Figure 3.16: Real electric field magnitude ($\Re(E)$) as an incident wave with *horizontal* polarization hits 5 cm and 10 cm diameter poles, without and with PEC rhombs (shell 2) with point angles 30°, 37.5° and 45°, respectively. The electric field magnitude color scale is shown in Figure 3.7.

3.3.3 Shell 3: Rhomb made out of a wideband radiation absorbent of increasing conductivity

The third shell that was investigated was a rhomb structure exactly as the PEC rhomb described in Section 3.3.2, but with multiple layers of a wideband radiation absorbent material with a conductivity gradient instead of the PEC material. As for the PEC rhomb (shell 2), three different rhomb point angles 2α were investigated for shell 3, which results' also played a part in which final rhomb design was selected. The implemented absorbent of increasing conductivity throughout the material, which design followed the theory in Section 2.2.2.2.1, was created by

layering multiple sheets with material permittivity $\epsilon_r = 1.8$ and permeability $\mu_r = 1$ (e.g. non magnetic materials) with different conductivity values within the range $\sigma_1 = 0.17$ to $\sigma_2 = 2.65$ S/m (such that the layer closest to the pole had the highest conductivity). Hence, the different layers together approximated the continuous conductivity

$$\sigma(z_{abs}) = \frac{\sigma_2 - \sigma_1}{H_{abs}} \cdot z_{abs} + \sigma_1 \tag{3.4}$$

throughout the absorbent where z_{abs} denotes the distance into it (from the outer layer and inwards) in the same length unit as the absorbent height H_{abs}. As described in Section 2.2.2.2.1, the increasing conductivity throughout the material causes the field attenuation to increase along with it. The sheets were designed to be of thickness 5 mm for all layers, with an exception for the outer layer which was given a residual thickness such that the resulting rhomb design would have the triangle heights H_{abs}, as described in Section 3.3.2.

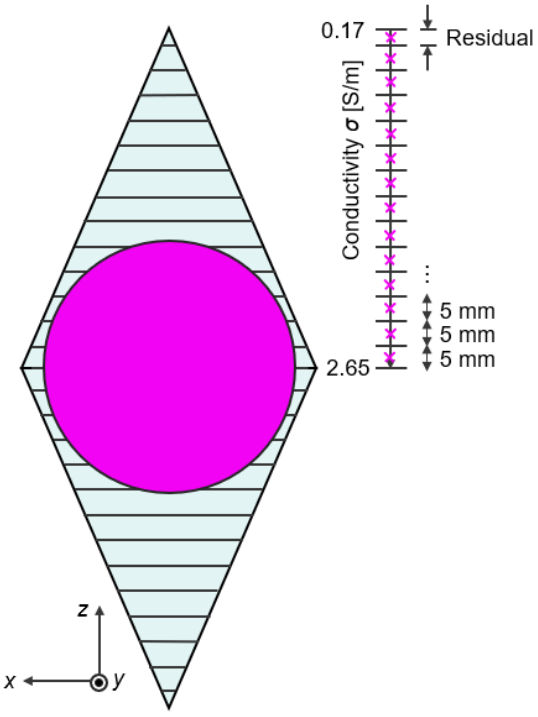

Figure 3.17: Specification of the assignment of the rhomb absorbent's sheet conductivity σ chosen in the range 0.17–2.65 S/m for the rhomb with point angle $2\alpha = 45°$.

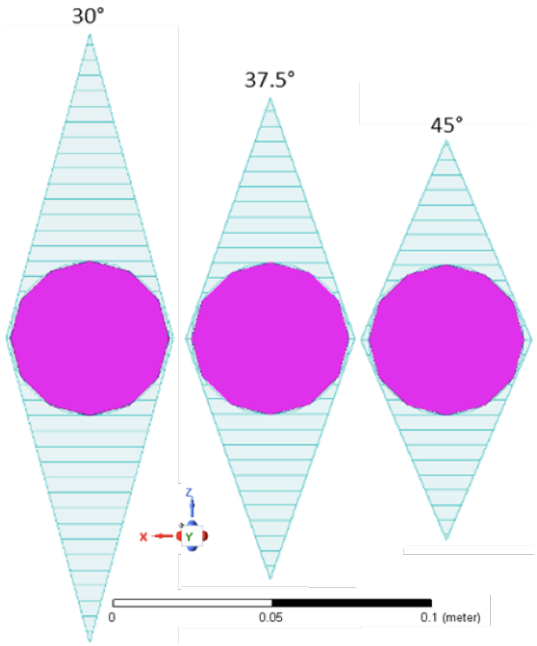

Figure 3.18: Setup of the rhomb made out of the wideband radiation absorbent material around the pole (which was extended along the y-axis) in the simulation environment described in Section 3.2 for different rhomb point angles. The dimensions of the rhombs were calculated as described by Equation (3.3) and Figure 3.13 (where α denotes half of the described rhomb point angles).

Figure 3.17 exemplifies how the sheet conductivity was selected for each layer for the designed rhomb with point angle $2\alpha = 45°$ with 13 layers of thickness 5 mm and one outer residual layer. As exemplified by the joint axis with conductivity and with length into the absorbent in Figure 3.17, the sheet conductivity for each layer was selected through dividing the conductivity range into the corresponding intervals obtained for the layer thicknesses and selecting the middle of each interval. Hence, the layers' conductivity for different designed rhombs could easily be obtained through calculations of the absorbent height H_{abs} (e.g. the height of the triangles) and the resulting number of absorbent layers. Figure 3.18 visualizes the wideband absorbent shells simulated in Ansys HFSS, with rhomb point angles $2\alpha = 30°$, $37.5°$ and $45°$, respectively.

In order to verify that the layered absorbent with sheets of increasing conductivity worked as intended, simulations for obtaining its S-parameters were performed using the same method as previously for the FGM-125 absorbent in Section 3.3.1. Figure 3.19 shows the obtained reflected effect ratios for different incident angles of the vertically polarized plane waves propagated toward the absorbents with thicknesses H_{abs} as a result of the rhomb angles $2\alpha = 30°$, $37.5°$ and $45°$ for the poles of diameter 5 cm and 10 cm, respectively. That is, the simulations for the S-parameters were made for different stretches of the conductivity from $\sigma_1 = 0.17$ S/m to $\sigma_2 = 2.65$ S/m (e.g. just different thicknesses of the absorbent) before the designed absorbents were structured/cut out to their corresponding rhomb shapes in order to verify that the designed gradients worked as intended. As can be seen for all the different designs of the wideband absorbent, all variations yielded reflected effect ratios of less than -15 dB (e.g. rather high return losses of 15 dB) for all the evaluated incident angles at and around 9.5 GHz, suggesting that all designed variations of the wideband absorbent would effectively absorb vertical illumination at and about the desired frequency. Of course, as the absorbents were modified in shape the structures' absorbent characteristics were somewhat changed, but the performed simulations enabled simple verification of the designed materials and direct comparisons with the corresponding reflected effect of the defined absorbent FGM-125 (e.g. the absorbents' characteristics could be compared with Figure 3.10).

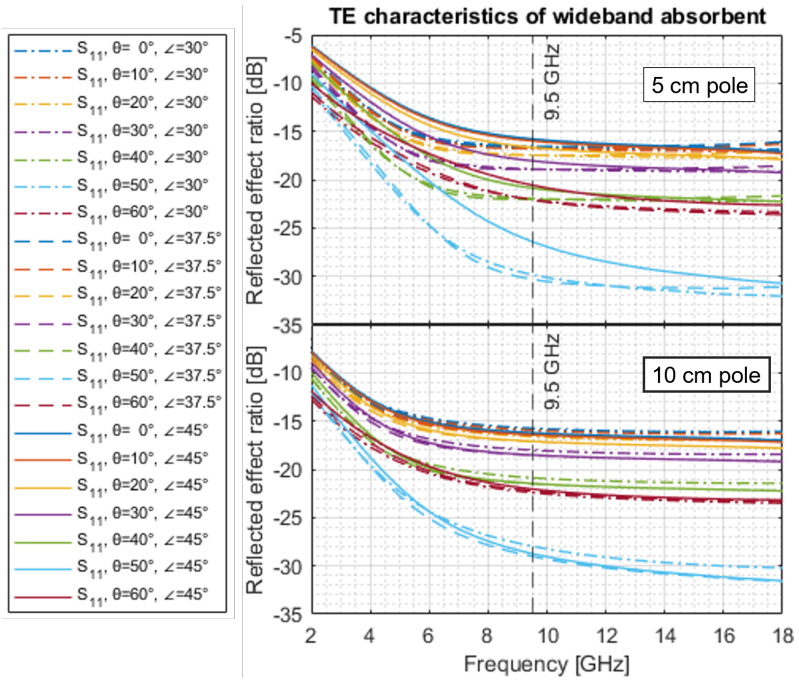

Figure 3.19: Reflected effect ratio [dB] of the wideband absorbents for different thicknesses (e.g. variations of rhomb point angles 2α and pole diameters) simulated in Ansys HFSS (using the same method as described for the FGM-125 absorbent in Section 3.3.1) visualizing the reflections at the absorbent material for different incident angles/steering angles θ. Lower reflections suggest more absorption by the material.

Figure 3.20 shows the resulting real electric fields as a vertically polarized incident wave with angle 0° was propagated toward the designs of shell 3 with rhomb point angles 30°, 37.5° and 45°, respectively, around the pole obstructions of diameters 5 cm and 10 cm, and Figure 3.21 shows the corresponding results for horizontal polarization. Through studying Figures 3.20 and 3.21 it can be seen that the designed absorbent worked well for both vertical and horizontal polarization. Further, by studying the electric fields it can be seen that the absorbent rhombs effectively removed the back scattering that occurred as shell 2 of the PEC rhomb was implemented, and that shell 3 reduced the scatterings from the sides of the rhomb structure in comparison. However, which can somewhat be seen by comparing Figure 3.20 with Figure 3.15, e.g. comparing the vertical polarization results of shell 3 and of shell 2, the absorbent rhombs seem to have yielded slight decreases of real electric field magnitude "behind" the obstructions. Further, as the design of shell 3 with rhomb point angle $2\alpha = 45°$ seemed to obtain the highest electric field magnitude behind the obstructions in Figure 3.20 and as that design performed well in terms of highest realized gain in the antenna and obstruction simulation at a distance of 3 m from the array antenna, similarly to the design of shell 2, and as it also was the less tough structure to simulate in Ansys HFSS, it was determined that the implemented rhomb point angle would be used for shell 3 as well (and, which is described in Section 3.3.4, also for shell 4 that too is shaped like a rhomb).

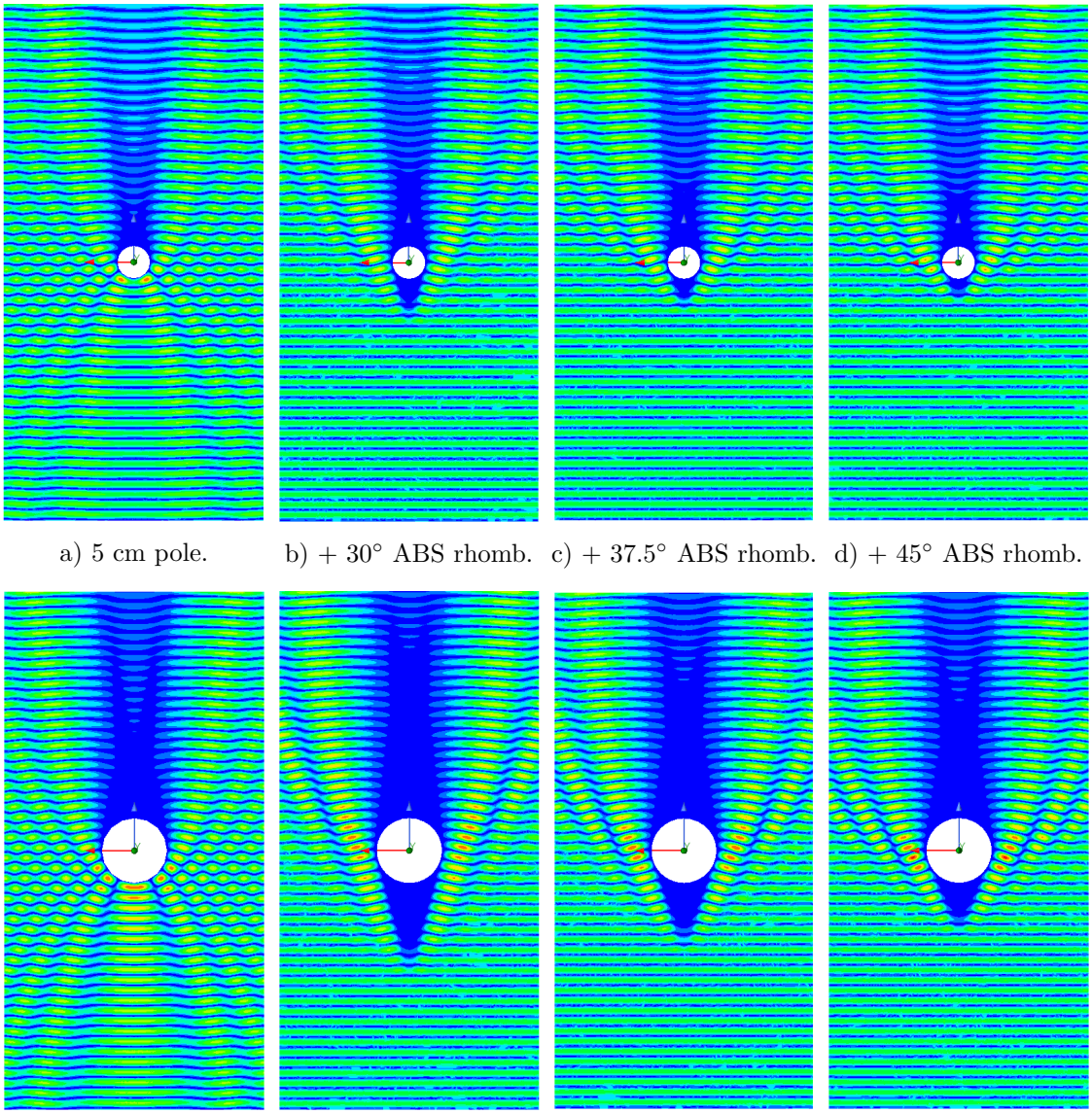

a) 5 cm pole. b) + 30° ABS rhomb. c) + 37.5° ABS rhomb. d) + 45° ABS rhomb.

e) 10 cm pole. f) + 30° ABS rhomb. g) + 37.5° ABS rhomb. h) + 45° ABS rhomb.

Figure 3.20: Real electric field magnitude ($\Re(E)$) as an incident wave with vertical polarization hits 5 cm and 10 cm diameter poles, without and with absorbent (ABS) rhombs (shell 3) with point angles 30°, 37.5° and 45°, respectively. The electric field magnitude color scale is shown in Figure 3.7.

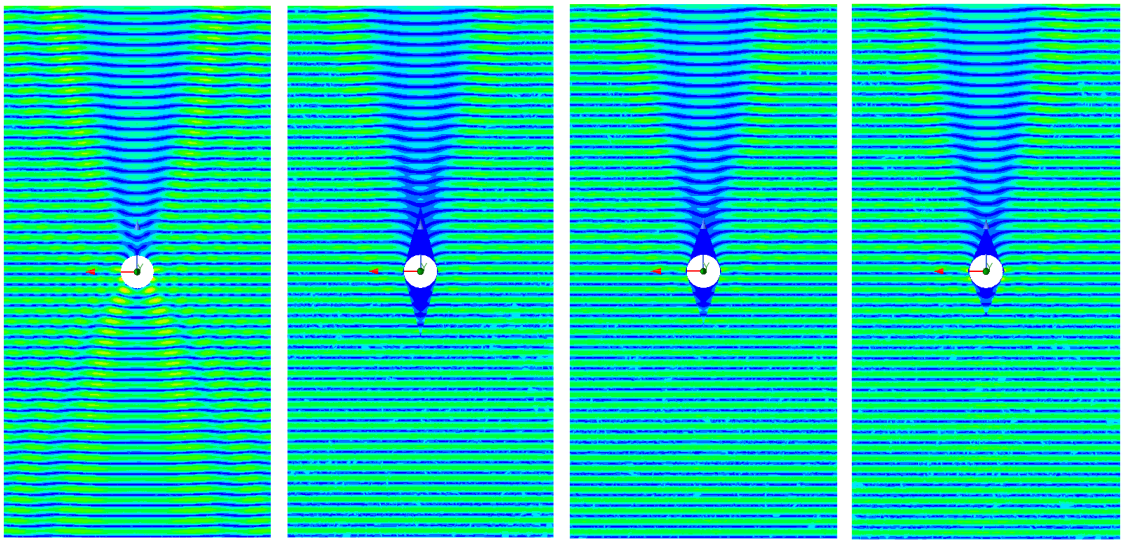

a) 5 cm pole. b) + 30° ABS rhomb. c) + 37.5° ABS rhomb. d) + 45° ABS rhomb.

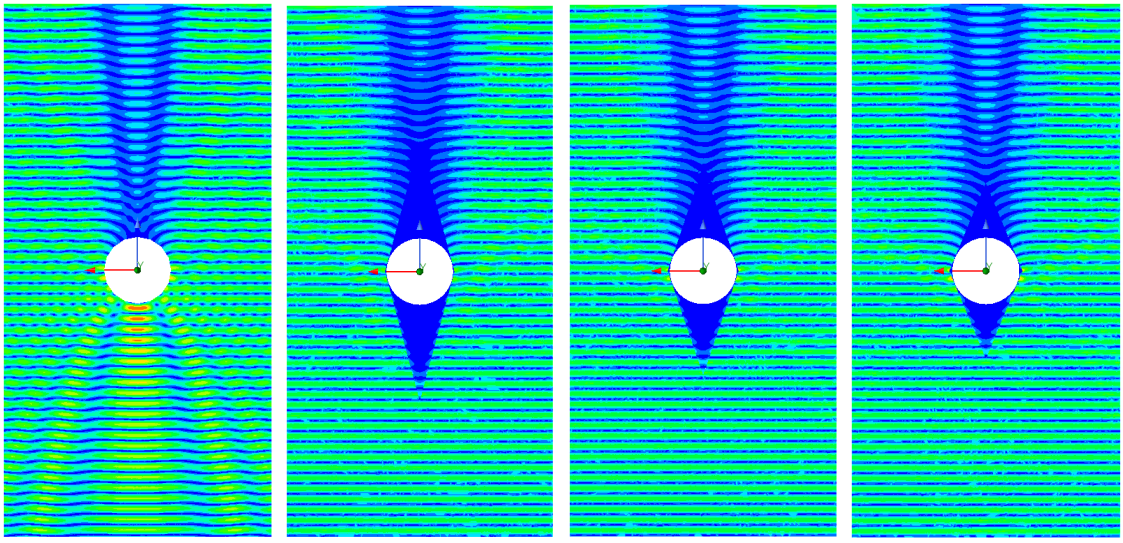

e) 10 cm pole. f) + 30° ABS rhomb. g) + 37.5° ABS rhomb. h) + 45° ABS rhomb.

Figure 3.21: Real electric field magnitude ($\Re(E)$) as an incident wave with *horizontal* polarization hits 5 cm and 10 cm diameter poles, without and with absorbent (ABS) rhombs (shell 3) with point angles 30°, 37.5° and 45°, respectively. The electric field magnitude color scale is shown in Figure 3.7.

3.3.4 Shell 4: Rhomb made out of PEC with added dielectric border and PEC strips

The fourth shell investigated was the PEC rhomb with point angle $2\alpha = 45°$ (shell 2) supplemented with an outer edge made out of dielectric material and multiple PEC strips going around the circumference of the structure. This design was evaluated due to previous works reporting its effectiveness in steering both vertically and horizontally polarized electric waves around it [5]. Figure 3.22 shows a slice of the designed structure, which in reality was extended along the y-axis for the total simulation pole length of 5 m. The PEC strips were added around the circumference

of the rhomb structure with thickness $T_s = 0.035$ mm and width $W_s = 2$ mm, as described by Figure 3.22 and Table 3.3 presenting the final design quantities. According to the previous works implementing the emulated cloak design [5], at least 2 PEC strips for each wavelength is necessary. As the slice in Figure 3.22 is of width $W_d = 10.5$ mm and the design was extended along the y-axis, it can be seen that it was chosen to design shell 4 with 3 PEC strips each wavelength (e.g. as $\lambda/3 = (31.6 \text{ mm})/3 = 10.5$ mm). The initial thickness of the substrate T_d was calculated as

$$T_d = \frac{\lambda}{4\sqrt{\epsilon_r - 1}} \tag{3.5}$$

where λ is the wavelength of the electromagnetic wave to be cloaked and ϵ_r is the relative permittivity of the substrate [5], after which the thickness was tuned based on simulation results in order to obtain the most effective design. Using the material Rogers TMM 4 with relative permittivity $\epsilon_r = 4.5$ as the dielectric substrate, the initial thickness was calculated to $T_d = 4.22$ mm, which was later tuned to $T_d = 4.45$ mm. Different design substrate thicknesses were tested through simulations in the antenna and pole obstruction setup described in Section 3.2, from which the design yielding the largest realized gain in azimuth angle $\theta = 0°$ and elevation angle $\phi = 0°$ was selected.

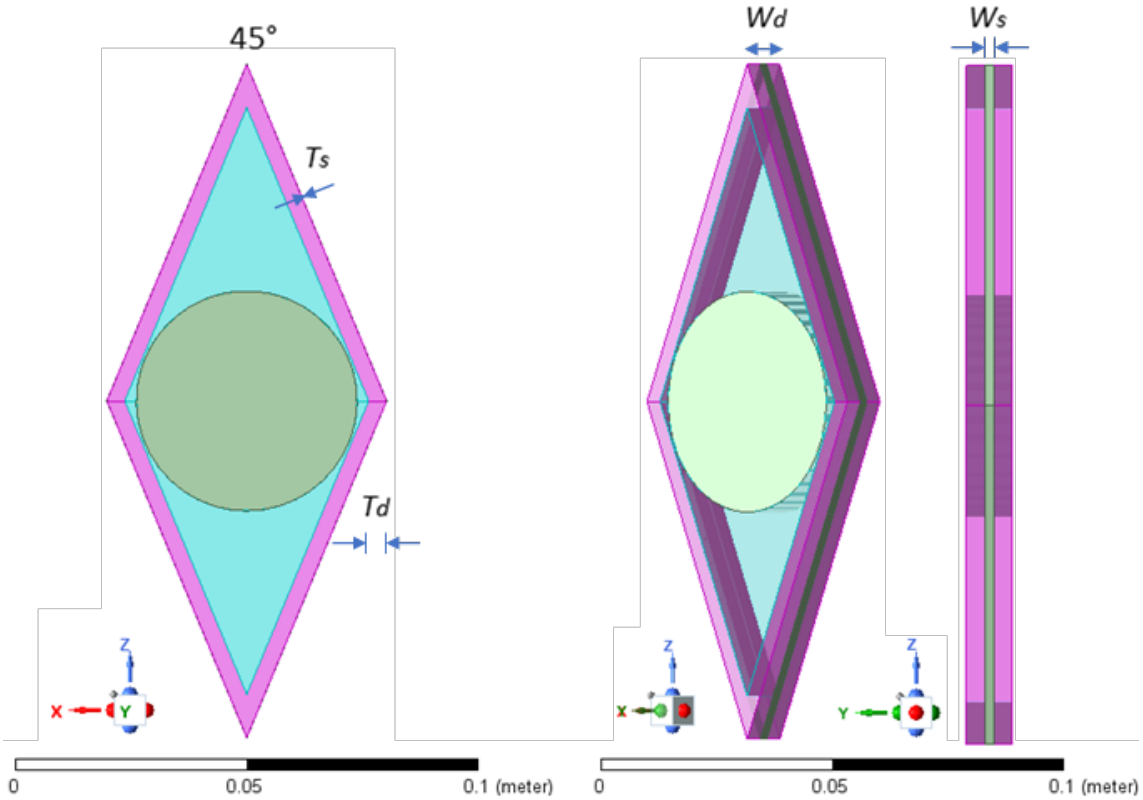

Figure 3.22: Setup of the structure made out of a PEC rhomb with point angle $2\alpha = 45°$ (shell 2), an outer dielectric boarder (in purple) and PEC strips around the circumference (in green), which was extended along the y-axis and placed around the pole in the simulation environment described in Section 3.2.

Table 3.3: Specification of the dimensions of the dielectric outer edge and stripes of shell 4.

Variable	T_d	T_s	W_d	W_s
Value [mm]	4.45	0.0350	10.5	2.00

To specify, the final design dimensions described in Table 3.3 were obtained by emulating previous works [5] for an implementation at 9.5 GHz, for which it was chosen to have 3 strips each wavelength, however the substrate thickness T_d was tuned around the calculated value obtained from Equation 3.5 such that cloak showed the best results in terms of realized gain. Unfortunately, the implemented model failed to imitate the solution proposed by the previous successful work [5] to its entirety. Though the final design of shell 4 yielded good results in this report in terms of realized gain and somewhat in terms of average sidelobe level in the forward direction in the H-plane, as is shown in Section 4.1.4, even better results would have been obtained if another dielectric material of lower permittivity had been assigned to the tips of the rhomb points. Likely, had shell 4 been designed properly there would not have been a need for tuning of the substrate thickness T_d either. In more detail, unnecessary scattering was the result of covering the whole underlying PEC rhomb with the high permittivity dielectric as the resulting model in fact did not have the required thickness of T_d as described by Equation 3.5 at the point tips (but, instead, a much thicker layer). Hence, when studying the results of shell 4 it should be kept in mind that it is very likely that the solution can perform even better in terms of realized gain and average sidelobe level than obtained with the final design in this report through some minor design changes. Hence, for implementation of a cloak such at shell 4, it is recommended to follow the detailed correct/successful design [5].

Figure 3.23 shows the resulting electric fields as vertically polarized incident waves with angles 0°, 15°, 30° and 45°, respectively, were propagated toward shell 4 around the pole obstructions of diameters 5 cm and 10 cm, and Figure 3.24 shows the corresponding results for horizontal polarization. Distinct from all other designed shells, it was chosen to also visualize the results of oblique incidences for shell 4 in this section due to it performing well in terms of retaining real electric field magnitude "behind" the obstruction (e.g. better than the other shells, though not shown in the report). As can be seen more qualitatively in Section 4.1.4, shell 4 did perform well even for oblique incidences (e.g. from sidelobes hitting the pole from an angle as the main beam was steered in the H-plane). By studying the electric fields it can be seen that the PEC strips successfully guided the waves around the circumference of the structures, and that shell 4 worked for both vertical and horizontal polarization (though, somewhat better for vertical polarization). Further, it can be seen that the structures effectively cloaked the pole obstructions even as the propagating waves reached the cloaks with different incident angles. However, as can be seen by the red areas in Figures 3.23 and 3.24 the structures did create areas with stronger real electric field magnitudes around the rhomb, especially at the rhomb points. Likely, the added dielectric outer border and PEC strips guiding the electric waves around the structure caused an increased amount of scattering at the PEC strips and especially at the rhomb points, which will cause losses in terms of realized gain and

result in higher average sidelobe levels for steering angles in the H-plane. However, please note that these complications might very well be possible to mitigate through the described design improvements.

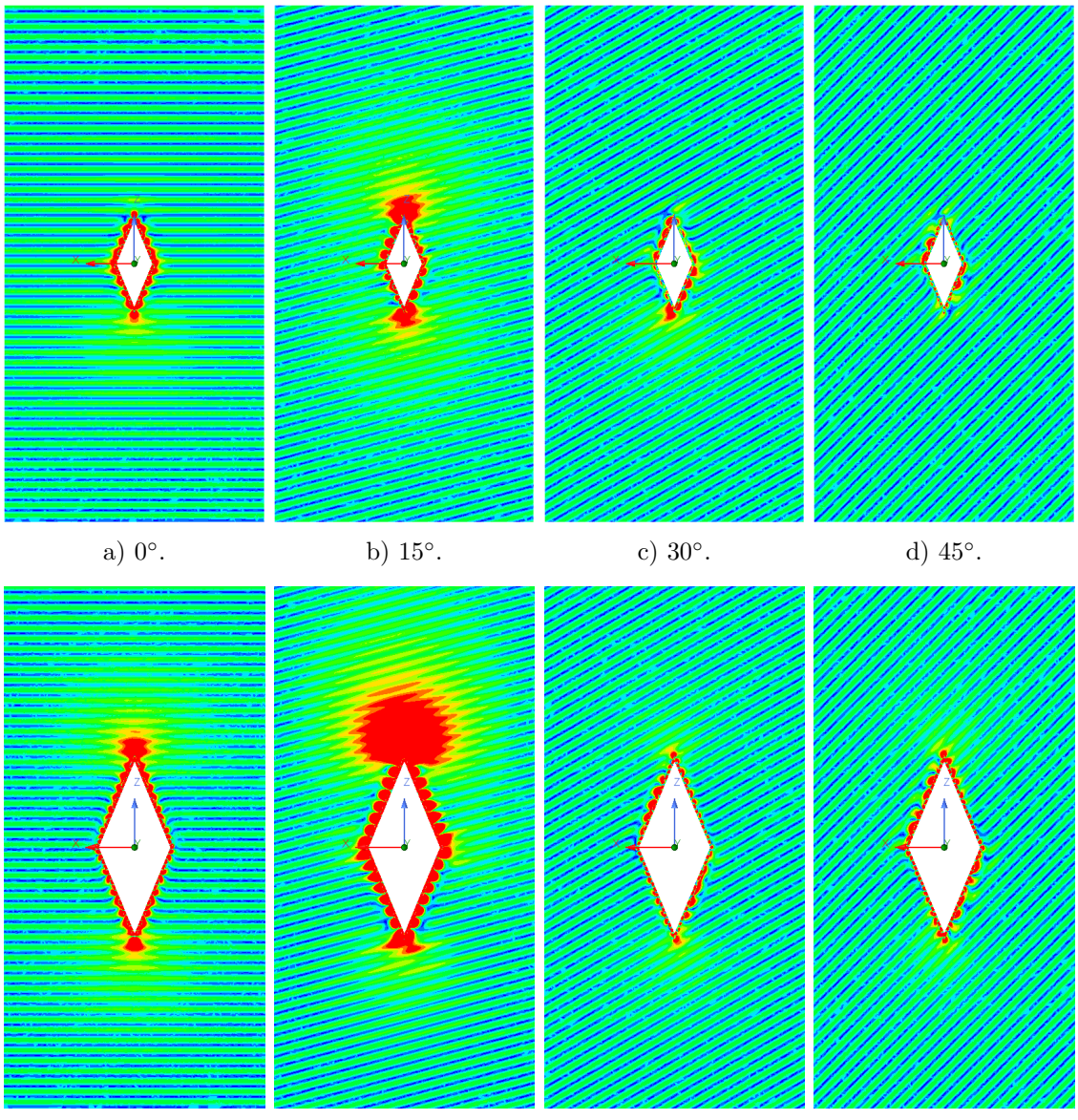

a) 0°. b) 15°. c) 30°. d) 45°.

e) 0°. f) 15°. g) 30°. h) 45°.

Figure 3.23: Real electric field magnitude ($\Re(E)$) as an incident wave with vertical polarization in a-d) hits 5 cm and in e-h) hits 10 cm diameter poles with PEC rhomb with dielectric outer edge and PEC strips around it (shell 4) with the incident angles 0°, 15°, 30° and 45°. The electric field magnitude color scale is shown in Figure 3.7.

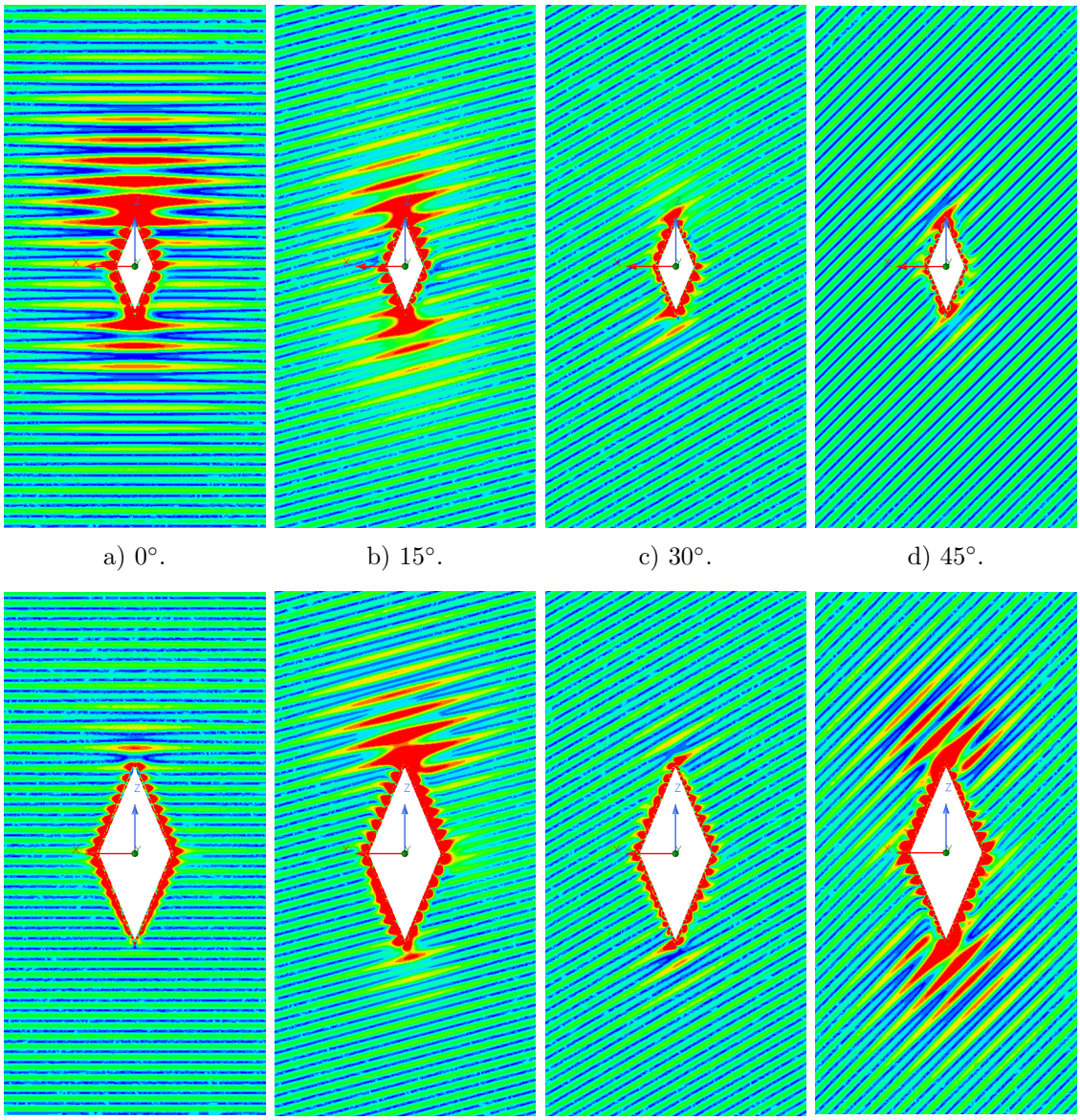

a) 0°. b) 15°. c) 30°. d) 45°.

e) 0°. f) 15°. g) 30°. h) 45°.

Figure 3.24: Real electric field magnitude ($\Re(E)$) as an incident wave with *horizontal* polarization in a-d) hits 5 cm and in e-h) hits 10 cm diameter poles with PEC rhomb with dielectric outer edge and PEC strips around it (shell 4) with the incident angles 0°, 15°, 30° and 45°. The electric field magnitude color scale is shown in Figure 3.7.

3.3.5 Shell 5: Layered meta-material cloak (non-practical solution)

The fifth shell examined was a theoretical layered meta-material cloak. Due to previous works reporting meta-material cloaks' effectiveness in guiding either vertically and horizontally polarized waves (depending on the design) around cylindrical obstructions, as described in Section 2.2.3.1, the theoretical vertical polarization cloak design described in this section was constructed for investigation of its performance.

As the theoretical layered meta-material cloak proved to be too heavy to mesh and simulate in Ansys HFSS (e.g. it required more RAM than was available), shell 5 was not implemented for simulations in the antenna and obstruction setup described in Section 3.2. However, it was decided that an investigation of the layered meta-material was to be done through simulating plane waves incident on the shell in order to evaluate if it is of any benefit to strive for such a solution in practice. Hence, shell 5 was analyzed due to it being an interesting electromagnetic cloak solution, and this section describes both how the layered meta-material cloaks were theoretically designed for the 5 cm and 10 cm diameter pole obstructions and tools that can be employed when trying to design a realizable version of the cloak.

The layered meta-material cloak was designed for vertical polarization following the theory in Section 2.2.3.1 for a selected cloak radius (defined from the centre of the cylindrical obstruction) of $b = 2a$ where a is the radius of the pole obstruction. Please note that the tensor component subscript 'z' in this section (and in the literature) refers to the cylinder axis, which in this project instead is along the y-axis (though, for the sake of simplicity, the subscript used in literature is retained here). As Equation (2.22) implies a very complicated meta-material design due to all the tensor components being functions of the radius r, it is desirable to simplify the design. Hence, as the electric field is polarized along the same axis as the cylinder pole the expression can be simplified to

$$\mu_r = \Big(\frac{r-a}{r}\Big)^2 \ , \ \mu_\theta = 1 \ , \ \epsilon_z = \Big(\frac{b}{b-a}\Big)^2 \tag{3.6}$$

which for the cloak radius of $b = 2a$ yields a required constant relative permittivity $\epsilon_r = 4$ throughout the cloak. As visualized in Figure 3.25 for both cloak designs (e.g. the cross section is scalable), shell 5 was constructed through adding multiple layers of theoretical meta-materials around the obstruction. For both pole obstruction diameters, the layered cloaks were constructed using 20 sheets, for which the layer material properties were calculated using Equation (3.6) with the values of r being the smallest radii to each layer (e.g. for each layer the radius to the ring's inner edge). Figure 3.26 shows the calculated and implemented values of the relative permeability throughout the cloaks, compared to the corresponding continuous permeabilities which were calculated using Equation (2.22). It was decided to obtain the required material properties through layering sheets in Ansys HFSS instead of employing a single material with coordinate dependent properties due to the layered design being more realistic. As can be understood by studying Figure 3.26, implementing more layers in the cloak implies making the design more accurate. However, designing the cloak with more layers with different material properties also implies longer simulation time and an increased difficulty in reconstructing the shell in practice. Hence, it was decided to use 20 layers for both cloaks (e.g. for the 5 cm and 10 cm pole, respectively) due to it yielding fine enough approximations of Equation (3.6) while it still yielded models that were possible to mesh and simulate in Ansys HFSS in the incident plane wave environment.

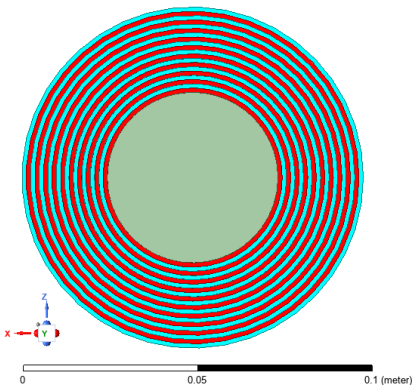

Figure 3.25: Setup of the 20 theoretical meta-material cylindrical layers with a total radius thickness of $b - a$ (in alternating red and blue) around the pole obstruction (in green, which is extended along the y-axis) of radius a in the simulation environment described in Section 3.2.

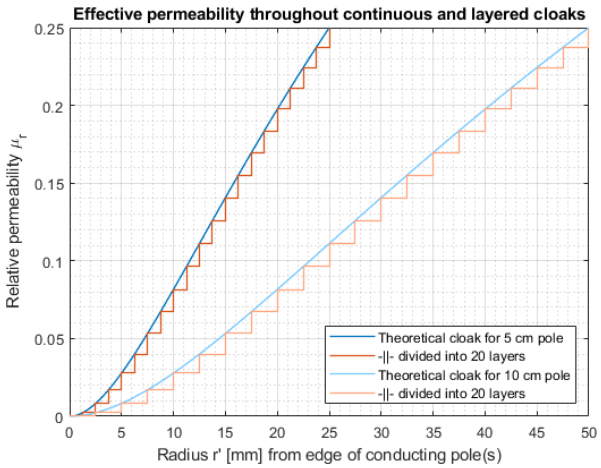

Figure 3.26: Permeability throughout continuous and layered cloaks for pole thicknesses 5 cm and 10 cm, respectively, calculated using Equation (3.6) for μ_r where $r = r' + a$.

Figure 3.27 shows the resulting electric fields as a vertically and a horizontally polarized incident wave, respectively, was propagated toward the design of shell 5 around the pole obstructions of diameters 5 cm and 10 cm. As can be seen by studying the resulting electric fields for the vertical polarization in Figure 3.27a-b), the electric field was very strong inside the cloak and local maximums were achieved in front of and behind the cloak. As the material permeability was entered as a constant value for each layer such that the required tensor gradients described in Equation (3.6) were not achieved properly (e.g. such that μ_θ was not achieved), and such that the required radial gradient μ_r was only approximately achieved, the cloak was not expected to function perfectly throughout the theoretical shell 5. However, the achieved results suggested that a simplified (e.g. less complicated to manufacture in practice as its electromagnetic properties only vary in one direction) meta-material cloak such as shell 5 could be implemented to cloak a cylinder obstruction along the same axis as the electric field is polarized. Further, as shell 5 was designed for cloaking of vertically polarized waves, its similar cloaking performance for horizontal polarization was unexpected. As can be seen in Figure 3.27c-d), the shell 5 seemed to effectively cloak the obstructions for horizontal polarization as well, however with local minimums or destructive interference in front of and behind the cloak.

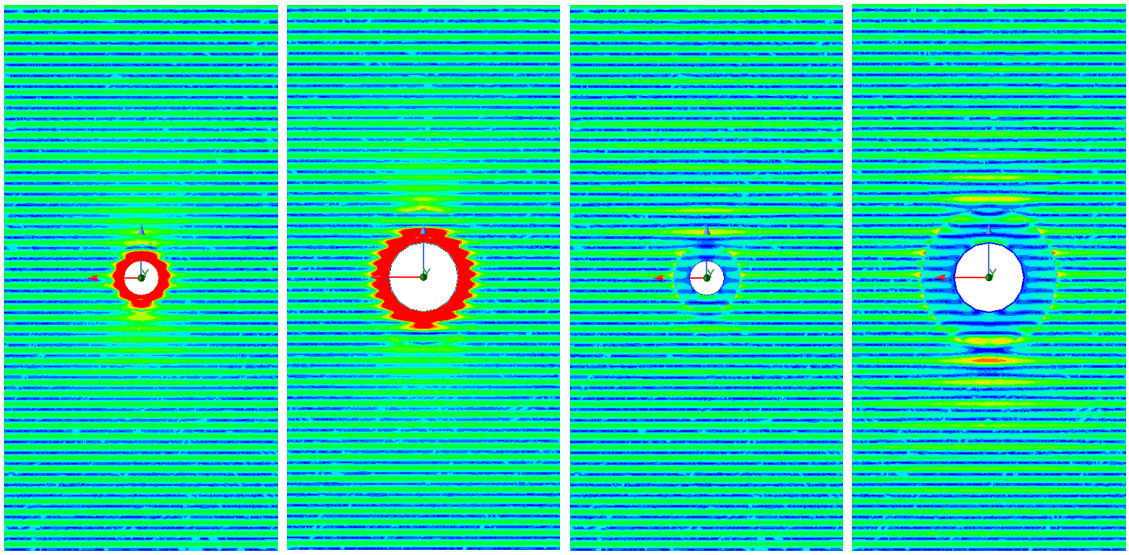

a) 5 cm pole + shell 5. b) 10 cm pole + shell 5. c) 5 cm pole + shell 5. d) 10 cm pole + shell 5.

Figure 3.27: Real electric field magnitude ($\Re(E)$) as an incident wave with vertical or horizontal polarization hits 5 cm and 10 cm diameter poles, without and with the corresponding design of the approximated theoretical layered meta-material cloak (shell 5). Figures a-b) and figures c-d) show the results for vertically and horizontally polarized incident waves, respectively. The electric field magnitude color scale is shown in Figure 3.7.

3.3.5.1 Split ring resonator cloak (practical implementation)

It is possible to approximately obtain the required electromagnetic material properties with the use of split ring resonators (SRR). Many previous works have reported functioning meta-material SRR cloaks for illumination of vertically polarized waves at radar frequencies, implementing rings with tunable patches [1][4]. With the correct tuning of the dimensions of the split rings they can act as meta-materials with, for instance, the relative permeability $\mu_r < 1$ for a certain frequency. A method for extracting the values of the relative permittivity ϵ_r, the relative permeability μ_r, the impedance z and the refractive index n of a tuned patch (or a slab of an arbitrary material) using Ansys HFSS and MATLAB is described in Appendix C. The drawbacks of the SRR cloak is the difficulty in tuning the patches correctly and the very narrowband results. Although multiple previous works have reported success when designing the SRR cloaks for vertical illumination, no cloaking characteristics were achieved when emulating the literature using SRR cloaks.

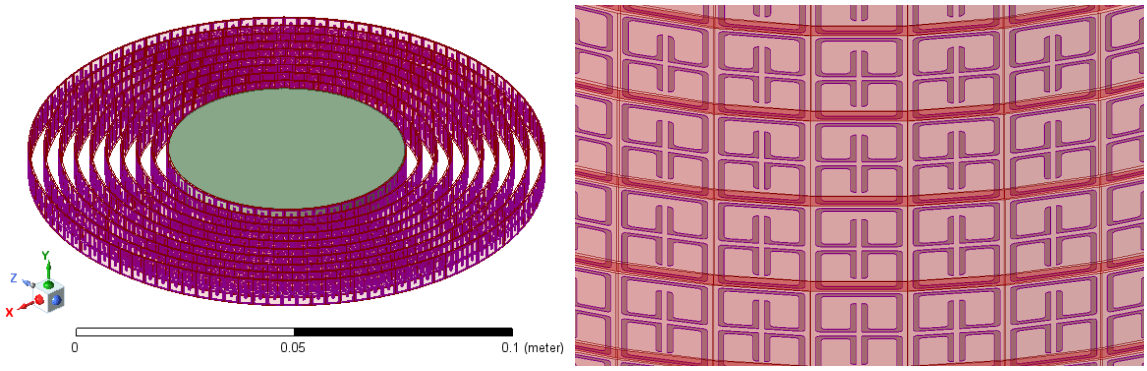

a) Zoom out.

b) Zoom in.

Figure 3.28: Visualization of a split ring resonator (SRR) coordinate transformation cloak, emulated in Ansys HFSS from previous works [1][4].

3.4 Post-processing of Ansys HFSS results in MATLAB

In order to exemplify the attained results after post-processing of the Ansys HFSS simulation data, Section 3.4.1 describes what type of data was exported and how the export was performed in order to maintain accurate embedded radiation pattern solutions after export and in order to simplify the process. Further, Section 3.4.2 describes how beamforming was applied on the exported embedded array antenna radiation pattern simulation data in MATLAB, after which Section 3.4.3 describes how the results were produced in MATLAB in order to gain knowledge about the designed array antenna's performance for different applied amplitude tapers in terms of realized gain and average sidelobe levels for different steering angles $\varnothing$ in the H-plane/azimuth plane for the elevation angle slice $\phi = 0°$.

3.4.1 Exporting data from Ansys HFSS to MATLAB

For post-processing of the Ansys HFSS simulation results, each antenna element's far field pattern, e.g. embedded antenna simulation data, was exported in *.ffd format into the MATLAB environment, after which they were converted into a MATLAB compatible format using the MATLAB functions '*import_hfss_element_patterns()*' and '*readHFSSff()*' shown in Appendix A. The far field element patterns were exported for each antenna element separately/manually using the button 'Export Fields' in the Ansys HFSS tab 'Compute Antenna Parameters' for the infinite radiation sphere. This (quite time consuming) way of exporting the data was performed because Ansys HFSS did not allow for them to be automatically exported in an embedded format (e.g. the export results were incorrect as the 'Export Element Pattern' button was used). To specify, the embedded element data was exported through exporting the fields for all elements separately by, iteratively, setting the effect of 1 W for one element and the effect of the others to 0 W in the edit sources tab for the created excitations. Further, as 21 embedded element fields needed to be exported for each solution, the export process from HFSS was made automatic

through the use of Ansys HFSS's script recording tool together with Visual Basic. More specifically, Visual Basic code was written explicitly for each export, such that the results were denoted and saved by their correct design variations and element numbers.

3.4.2 Beamforming in MATLAB

Having exported the embedded HFSS data to the MATLAB folder with the function '*import_hfss_element_patterns()*' (which in turn uses '*readHFSSff()*'), the written MATLAB function '*E2RelGain()*' shown in Appendix A.6 could be applied to obtain and plot the realized gain radiation pattern of the HFSS simulation in MATLAB. The MATLAB function '*E2RelGain()*' was written such that a modified array vector could be input in order to apply beamforming (e.g. lobe steering and/or amplitude modification) following the detailed theory in Section 2.1.4.3. It properly scales the data such that the correct simulated realized gain is obtained, and it allows for the data to easily be plotted both in 2D and 3D, if desired. Additionally, the written function makes sure that the realized gain is properly normalized over the array antenna as beamforming is applied. In order to simulate the antenna with a desired array vector in HFSS, the amplitude simply had to be squared (such that it corresponded to effect [W]) and input into the edit sources tab for the excitations. For more information regarding how the array antenna beamforming was applied, please refer to the mathematical descriptions in Section 2.1.4.3 and the thoroughly commented MATLAB code in Appendix A.6.

3.4.3 Produced results in MATLAB

For evaluation of the array antenna's performance for different amplitude tapers in terms of realized gain and average sidelobe level for different steering angles $\varnothing$ in the H-plane/azimuth plane for elevation angle slice $\phi = 0°$, the realized gain in the desired steering direction $\varnothing$ and the average sidelobe level of the realized gain radiation pattern were for uniform and Taylor tapers calculated for steering angles in the range $\varnothing = -45°$ to $45°$. This was accomplished in MATLAB by applying beamforming as described in Section 3.4.2 such that the different amplitude tapered realized gain radiation patterns were steered through all the desired steering angles $\varnothing$, for which the desired calculations were performed. That is, for all steering angles $\varnothing$ the antenna taper's realized gain in the steering angle direction was calculated, as well as the realized gain radiation pattern's average sidelobe level. As described in Sections 1.4 and 3.2, the average sidelobe level for a steering angle was calculated for the forward direction of the antenna, e.g. for the azimuth angles $-90° \leq \theta \leq 90°$, unless otherwise stated. Appendix A.4 shows the written MATLAB function '*sa_RG_ASLL()*' which returns the complex realized gain and the calculated average sidelobe level in dB for an input steering angle for uniform and Taylor tapers, and Appendix A.5 shows the written MATLAB function '*sas_MaxRG_ASLL()*' which for an input range of steering angles returns the realized gains in dB in the desired steering angle directions as well as the calculated average sidelobe levels for uniform and Taylor tapers. In order to calculate the average sidelobe level of a radiation pattern, the

written MATLAB function '*RelGain2AvgSLL()*' shown in Appendix A.7 was/is implemented, which calculates the average sidelobe level as defined in Figure 2.2 in Section 2.1.2. Further, Appendix A.8 shows the written MATLAB function '*phase2A()*' which applies a linear phase shift over an input amplitude antenna array vector (for lobe steering) and Appendix A.9 shows the MATLAB function '*taylortap_lin()*' which was implemented for obtaining a suitable Taylor taper for the array antenna. The written MATLAB script '*main.m*' which implements all of the described functions is shown in Appendix A.1. Additionally, a written general MATLAB function '*plt_gendata_ref_genpoles_genshells()*' implemented to more simply present/plot the many calculated result variations is shown in Appendix A.10.

4
Results

In this chapter, the performances of the individual designed shells are evaluated compared to the uncloaked case in terms of realized gain in the desired steering angle in the H-plane and average sidelobe level in the forward direction (e.g. for the azimuth angles $-90° \leq \theta \leq 90°$) in Section 4.1. Further, Section 4.2 compares the performances of the shells with each other, the uncloaked case and the unobstructed case. For a more detailed view of the shell's performances, please refer to Section 4.1 of the individual analyses. Instead, for the more general view of the shells' suitability for the specific described problem scenarios, please refer to Section 4.2 summarizing the most interesting results of the project.

4.1 Individual shell performances in terms of realized gain and average sidelobe level in H-plane

In this section, the designed shells are evaluated in terms of realized gain and average sidelobe level for steering angles in the H-plane. In each shell's section, two figures are presented showing the realized gain and the average sidelobe level, respectively, for the two different antenna tapers as the shell cloaks the 5 cm and the 10 cm diameter poles, respectively, located at the distances 1 m, 2 m, 3 m, 4 m, 5 m, 10 m, 20 m and 30 m. As described in Section 3.4.1, the average sidelobe levels were calculated for exported antenna diagrams for the forward direction of the antenna, i.e. for the azimuth angles $-90° \leq \theta \leq 90°$, unless otherwise stated. For simple comparisons, all figures in this section show the results for the 5 cm and 10 cm poles in the left and right columns, respectively, and the performances for the uniform and Taylor tapers in the top and bottom rows, respectively. Additionally, for easier comparisons, please note that the y-axis of every figure is fixed, such that each figure's results can be directly compared by studying the ranges the curves expand over in the x- and y-dimensions. For visualization of the resulting realized gain radiation pattern as the antenna is steered in the H-plane, Figure 4.1 exemplifies the steering of the beam as the antenna is obstructed by 5 cm and 10 cm diameter poles, respectively, from a distance of 3 m, compared to the realized gain radiation pattern of the unsteered and unobstructed antenna (in black). As can be seen by the radiation patterns from the obstructed antenna in the left column of Figure 4.1, the realized gains in the main beam (e.g. around the desired steering angle) were reduced and the average sidelobe levels were increased due to the obstruction being

in its vicinity. Further, as can be seen by studying the rows in Figure 4.1, the excited radiations' average sidelobe levels were significantly reduced as Taylor tapering was applied to the array antenna.

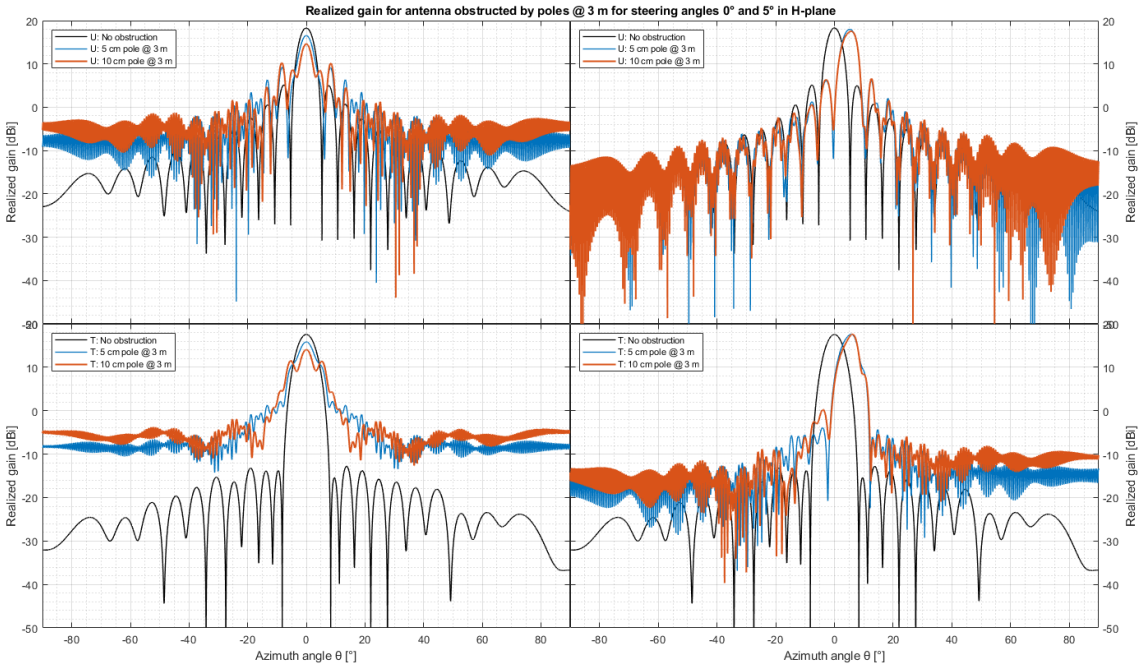

Figure 4.1: Visualization of the realized gain radiation pattern as beamforming was applied on the array antenna obstructed by 5 cm and 10 cm diameter poles. The plots exemplify the realized gain radiation pattern steered to the angles 0° and 5° in the H-plane (in the figure's left and right column, respectively) and obstructed by 5 cm and 10 cm poles at 3 m from the antenna with uniform and Taylor taper (in the figure's top and bottom row, respectively). Additionally, the realized gain of the unsteered and unobstructed antenna is shown in black as a benchmark/reference.

Another interesting thing that can be seen by studying the realized gain in the H-plane is the resulting oscillating sidelobes that occur as the antenna is obstructed. The oscillations are the result of the electromagnetic waves hitting the obstruction and being scattered on its surface such that the waves travel a longer distance and are shifted in phase. Hence, as the realized gain radiation pattern was measured in far field in Ansys HFSS, the resulting pattern had more or less oscillation depending on the scattering characteristics of the obstruction. For instance, as shown in Figure 4.1, the resulting radiation pattern in far field had a lot of oscillations in it as the antenna was obstructed by a PEC pole because of much scattering at its surface due to short circuits along it. Instead, had the pole obstructions been covered in absorbent material the oscillations would be significantly reduced (due to less scattering at the obstruction).

4.1.1 Shell 1: Thin narrowband radiation absorbent FGM-125 by Eccosorb™

In this section, the narrowband absorbent FGM-125 (shell 1) is evaluated in terms of realized gain and average sidelobe level for steering angles in the H-plane. Figures 4.2 and 4.3 show the realized gain and the average sidelobe level in the forward direction, respectively, for the two different antenna tapers as shell 1 was placed around the 5 cm and 10 cm diameter poles, respectively, at the distances 1–30 m (compared to the corresponding results with only the poles in dashed lines of the same colors as benchmarks). In Figure 4.2 it can clearly be seen that the realized gain was reduced more compared to the benchmark (of only the pole) as the absorbent FGM-125 was placed around the 5 cm diameter pole than the 10 cm diameter pole. Through comparing the results to the benchmarks (of only the poles, in dashed lines of corresponding colors) it can be seen that as shell 1 was placed around the 5 cm diameter pole the realized gain was significantly reduced for all pole distances, but it reduced the realized gain less as it was placed around the thicker pole. The larger impact on the thinner pole obstruction could be expected as the absorbent thickness of 3.18 mm increased the diameter of the obstruction by 25.4 % as the shell was placed around the thinnest pole of diameter 5 cm, whereas it only increased the diameter of the thicker pole by 12.7 %. That is, shell 1 seems to have negatively affected the thinner pole in terms of realized gain more due to it both increasing the obstruction diameter and absorbing the incoming radiation. More qualitatively, for the 5 cm pole with shell 1 around it, for the distances 1–3 m the realized gain was reduced by 0.36–0.77 dB and 0.29–0.66 dB for the uniform and Taylor taper, respectively, at the steering angle $\varnothing = 0°$ in the H-plane. Instead, for the pole of diameter 10 cm, the realized gain was only reduced with about 0.1 dB for the distances 1–5 m for both tapers.

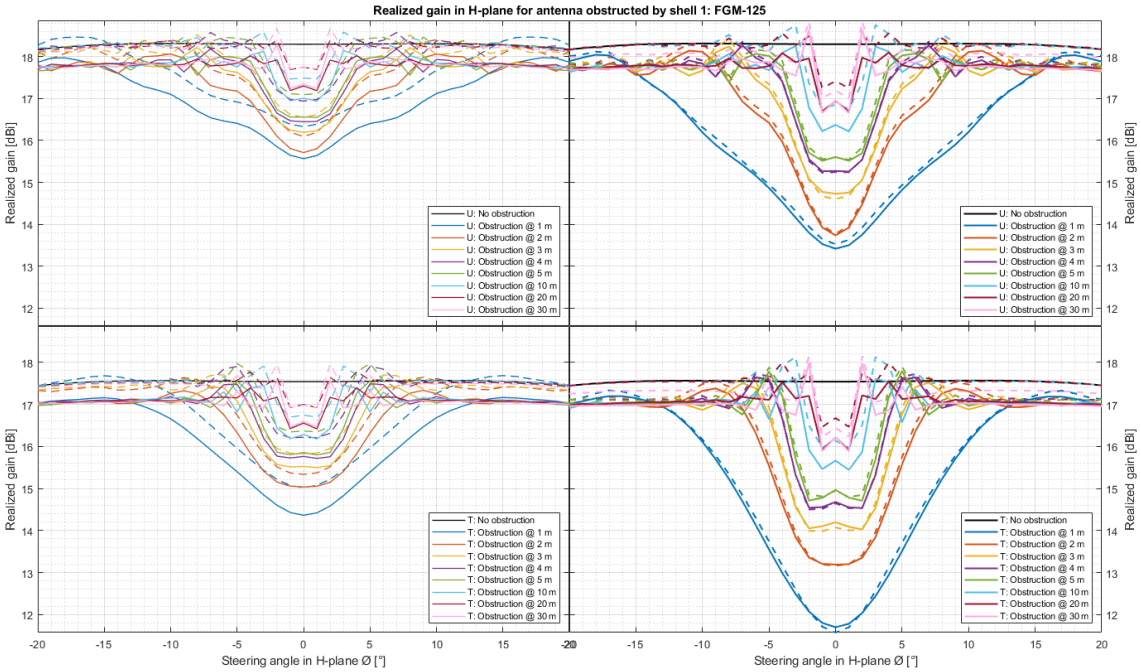

Figure 4.2: Realized gain in the H-plane as the narrowband absorbent FGM-125 (shell 1) is placed around the 5 cm and the 10 cm diameter pole (in the figure's left and right column, respectively) for uniform taper and Taylor taper (in the figure's top and bottom row, respectively). The dashed colored curves show the corresponding results for only the pole obstructions (as a benchmark/reference).

In Figure 4.3 it can clearly be seen that the average sidelobe level was lowered compared to the benchmark (of only the pole, in dashed lines of corresponding color) for all pole distances, for both pole thicknesses and for both tapers (as the resulting full lines all lied below the benchmark dashed lines as the antenna beam was around the obstruction/the area of interest). Hence, it can be understood that shell 1 can be a solution if the goal is to reduce the average sidelobe levels in the forward direction around the antenna obstruction. More qualitatively, for the 5 cm and 10 cm diameter poles with shell 1 around them, respectively, for the distances of 1–3 m the average sidelobe level was reduced by 3.76–4.12 dB and 3.89–4.04 dB for the uniform taper, and 3.82–4.47 dB and 3.98–4.04 dB for the Taylor taper at the steering angle $\varnothing = 0°$ in the H-plane. Generally, the results in Figures 4.2 and 4.3 suggest that shell 1 is appropriate for reducing the average sidelobe level in the forward direction around an obstruction to the price of some realized gain. Further, the results suggest that the FGM-125 absorbent might be best implemented around a thicker obstruction (e.g. >5 cm) as it might be too costly in terms of realized gain losses to implement the shell rather than simply let the thin pole obstruction be.

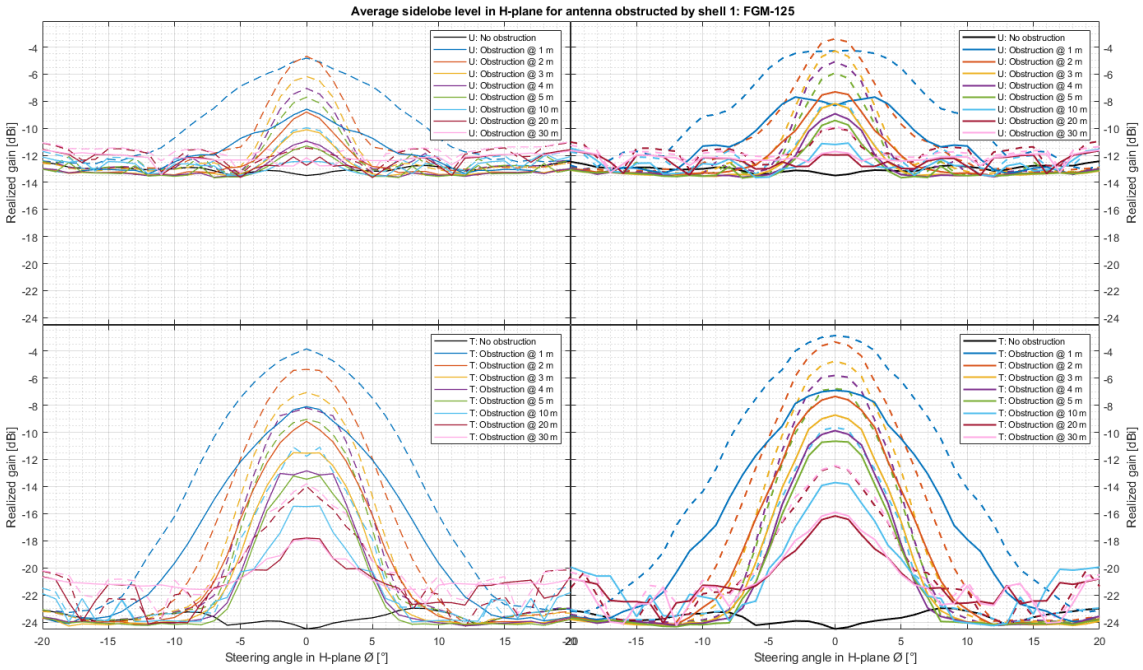

Figure 4.3: Average sidelobe level in the H-plane as the narrowband absorbent FGM-125 (shell 1) is placed around the 5 cm and the 10 cm diameter pole (in the figure's left and right column, respectively) for uniform taper and Taylor taper (in the figure's top and bottom row, respectively). The dashed colored curves show the corresponding results for only the pole obstructions (as a benchmark/reference).

4.1.2 Shell 2: Rhomb made out of PEC

In this section, the PEC rhomb (shell 2) is evaluated in terms of realized gain and average sidelobe level for steering angles in the H-plane, and the corresponding results are shown for shell 2 designed with the rhomb point angles 30.0°, 37.5° and 45.0° at 3 m from the array antenna. Figures 4.4 and 4.5 show the realized gain and the average sidelobe level in the forward direction, respectively, for the two different antenna tapers as shell 2 was placed around the 5 cm and 10 cm diameter poles, respectively, at the distances 1–30 m (compared to the corresponding results with only the poles in dashed lines of the same colors as benchmarks). As can be seen for both tapers in Figure 4.4, shell 2 effectively increased the realized gain as it was placed around the 10 cm pole obstruction close to the antenna. This can especially be seen in the right column of Figure 4.4 showing the results for the thicker pole obstructions, for which increasingly larger amounts of realized gain was retained as the obstruction was moved closer to the antenna. The larger increase of realized gain for the cloaking of the 10 cm diameter pole compared to the 5 cm diameter pole could be expected due to more of the antenna excitation being steered away from the obstruction by the rhomb point rather than being scattered at its surface. More qualitatively, for the pole of diameter 10 cm, the realized gain was increased with about 0.36–0.76 dB and 0.28–0.98 dB for the uniform and Taylor taper, respectively, for the distances 1–3 m compared to the benchmark (with only the corresponding pole) at the steering angle $\varnothing = 0°$ in the H-plane. For the pole of diameter 5 cm,

the realized gain increased and decreased for the distances 1–3 m, showing potential to retain the realized gain.

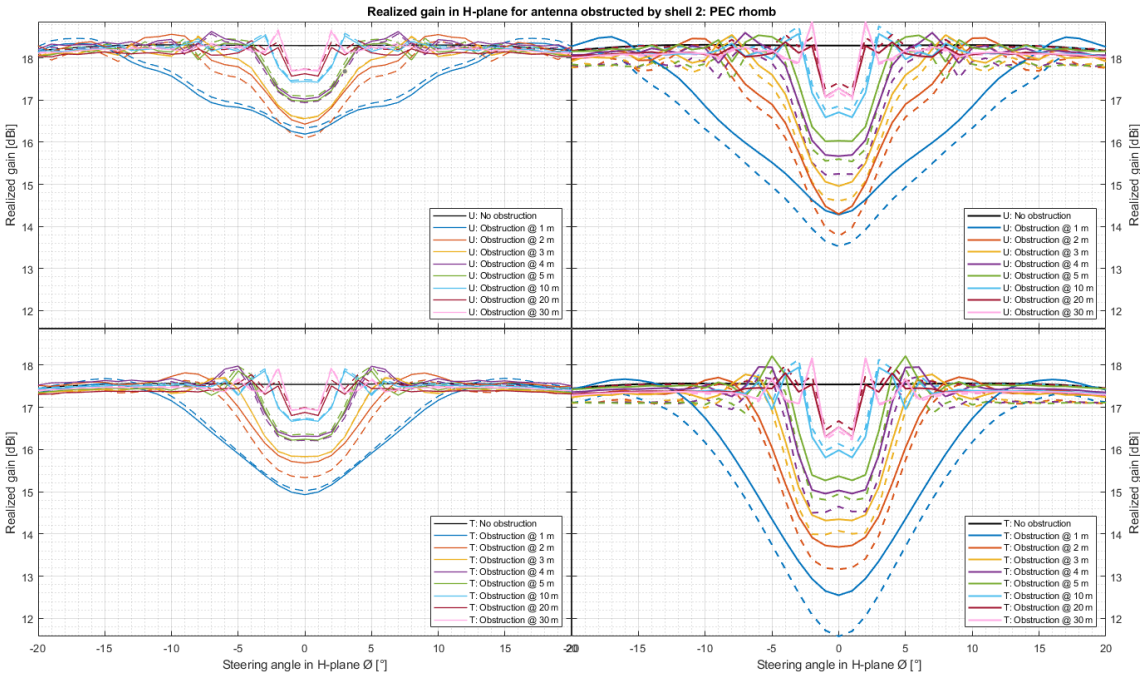

Figure 4.4: Realized gain in the H-plane as the PEC rhomb (shell 2) is placed around the 5 cm and the 10 cm diameter pole (in the figure's left and right column, respectively) for uniform taper and Taylor taper (in the figure's top and bottom row, respectively). The dashed colored curves show the corresponding results for only the pole obstructions (as a benchmark/reference).

In Figure 4.5 showing the resulting average sidelobe level for the steering angles in the H-plane in the forward direction for shell 2 it can clearly be seen that the average sidelobe level was lowered compared to the benchmark (of only the pole, in dashed lines of corresponding color) for all pole distances, for both pole thicknesses and for both tapers (as the resulting full lines all lied below the benchmark dashed lines as the antenna beam was around the obstruction/the area of interest). More qualitatively, for the 5 cm pole with shell 2 around it, at the distances of 1–3 m the average sidelobe level was decreased by 4.40–4.78 dB and 4.67–5.19 dB for the uniform and Taylor taper, respectively, compared to the benchmark (with only the corresponding pole) at the steering angle $\varnothing = 0°$ in the H-plane. Instead, for the pole of diameter 10 cm, the average sidelobe level was decreased with about 5.54–6.41 dB and 5.89–6.52 dB for the uniform and Taylor taper, respectively, for the distances 1–3 m. Generally, the results in Figures 4.4 and 4.5 suggested that shell 2 is appropriate for both increasing the realized gain and decreasing the average sidelobe level in the forward direction of the antenna, especially as the obstruction is in the close vicinity of the antenna.

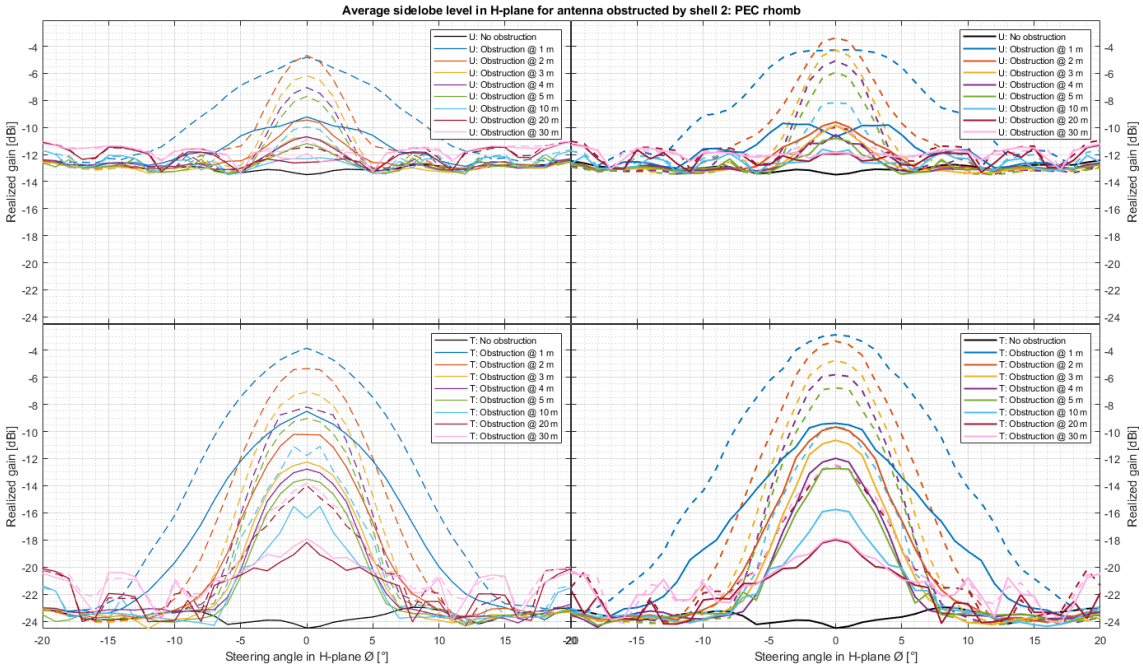

Figure 4.5: Average sidelobe level in the H-plane as the PEC rhomb (shell 2) is placed around the 5 cm and the 10 cm diameter pole (in the figure's left and right column, respectively) for uniform taper and Taylor taper (in the figure's top and bottom row, respectively). The dashed colored curves show the corresponding results for only the pole obstructions (as a benchmark/reference).

As described in Section 3.3.2, shell 2 was initially designed with the rhomb point angles 2α =30°, 37.5° or 45°, after which the designs were simulated around the 5 cm and 10 cm diameter poles at the distance of 3 m from the array antenna in the antenna and obstruction simulation. By studying Figure 4.6 showing the obtained results, it can be seen that the design of shell 2 with rhomb point angle $2\alpha = 45°$ (e.g. the chosen final design) performed best around the 5 cm diameter pole and well around the 10 cm pole at the steering angle $\varnothing = 0°$ in the H-plane. Hence, as the performance was similar between the different rhomb designs with only marginally better or worse resulting realized gain and average sidelobe level in the forward direction in the H-plane, it was concluded that any rhomb shape with a reasonable point angle would yield acceptable results. However, as described in Section 3.3.3, the rhomb point angle of $2\alpha = 45°$ was selected due to the shape being possible to mesh and simulate for shell 3 with the more complicated material design (and identical rhomb point angles for the different shells were desired for qualitative comparisons).

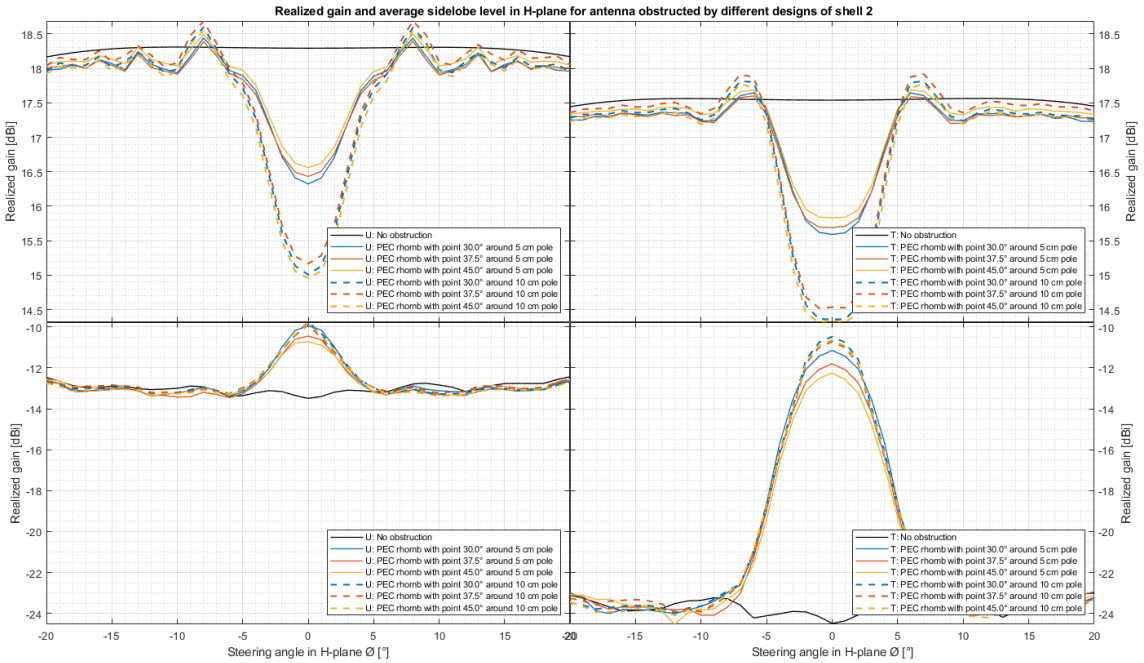

Figure 4.6: Realized gain and average sidelobe level (in the figure's top and bottom row, respectively) in the H-plane as the PEC rhomb (shell 2) designed with three different point angles was placed around the 5 cm and the 10 cm diameter pole (in the figure's left and right column, respectively) for uniform taper and Taylor taper (in the figure's left and right column, respectively) at a distance of 3 m.

4.1.3 Shell 3: Rhomb made out of a wideband radiation absorbent of increasing conductivity

In this section, the ABS rhomb (shell 3) is evaluated in terms of realized gain and average sidelobe level for steering angles in the H-plane, and the corresponding results are shown for shell 3 designed with the rhomb point angles 30.0°, 37.5° and 45.0° at 3 m from the array antenna. Figures 4.7 and 4.8 show the realized gain and the average sidelobe level in the forward direction, respectively, for the two different antenna tapers as shell 3 was placed around the 5 cm and 10 cm diameter poles, respectively, at the distances 1–30 m (compared to the corresponding results with only the poles in dashed lines of the same colors as benchmarks). As can be seen for both tapers in Figure 4.7 by comparing the resulting realized gains to the benchmarks (in dashed lines), shell 3 reduced the realized gain significantly for all pole distances as it was placed around the 5 cm diameter pole, and reduced the realized gain for the pole distances further away from the antenna as it was placed around the thicker pole. Likely, the rhomb structure still performed better than the uncloaked case as it was very close to the antenna, as the antenna excitation in the near field was steered to the sides instead of scattered backwards, like in the unobstructed case. More qualitatively, the realized gain was reduced by 0.40–0.55 dB and 0.39–0.57 dB at the steering angle $\varnothing = 0°$ in the H-plane for the uniform and Taylor taper, respectively, for the distances 1–3 m as shell 3 was placed around the

5 cm pole. Instead, the realized gain was reduced by 0.08–0.21 dB and 0.03–0.35 dB for the uniform and Taylor taper, respectively, as shell 3 was placed around the thicker pole obstruction at the distances 1–3 m compared to the uncloaked case.

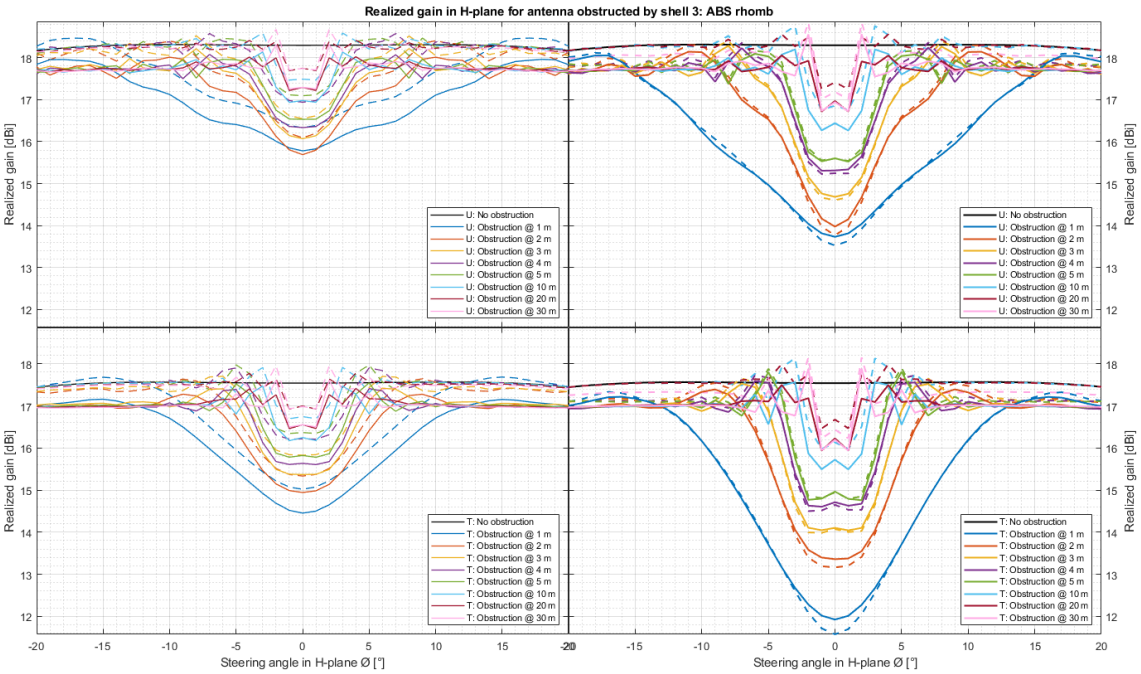

Figure 4.7: Realized gain in the H-plane as the wideband absorbent ABS rhomb (shell 3) is placed around the 5 cm and the 10 cm diameter pole (in the figure's left and right column, respectively) for uniform taper and Taylor taper (in the figure's top and bottom row, respectively). The dashed colored curves show the corresponding results for only the pole obstructions (as a benchmark/reference).

In Figure 4.8 showing the resulting average sidelobe level for the steering angles in the H-plane in the forward direction for shell 3 it can clearly be seen that the average sidelobe level was lowered compared to the benchmark (of only the pole, in dashed lines of corresponding color) for all pole distances, for both pole thicknesses and for both tapers (as the resulting full lines all lied below the benchmark dashed lines as the antenna beam was around the obstruction/the area of interest). However, as shell 3 was made of a wideband absorbent material the average sidelobe level in the forward direction decreased with an unexpectedly low amount. More qualitatively, for the 5 cm pole with shell 3 around it, at the distances of 1–3 m the average sidelobe level in the forward direction was decreased by 1.55–2.06 dB and 2.13–2.58 dB for the uniform and Taylor taper, respectively, compared to the benchmark (with only the corresponding pole) at the steering angle $\varnothing = 0°$ in the H-plane. Instead, for the pole of diameter 10 cm, the average sidelobe level was decreased with about 1.33–2.49 dB and 1.88–2.71 dB for the uniform and Taylor taper, respectively, for the distances 1–3 m. The unexpectedly low average sidelobe levels for the antenna diagram in front of the antenna were the result of the absorbent performing well in the back direction for the azimuth angles $-180° \leq \theta < -90°$ and $90° < \theta \leq 180°$ but showing weak absorbent characteristics for the azimuth angles $-90° \leq \theta \leq 90°$ corresponding to the antenna's forward direction. That this was the case can be seen

in Section 4.2 which compares the performances of all the shells and, especially, shell 2 and shell 3. Additionally, it is likely that the designed absorbent rhomb yielded less absorbent characteristics than expected due to the absorbent being structured into a triangle/rhomb tip, distinct from the rectangle that was simulated in order to evaluate the designed material's reflected effect ratio (which showed very promising results). Further, it is possible that the implemented layered absorbent design could work well if the conductivity range was increased. That is, larger values for the conductivity might have been necessary in order to increase the field attenuation throughout shell 3 due to the absorbent being made "less thick" when it was cut out into a rhomb shape, such that the absorbent material was not deep enough to attenuate the undesired antenna excitation sidelobes for the chosen conductivity range.

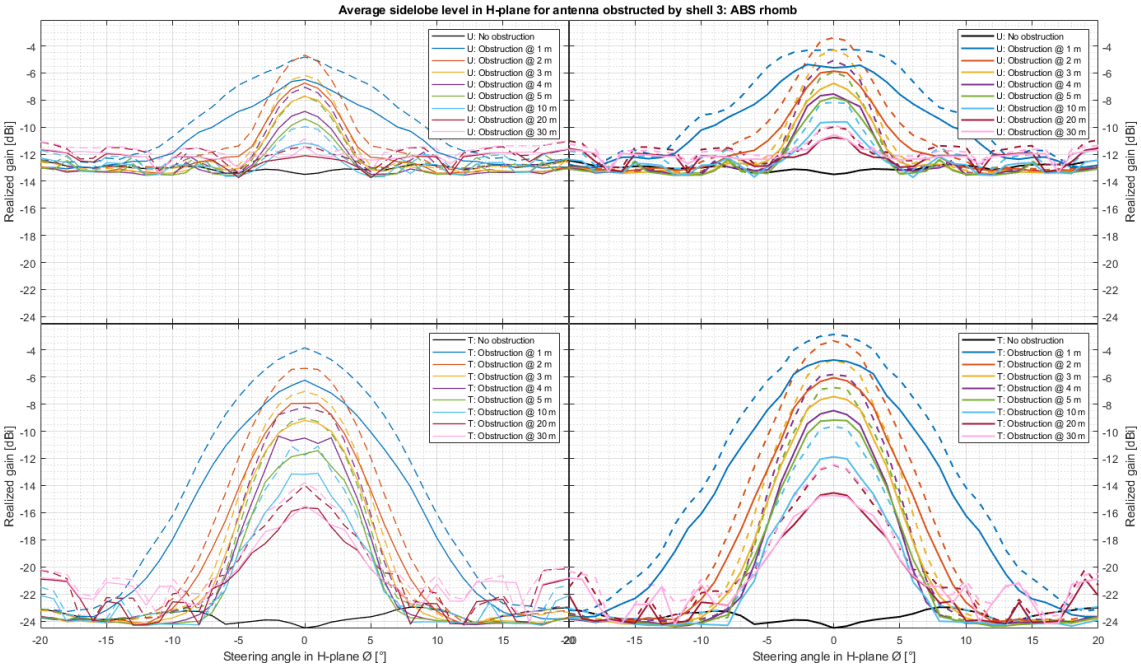

Figure 4.8: Average sidelobe level in the H-plane as the wideband absorbent ABS rhomb (shell 3) is placed around the 5 cm and the 10 cm diameter pole (in the figure's left and right column, respectively) for uniform taper and Taylor taper (in the figure's top and bottom row, respectively). The dashed colored curves show the corresponding results for only the pole obstructions (as a benchmark/reference).

Figure 4.9 shows the results of shell 3 designed with the rhomb point angles 2α =30°, 37.5° or 45° simulated around the 5 cm and 10 cm diameter poles at the distance of 3 m from the array antenna in the antenna and obstruction simulation. Similar to the corresponding results for shell 2 shown in Figure 4.6 in Section 4.1.2, the results for the different rhomb designs varied. However, though the design with the rhomb point angle $2\alpha = 45°$ did not yield the best results of the three variations of shell 3 in terms of average sidelobe level in the forward direction for both pole diameters (though only marginal differences) and though it did not perform especially better than the other designs in terms of realized gain, the design with $2\alpha = 45°$ was simulated further due to it being the only design that was possible to mesh and

simulate in Ansys HFSS. For the ABS rhombs with point angles $2\alpha = 30°$ and 37.5°, only a mesh convergence of 0.05 (instead of 0.005) was achieved due to the designs requiring too much RAM memory to simulate in Ansys HFSS.

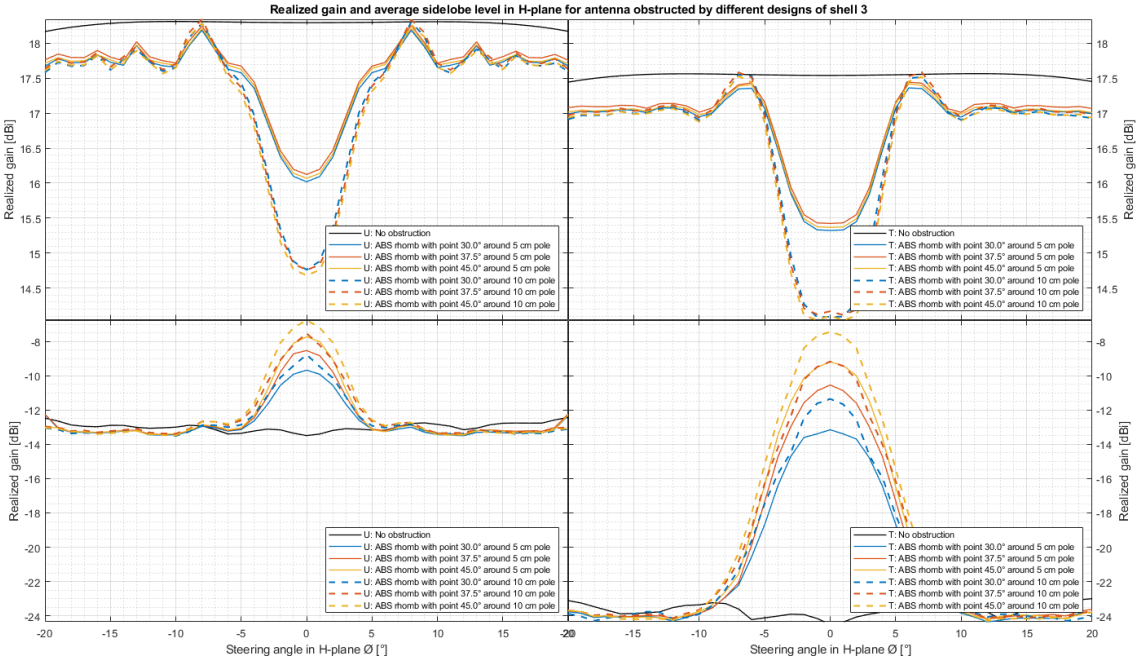

Figure 4.9: Realized gain and average sidelobe level (in the figure's top and bottom row, respectively) in the H-plane as the ABS rhomb (shell 3) designed with three different point angles was placed around the 5 cm and the 10 cm diameter pole (in the figure's left and right column, respectively) for uniform taper and Taylor taper (in the figure's left and right column, respectively) at a distance of 3 m. For the ABS rhombs with point angles 30° and 37.5°, only the mesh convergences 0.05 (instead of 0.005) were achieved due to the designs requiring too much RAM memory to simulate in Ansys HFSS.

4.1.4 Shell 4: Rhomb made out of PEC with added dielectric border and PEC strips

In this section, the DiStrip rhomb (shell 4) is evaluated in terms of realized gain and average sidelobe level for steering angles in the H-plane. Figures 4.10 and 4.11 show the realized gain and the average sidelobe level in the forward direction, respectively, for the two different antenna tapers as shell 4 was placed around the 5 cm and 10 cm diameter poles, respectively, at the distances 1–30 m (compared to the corresponding results with only the poles in dashed lines of the same colors as benchmarks). As can be seen for both tapers in Figure 4.10 by comparing the resulting realized gains to the benchmarks (in dashed lines), shell 4 very effectively increased the realized gain in far field. More interestingly, which can be seen for multiple pole distances in Figure 4.10 by the resulting realized gain curves lying over the corresponding benchmark results of the uncloaked cases, shell 4 succeeded in steering the electromagnetic waves around the circumference of the structure, as studied for the incident plane wave simulations with shell 4 in Section 3.3.4. More

thoroughly, it can be seen in Figure 4.10 that shell 4 most effectively guided the electromagnetic waves around itself for the short steering angle range of ±2.5° (and upwards, depending on the pole distance and pole diameter), where the results were close to the unobstructed case when the pole obstructions were further away from the antenna. More qualitatively, the realized gain was increased by 0.11–0.88 dB and 0.78–1.13 dB at the steering angle $\varnothing = 0°$ in the H-plane for the uniform and Taylor taper, respectively, for the distances 1–3 m as shell 4 was placed around the 5 cm pole. Instead, the realized gain was increased by 1.36–1.92 dB and 1.92–2.75 dB for the uniform and Taylor taper, respectively, as shell 4 was placed around the thicker pole obstruction at the distances 1–3 m compared to the uncloaked case.

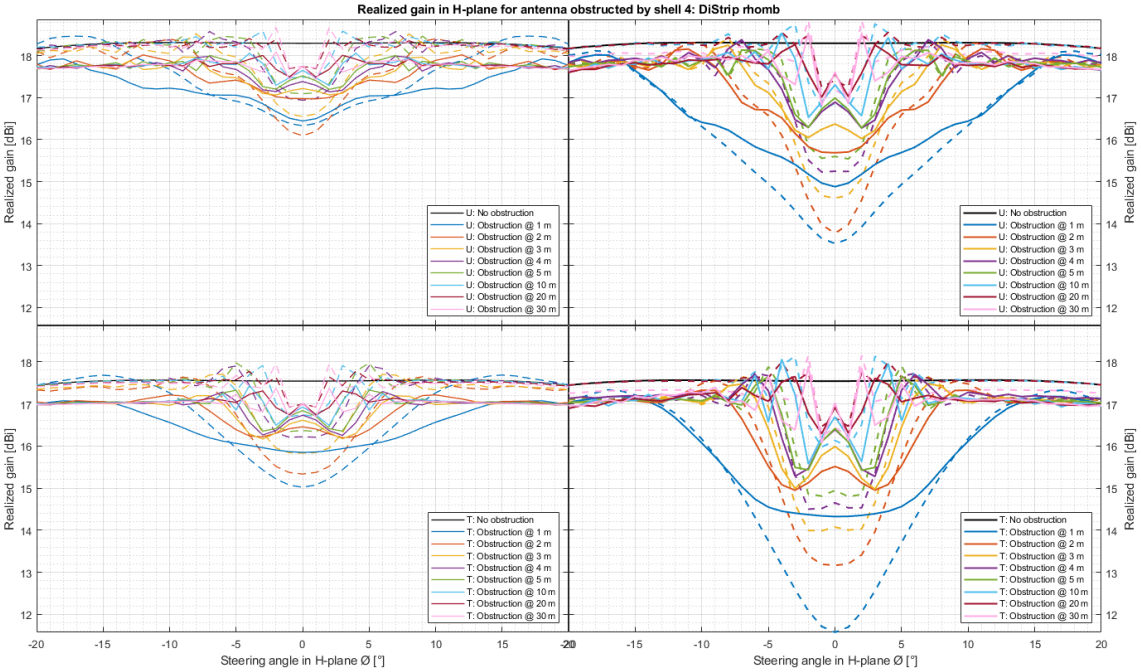

Figure 4.10: Realized gain in the H-plane as the DiStrip rhomb (shell 4) is placed around the 5 cm and the 10 cm diameter pole (in the figure's left and right column, respectively) for uniform taper and Taylor taper (in the figure's top and bottom row, respectively). The dashed colored curves show the corresponding results for only the pole obstructions (as a benchmark/reference).

As can clearly be seen by studying Figure 4.8 showing the resulting average sidelobe level for the steering angles in the H-plane in the forward direction for shell 4, the average sidelobe level was increased or only slightly decreased compared to the benchmark for all pole distances, for both pole thicknesses and for both tapers. More qualitatively, for the 5 cm pole with shell 4 around it, at the distances of 1–3 m the average sidelobe level in the forward direction was increased by 0.03–0.47 dB and decreased by 0.00–0.43 dB for the uniform and Taylor taper, respectively, compared to the benchmark (with only the corresponding pole) at the steering angle $\varnothing = 0°$ in the H-plane. Instead, for the pole of diameter 10 cm, the average sidelobe level was increased with about 0.62–2.07 dB and 0.09–0.79 dB for the uniform and Taylor taper, respectively, for the distances 1–3 m. That is, generally, shell 4 effectively increased the realized gain to the price of introduced scattering, e.g. a significantly

increased or remaining average sidelobe level in the antenna's forward direction in the H-plane. Please note that, as described in Section 3.3.4, shell 4 was not designed entirely as proposed by previous successful works [5] and that the solution likely would have yielded both higher realized gain for a larger range of steering angles in the H-plane and much lower average sidelobe levels in the forward direction had the design stage not failed to change the dielectric material at the rhomb point tips to a dielectric of lower permittivity.

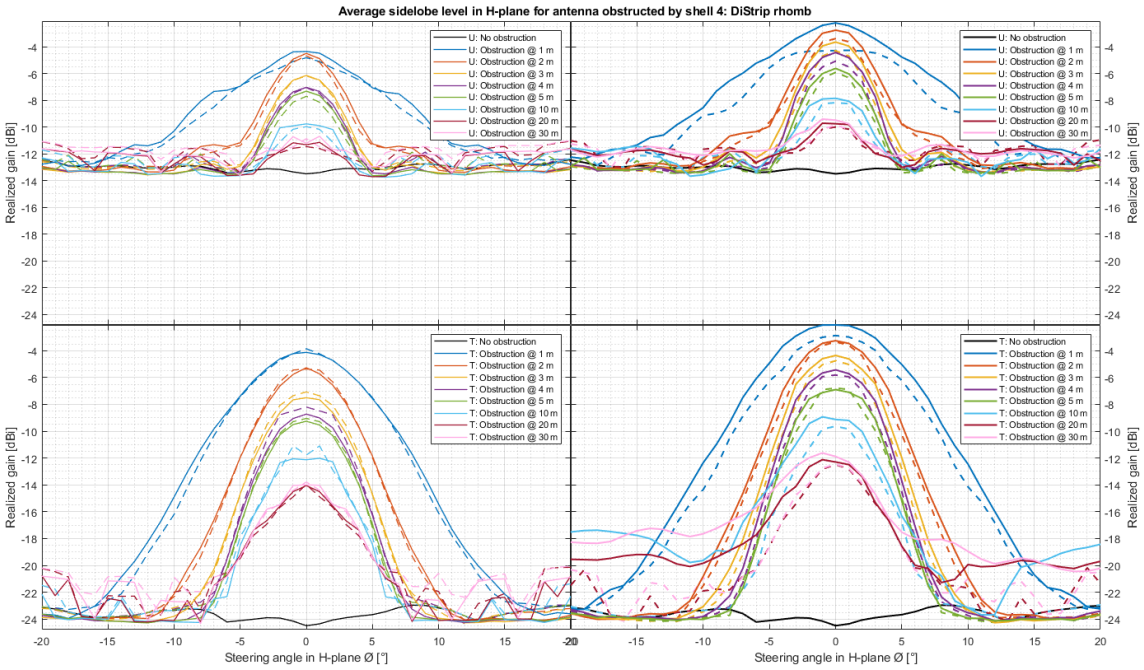

Figure 4.11: Average sidelobe level in the H-plane as the DiStrip rhomb (shell 4) is placed around the 5 cm and the 10 cm diameter pole (in the figure's left and right column, respectively) for uniform taper and Taylor taper (in the figure's top and bottom row, respectively). The dashed colored curves show the corresponding results for only the pole obstructions (as a benchmark/reference).

4.2 Comparison of shell performances in terms of realized gain and average sidelobe level in H-plane

In this section, the performances of the shells are compared in terms of realized gain and average sidelobe level in the H-plane. Through plotting the results shown in Section 4.1 as a function of the pole distances (e.g. in 3D), the decrease of realized gain and the increase of average sidelobe level relative to the unobstructed cases are shown as color gradients in the xy-plane specifying the pole distance [m] and steering angle $\varnothing$ [°]. For clear investigations of the shell performances for the four different antenna obstruction cloaking problem scenarios, this section evaluates the variations described in Table 4.1, in their given order.

Table 4.1: The four different antenna obstruction cloaking scenarios.

Scenario	Pole diameter	Antenna taper
1	5 cm	U
2	10 cm	T
3	5 cm	U
4	10 cm	T

By studying Figure 4.12 showing the shell's cloaking characteristics for scenario 1 of the 5 cm pole obstruction and uniform antenna taper, it can clearly be seen that the DiStrip rhomb (shell 4) performed best in terms of realized gain, however worst in terms of average sidelobe level, whereas the PEC rhomb (shell 2) performed best in terms of average sidelobe level and second best in terms of realized gain. Additionally, it should be noted that the DiStrip rhomb worked especially well for the rather narrow steering angle range of about $\pm 2.5°$ for pole distances of more than 3 m from the antenna. Please note that (though not demonstrated in this report), shell 4 would very likely have yielded the high realized gain improvement for a wider range of steering angles and, especially, lower average sidelobe levels in the forward direction had the cloak been properly designed, as described in Sections 3.3.4 and 4.1.4. Further, through comparing the results of the shells with the results for only the pole, it can distinctly be seen that the absorbent FGM-125 (shell 1) and the absorbent ABS rhomb (shell 3) both yielded larger decreases of realized gain than the uncloaked obstruction, and that the DiStrip rhomb (shell 4) yielded a larger increase of average sidelobe level.

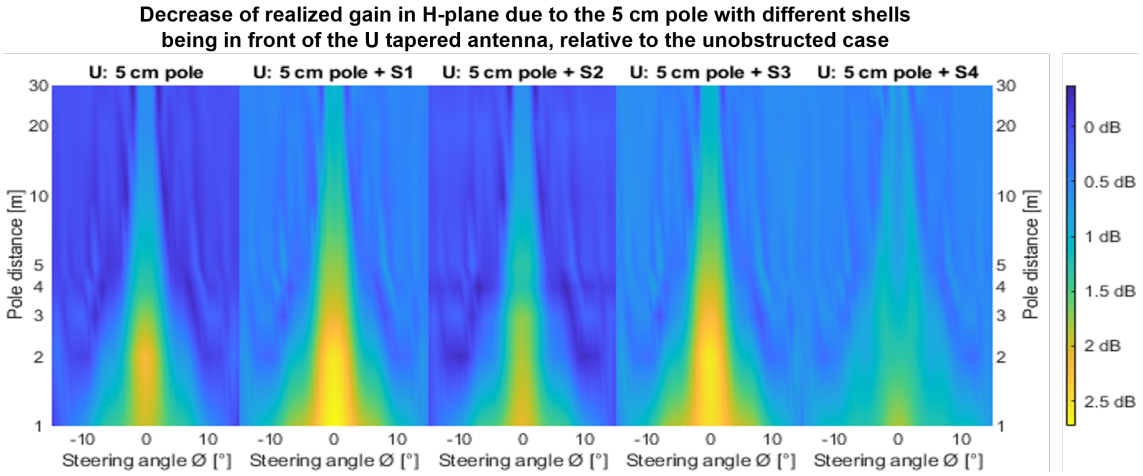

a) Relative decrease in realized gain.

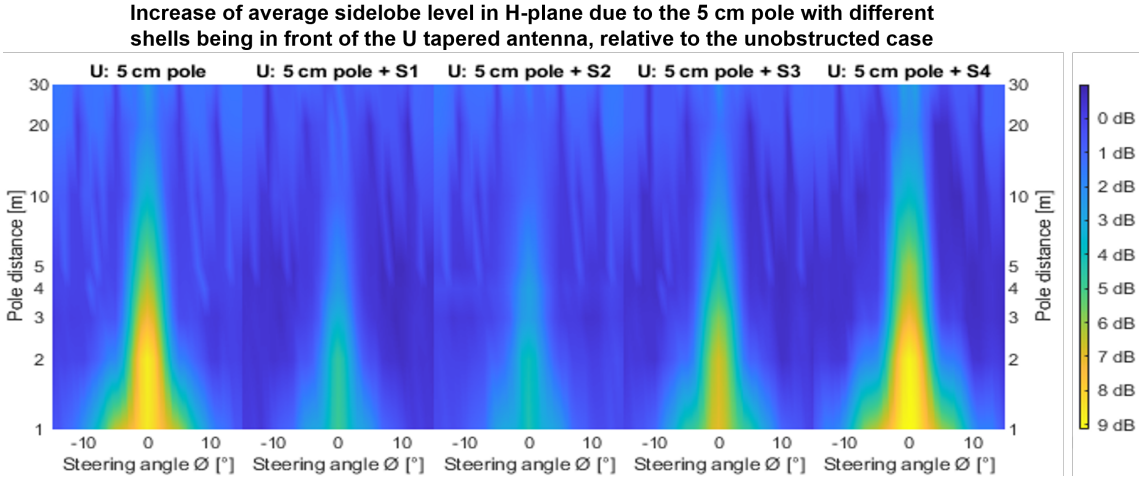

b) Relative increase in average sidelobe level.

Figure 4.12: Decrease in realized gain and increase in average sidelobe level as a result of the 5 cm pole with different shells in front of the antenna with uniform taper, relative to the unobstructed case (e.g. such that 0 dB corresponds to the ideal case/no obstruction). The colorbar specifies the figure's realized gain range and the y-axis specifies the pole distance in a logarithmic scale.

As described in Section 4.1.3, the unexpected unabsorbent characteristics suggested by the results for the ABS rhomb were due to the average sidelobe level being calculated for only the forward direction of the antenna. Instead, by exporting plotting the antenna diagram in the full range of the H-plane it can be seen that the ABS rhomb yielded lower sidelobes than the PEC rhomb in the back direction. This can be seen in Figure 4.13 exemplifying the absorbent characteristics of shell 3 in the back direction and the lack of it in the forward direction, through which it can be understood why a PEC rhomb outperformed the absorbent rhomb of the same design dimensions in terms of average sidelobe levels. In order to clearly detail the calculated average sidelobe level results, Figure 4.13 shows the calculated average sidelobe levels for shell 2 and shell 3 around the 5 cm pole compared to the unobstructed case, calculated for the full range in the H-plane and only for the

forward range (shown in dashed and dotted lines, respectively). By studying the calculated average sidelobe levels, it can be seen that the average sidelobe level was higher for shell 3 for only the forward direction compared to the full angle range in the H-plane due to it not showing absorbent characteristics within the azimuth angle range $-90° \leq \theta \leq 90°$ but outside it, whereas the result for shell 2 happened to remain somewhat unchanged.

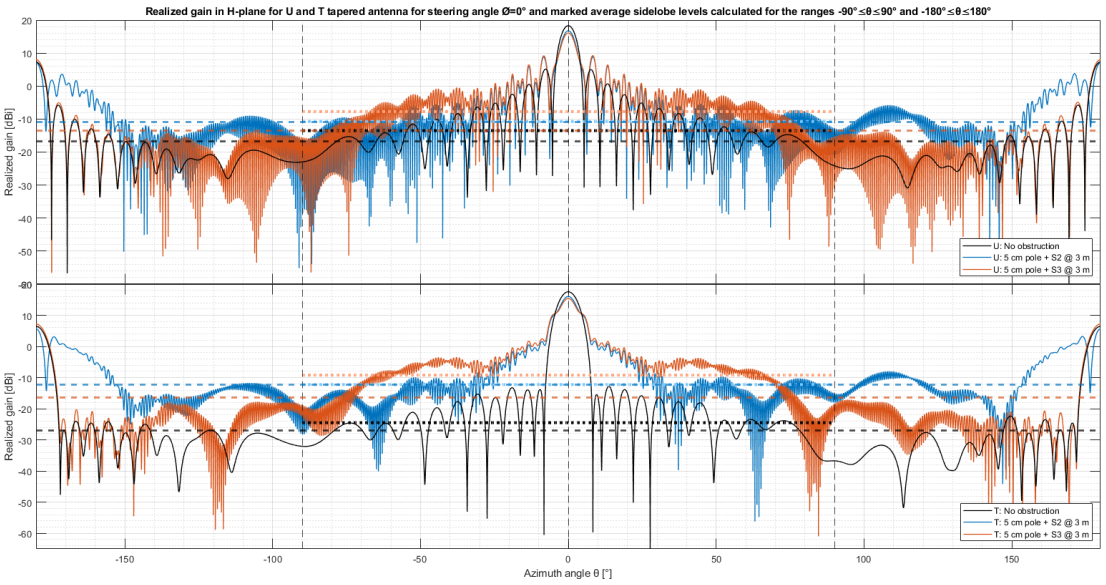

Figure 4.13: Comparison of the resulting antenna diagram as shell 2 and shell 3 were placed around the 5 cm pole at the distance of 3 m. The dashed and dotted lines mark the average sidelobe level of the full azimuth angle range $-180° \leq \theta \leq 180°$ and the azimuth range $-90° \leq \theta \leq 90°$ for the forward direction, respectively, for the antenna diagrams of corresponding colors.

By further studying Figures 4.14, 4.15 and 4.16 showing the results for the scenarios 2, 3 and 4, respectively, it can be seen that the same general results were obtained for the 5 cm and the 10 cm diameter poles for the two tapers as described previously for scenario 1 of the 5 cm pole with uniform taper in Figure 4.12. Hence, it was concluded that shell 4 of the DiStrip rhomb performed best in terms of increasing the realized gain in the desired steering angle H-plane, but worst in terms of average sidelobe level in the forward direction of the H-plane. Instead, it was concluded that shell 2 of the PEC rhomb performed best in terms of decreasing the average sidelobe level in the forward direction of the H-plane and second best in terms of realized gain, whereas shell 3 failed to show the desired absorbent characteristics for the azimuth angles θ corresponding to the H-plane in front of the antenna.

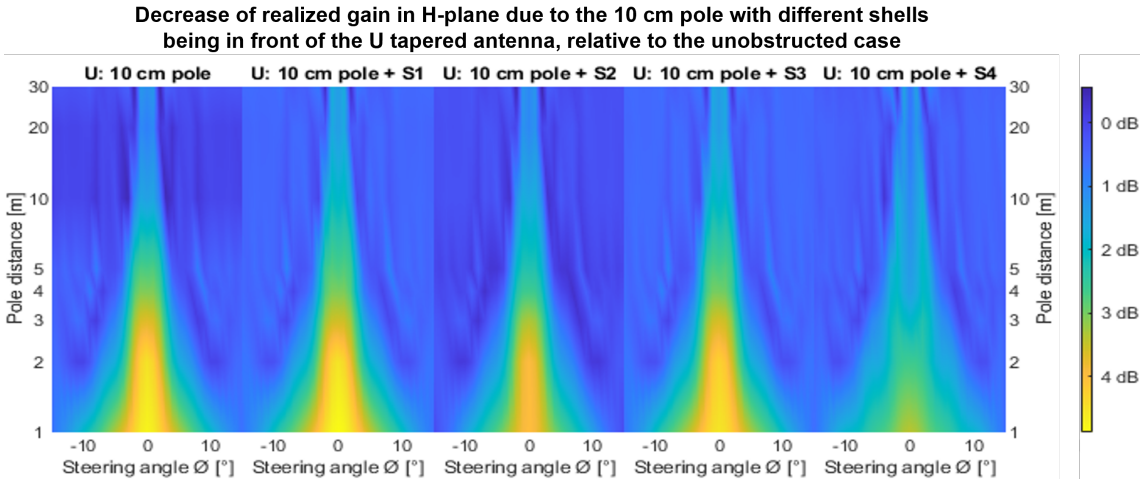

a) Relative decrease in realized gain.

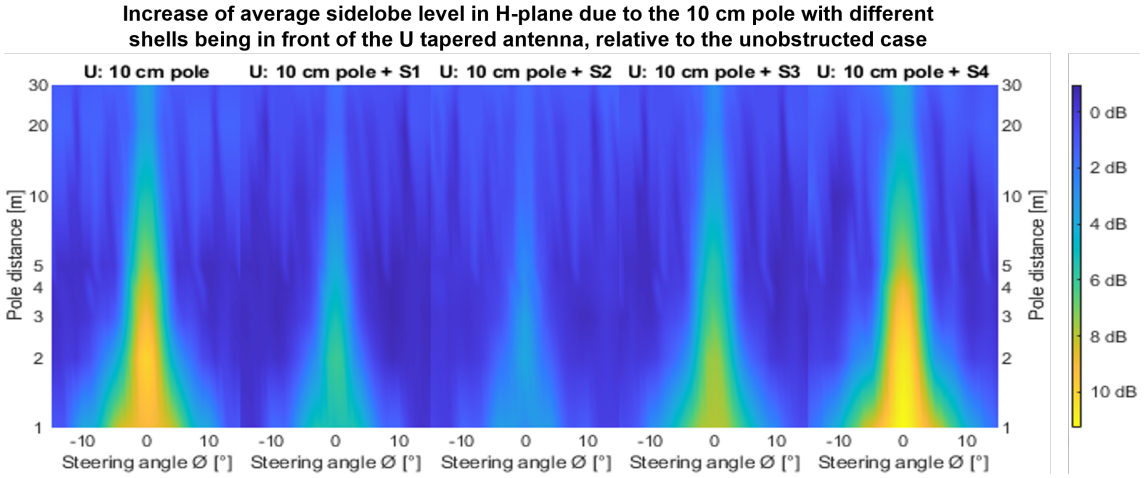

b) Relative increase in average sidelobe level.

Figure 4.14: Decrease in realized gain and increase in average sidelobe level as a result of the 10 cm pole with different shells in front of the antenna with uniform taper, relative to the unobstructed case (e.g. such that 0 dB corresponds to the ideal case/no obstruction). The colorbar specifies the figure's realized gain range and the y-axis specifies the pole distance in a logarithmic scale.

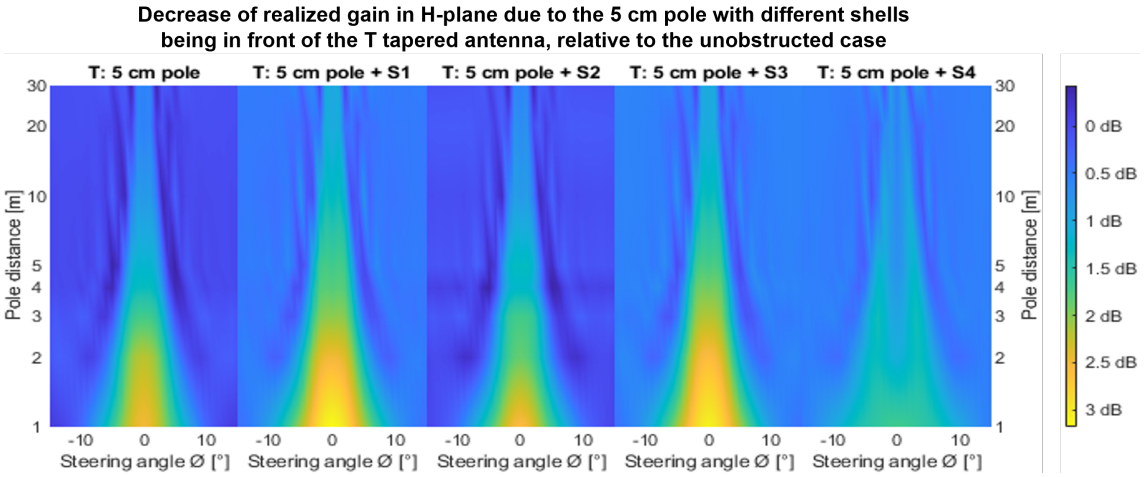

a) Relative decrease in realized gain.

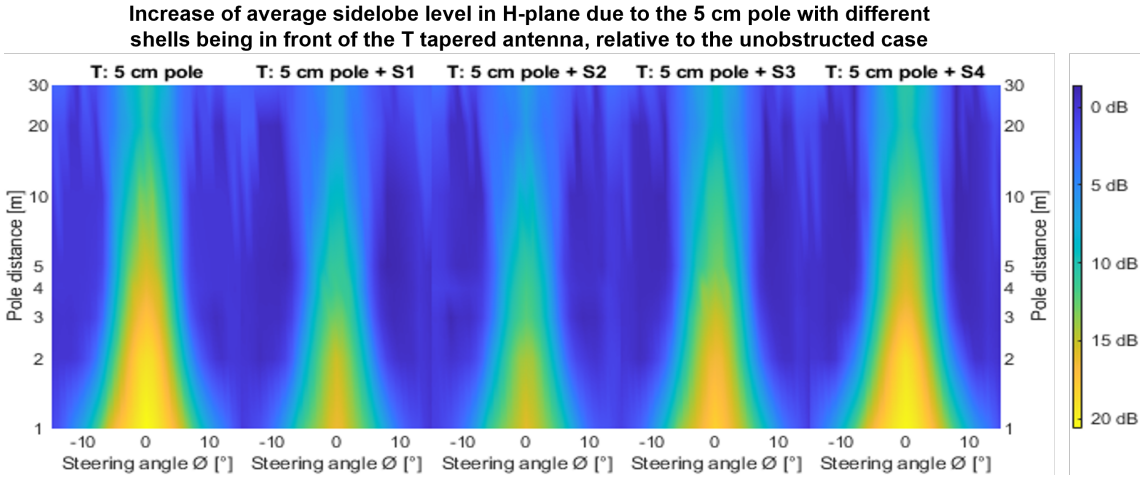

b) Relative increase in average sidelobe level.

Figure 4.15: Decrease in realized gain and increase in average sidelobe level as a result of the 5 cm pole with different shells in front of the antenna with Taylor taper, relative to the unobstructed case (e.g. such that 0 dB corresponds to the ideal case/no obstruction). The colorbar specifies the figure's realized gain range and the y-axis specifies the pole distance in a logarithmic scale.

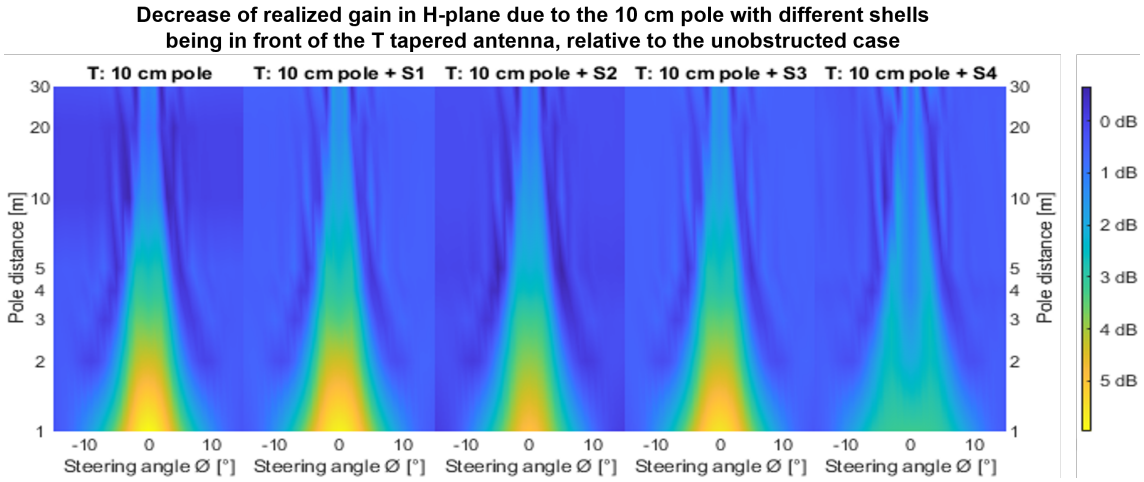

a) Relative decrease in realized gain.

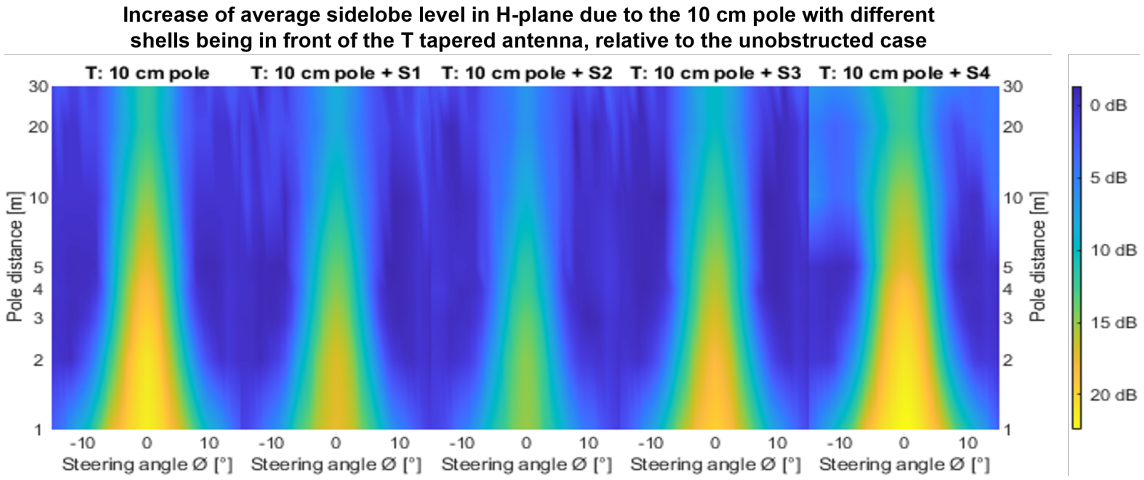

b) Relative increase in average sidelobe level.

Figure 4.16: Decrease in realized gain and increase in average sidelobe level as a result of the 10 cm pole with different shells in front of the antenna with Taylor taper, relative to the unobstructed case (e.g. such that 0 dB corresponds to the ideal case/no obstruction). The colorbar specifies the figure's realized gain range and the y-axis specifies the pole distance in a logarithmic scale.

Table 5.1: Summary of the shells' performances relative to the uncloaked case. Two arrows mark the best performing scenario for each category.

Scenario		**Shell**	**RG**	**ASLL***
1	5 cm pole U taper	S1 S2 S3 S4	↘ ↗ ↘ ↗ ↗	↘ ↘ ↘ ↘ ↗
2	10 cm pole U taper	S1 S2 S3 S4	↘ ↗ ↗ ↗ ↗	↘ ↘ ↘ ↘ ↗
3	5 cm pole T taper	S1 S2 S3 S4	↘ ↗ ↘ ↗ ↗	↘ ↘ ↘ ↘ ↗
4	10 cm pole T taper	S1 S2 S3 S4	↘ ↗ ↗ ↗ ↗	↘ ↘ ↘ ↘ ↗

*For the angles $-90° \leq \theta \leq 90°$ in the H-plane.

5
Conclusion

Four different techniques of electromagnetic cloaking and anti-scattering on a vertically aligned metallic cylindrical obstruction of diameter 5 cm or 10 cm at the distances 1–30 m from a vertically polarized 9.5 GHz/X-band antenna have been investigated in terms of realized gain (RG) and average sidelobe level (ASLL) in the H-plane/azimuth plane in front of the antenna. The four designed and evaluated shells were 1) a thin layer of a narrowband absorbent, 2) a rhomb made out of PEC, 3) a rhomb made out of a wideband absorbent material and 4) a PEC rhomb (e.g. shell 2) supplemented with a dielectric border and PEC strips along the circumference of the structure. Additionally, the report investigated the possibilities of designing a theoretically layered meta-material cloak in practice. Though obtaining cloaking characteristics using meta-materials has been a hot topic the recent years and promising results have been suggested at X-band frequencies, the thesis concluded after evaluation that there exist much easier and less time consuming solutions that yield very effective results. As summarized by Table 5.1 which compares the performances of the shells compared to the uncloaked cases, cloaking the pole obstructions with the PEC rhomb (shell 2) yielded a large decrease in average sidelobe level, on average a decrease of 4.75 dB and of 6.17 dB from the uncloaked case at the distances 1–5 m for the 5 cm and 10 cm pole, respectively, with Taylor taper, and at the same time increased the realized gain in far field. Instead, shell 4 effectively guided the electromagnetic waves around the circumference of the structure yielding an increase of realized gain, on average an increase of 0.74 dB and of 2.04 dB from the unobstructed case at the distances 1–5 m distance for a 5 cm and 10 cm pole, respectively, with Taylor taper. The conclusion drawn was that the described project problem scenario is best solved with shell 2 if the goal is to decrease the average sidelobe level *and* increase the realized gain, or with shell 4 if the aim is to increase the realized gain as much as possible. Finally, the thesis recommends to redesign shell 4 such that the point tips of the outer dielectric edge are made of a material with a relatively lower permittivity as it likely will both significantly reduce the average sidelobe level and increase the realized gain for steering angles in the H-plane such that it proves to be the best solution for the described problem scenario.

Bibliography

[1] D. Schurig, J. J. Mock, B. J. Justice, *et al.*, "Metamaterial electromagnetic cloak at microwave frequencies,"
Science, vol. 314, no. 5801, pp. 977–980, 2006.
DOI: 10.1126/science.1133628. eprint:
https://www.science.org/doi/pdf/10.1126/science.1133628. [Online].
Available: https://www.science.org/doi/abs/10.1126/science.1133628.

[2] P. Yuste, J. Rius, J. Romeu, S. Blanch, A. Heldring, and E. Ubeda, "A microwave invisibility cloak: The design, simulation, and measurement of a simple and effective frequency-selective surface-based mantle cloak.," *IEEE Antennas and Propagation Magazine, Antennas and Propagation Magazine, IEEE, IEEE Antennas Propag. Mag*, vol. 60, no. 4, pp. 49–59, 2018,
ISSN: 1045-9243. [Online]. Available:
https://search.ebscohost.com/login.aspx?direct=true&db=edseee&AN=edseee.8396862&site=eds-live&scope=site&authtype=guest&custid=s3911979&groupid=main&profile=eds.

[3] X. Chen, T. M. Grzegorczyk, B.-I. Wu, J. Pacheco, and J. A. Kong, "Robust method to retrieve the constitutive effective parameters of metamaterials,"
Phys. Rev. E, vol. 70, p. 016 608, 1 Jul. 2004.
DOI: 10.1103/PhysRevE.70.016608. [Online]. Available:
https://link.aps.org/doi/10.1103/PhysRevE.70.016608.

[4] M. Sharawi and A. Numan, "Extraction of material parameters for metamaterials using a full-wave simulator [education column],"
IEEE Antennas and Propagation Magazine, vol. 55, p. 202, Oct. 2013.
DOI: 10.1109/MAP.2013.6735515.

[5] P.-S. Kildal, A. Kishk, and A. Tengs, "Reduction of forward scattering from cylindrical objects using hard surfaces.," *IEEE Transactions on Antennas and Propagation, Antennas and Propagation, IEEE Transactions on, IEEE Trans. Antennas Propagat*, vol. 44, no. 11, pp. 1509–1520, 1996,
ISSN: 0018-926X. [Online]. Available:
https://search.ebscohost.com/login.aspx?direct=true&db=edseee&AN=edseee.542076&site=eds-live&scope=site&authtype=guest&custid=s3911979&groupid=main&profile=eds.

[6] SAAB. "Visby-class corvette: Saab." (),
[Online]. Available: https://www.saab.com/products/visby-class-corvette.

[7] NASA. "Anatomy of an electromagnetic wave - nasa science." (2022),
[Online]. Available: https://science.nasa.gov/ems/02_anatomy/.

[8] FURUNO. "Radar basics." (), [Online]. Available: https://www.furuno.com/en/technology/radar/basic/#:~:text=The%20distance%20resolution%20depends%20greatly,the%20distance%20resolution%20is%20reduced.

[9] "Ieee standard letter designations for radar-frequency bands," *IEEE Std 521-2002 (Revision of IEEE Std 521-1984)*, pp. 1–10, 2003. DOI: 10.1109/IEEESTD.2003.94224.

[10] C. A. Balanis, *Antenna theory. [electronic resource] : analysis and design.* John Wiley, 2005, ISBN: 0471714615. [Online]. Available: %5Curl%7Bhttps://search.ebscohost.com/login.aspx?direct=true&db=cat07472a&AN=clec.DAWVLE25709967&site=eds-live&scope=site&authtype=guest&custid=s3911979&groupid=main&profile=eds%7D.

[11] A. Villeneuve, "Taylor patterns for discrete arrays," *IEEE Transactions on Antennas and Propagation*, vol. 32, no. 10, pp. 1089–1093, 1984. DOI: 10.1109/TAP.1984.1143212.

[12] P.-S. Kildal, *Foundations of Antenna Engineering : A Unified Approach for Line-of-Sight and Multipath.* Artech House, 2015, ISBN: 9781608078684. [Online]. Available: https://search.ebscohost.com/login.aspx?direct=true&db=cat07472a&AN=clec.EBC4537960&site=eds-live&scope=site&authtype=guest&custid=s3911979&groupid=main&profile=eds.

[13] B. Arik D., *Active Electronically Scanned Arrays : Fundamentals and Applications.* Wiley, 2021, ISBN: 978-1-119-74908-0. [Online]. Available: https://search.ebscohost.com/login.aspx?direct=true&db=edseee&AN=edseee.9635026&site=eds-live&scope=site&authtype=guest&custid=s3911979&groupid=main&profile=eds.

[14] D. M. Pozar, *Microwave engineering.* Wiley, 2012, ISBN: 9780470631553. [Online]. Available: https://search.ebscohost.com/login.aspx?direct=true&db=cat09075a&AN=clpc.oai.edge.chalmers.folio.ebsco.com.fs00001000.1f116dfa.0d37.49c1.918e.8c6fad4989eb&site=eds-live&scope=site&authtype=guest&custid=s3911979&groupid=main&profile=eds.

[15] S. L. Hub. "Refraction of light." (May 23, 2020), [Online]. Available: https://www.sciencelearn.org.nz/resources/49-refraction-of-light#:~:text=Refraction%20is%20the%20bending%20of,magnifying%20glasses%2C%20prisms%20and%20rainbows.

[16] B. Chambers and A. Tennant, "Active dallenbach radar absorber," in *2006 IEEE Antennas and Propagation Society International Symposium*, 2006, pp. 381–384. DOI: 10.1109/APS.2006.1710537.

[17] F.-k. Zhou, R.-y. Tan, W. Fang, *et al.*, "An ultra-broadband microwave absorber based on hybrid structure of stereo metamaterial and planar metasurface for the s, c, x and ku bands," *Results in Physics*, vol. 30, p. 104 811, 2021, ISSN: 2211-3797.

DOI: https://doi.org/10.1016/j.rinp.2021.104811. [Online]. Available: https://www.sciencedirect.com/science/article/pii/S2211379721008627.

[18] M. Liang and D. Haochuan, "Study on absorbing characteristics of salisbury screen filled with plasma," *Procedia Computer Science*, vol. 187, pp. 241–245, 2021, 2020 International Conference on Identification, Information and Knowledge in the Internet of Things, IIKI2020, ISSN: 1877-0509. DOI: https://doi.org/10.1016/j.procs.2021.04.057. [Online]. Available: https://www.sciencedirect.com/science/article/pii/S1877050921008504.

[19] P. M. Saville, "Optimisation of dallenbach layers using real materials," 2007. [Online]. Available: https://api.semanticscholar.org/CorpusID:107373462.

[20] M. F. Elmahaishi, R. S. Azis, I. Ismail, and F. D. Muhammad, "A review on electromagnetic microwave absorption properties: Their materials and performance,"
Journal of Materials Research and Technology, vol. 20, pp. 2188–2220, 2022, ISSN: 2238-7854. DOI: 10.1016/j.jmrt.2022.07.140. [Online]. Available: https://www.sciencedirect.com/science/article/pii/S2238785422012017.

[21] Y. Kotsuka,
Electromagnetic Wave Absorbers : Detailed Theories and Applications.
John Wiley amp; Sons, Incorporated, 2019, ISBN: 9781119564140.
[Online]. Available:
https://search.ebscohost.com/login.aspx?direct=true&db=cat07472a&AN=clec.EBC5896732&site=eds-live&scope=site&authtype=guest&custid=s3911979&groupid=main&profile=eds.

[22] L. P. Materials. "Eccosorb™ fgm." (), [Online]. Available:
https://www.laird.com/products/absorbers/thin-elastomer-absorbers/silicone-elastomer-sheet/free-space-absorbers/eccosorb-fgm.

[23] Y. Kotsuka,
Electromagnetic Wave Absorbers : Detailed Theories and Applications.
John Wiley amp; Sons, Incorporated, 2019, p. 72, ISBN: 9781119564140.
[Online]. Available:
https://search.ebscohost.com/login.aspx?direct=true&db=cat07472a&AN=clec.EBC5896732&site=eds-live&scope=site&authtype=guest&custid=s3911979&groupid=main&profile=eds.

[24] T. V. I. for Artificial Electromagnetic Materials and Metamaterials. "Metamaterials." (), [Online]. Available:
https://www.metamorphose-vi.org/index.php/metamaterials.

[25] J. B. Pendry, D. Schurig, and D. R. Smith, "Controlling electromagnetic fields," *Science*, vol. 312, no. 5781, pp. 1780–1782, 2006.
DOI: 10.1126/science.1125907. [Online]. Available:
https://www.science.org/doi/abs/10.1126/science.1125907.

[26] P. Alitalo and S. Tretyakov, "Electromagnetic cloaking with metamaterials," *Materials Today*, vol. 12, Mar. 2009. DOI: 10.1016/S1369-7021(09)70072-0.

[27] W. Cai, U. Chettiar, A. Kildishev, and V. Shalaev, "Optical cloaking with metamaterials. nat photonics 1:224-227,"
Birck and NCN Publications, vol. 1, Apr. 2007.
DOI: 10.1038/nphoton.2007.28.

[28] Ansys. “Ansys electronics | electronic design electromagnetics simulation.” (), [Online]. Available: https://www.ansys.com/products/electronics.

[29] Ansys. “Ansys hfss | 3d high frequency simulation software.” (), [Online]. Available: https://www.ansys.com/products/electronics/ansys-hfss.

A

MATLAB code

In this section, the MATLAB script *main.m* which was used to post-process all the simulated Ansys HFSS data is shown, as well as all its used MATLAB functions. Additionally, the initial data loading code of *main.m* specifies the performed antenna and obstruction simulations, including each result's implemented method and obtained accuracy.

A.1 Script *main.m*

```
%% Script for import, post-processing and plotting of simulation data from HFSS

% Load data:
element_list = 1:21;
% Reference (no obstruction):
data_WG21x1 = import_hfss_element_patterns(element_list,'
    WG_21x1_NoPole_NoAbs_AutoMesh_0dot005conv_FEBI_20240318_E_');
% Pole diameter 5 cm:
% Pole @ 1 m, 2 m, 3 m, 4 m, 5 m, 10 m, 20 m & 30 m:
data_5cm5mP_1m = import_hfss_element_patterns(element_list,'
    WG_21x1_5cm5mPole_NoAbs_AutoMesh_0dot005conv_1000mmZ_FEBIandIE_20240320_E_');
data_5cm5mP_2m = import_hfss_element_patterns(element_list,'
    WG_21x1_5cm5mPole_NoAbs_AutoMesh_0dot005conv_2000mmZ_FEBIandIE_20240320_E_');
data_5cm5mP_3m = import_hfss_element_patterns(element_list,'
    WG_21x1_5cm5mPole_NoAbs_AutoMesh_0dot005conv_3000mmZ_FEBIandIE_20240320_E_');
data_5cm5mP_4m = import_hfss_element_patterns(element_list,'
    WG_21x1_5cm5mPole_NoAbs_AutoMesh_0dot005conv_4000mmZ_FEBIandIE_20240318_E_');
data_5cm5mP_5m = import_hfss_element_patterns(element_list,'
    WG_21x1_5cm5mPole_NoAbs_AutoMesh_0dot005conv_5000mmZ_FEBIandIE_20240320_E_');
data_5cm5mP_10m = import_hfss_element_patterns(element_list,'
    WG_21x1_5cm5mPole_NoAbs_20mmMesh_0dot005conv_10meterZ_FEBIandIE_20240327_E_');
data_5cm5mP_20m = import_hfss_element_patterns(element_list,'
    WG_21x1_5cm5mPole_NoAbs_20mmMesh_0dot005conv_20meterZ_FEBIandIE_20240402_E_');
data_5cm5mP_30m = import_hfss_element_patterns(element_list,'
    WG_21x1_5cm5mPole_NoAbs_20mmMesh_0dot005conv_30meterZ_FEBIandIE_20240402_E_');
% Pole + FGM125 @ 1 m, 2 m, 3 m, 4 m, 5 m, 10 m, 20 m & 30 m:
data_5cm5mP_1m_FGM125 = import_hfss_element_patterns(element_list,'
    WG_21x1_5cm5mPole_FGM125_20mmMesh_0dot005conv_1000mmZ_FEBIandFEBI_20240318_E_');
data_5cm5mP_2m_FGM125 = import_hfss_element_patterns(element_list,'
    WG_21x1_5cm5mPole_FGM125_20mmMesh_0dot005conv_2000mmZ_FEBIandFEBI_20240318_E_');
data_5cm5mP_3m_FGM125 = import_hfss_element_patterns(element_list,'
    WG_21x1_5cm5mPole_FGM125_20mmMesh_0dot005conv_3000mmZ_FEBIandFEBI_20240318_E_');
data_5cm5mP_4m_FGM125 = import_hfss_element_patterns(element_list,'
    WG_21x1_5cm5mPole_FGM125_20mmMesh_0dot005conv_4000mmZ_FEBIandFEBI_20240318_E_');
data_5cm5mP_5m_FGM125 = import_hfss_element_patterns(element_list,'
    WG_21x1_5cm5mPole_FGM125_20mmMesh_0dot005conv_5000mmZ_FEBIandFEBI_20240318_E_');
data_5cm5mP_10m_FGM125 = import_hfss_element_patterns(element_list,'
    WG_21x1_5cm5mPole_FGM125_20mmMesh_0dot005conv_10meterZ_FEBIandFEBI_20240410_Linux_E_');
data_5cm5mP_20m_FGM125 = import_hfss_element_patterns(element_list,'
    WG_21x1_5cm5mPole_FGM125_20mmMesh_0dot005conv_20meterZ_FEBIandFEBI_20240411_Linux_E_');
data_5cm5mP_30m_FGM125 = import_hfss_element_patterns(element_list,'
    WG_21x1_5cm5mPole_FGM125_20mmMesh_0dot005conv_30meterZ_FEBIandFEBI_20240411_Linux_E_');
```

```
% Pole + RombPEC @ 3 m, 30 deg & 37.5 deg:
data_5cm5mP_3m_RombPEC30deg = import_hfss_element_patterns(element_list,'
    WG_21x1_5cm5mPole_RombPEC30deg_20mmMesh_0dot005conv_3meterZ_FEBIandIE_20240415_Linux_E_');
data_5cm5mP_3m_RombPEC37dot5deg = import_hfss_element_patterns(element_list,'
    WG_21x1_5cm5mPole_RombPEC37dot5deg_20mmMesh_0dot005conv_3meterZ_FEBIandIE_20240415_Linux_E_');
% Pole + RombPEC45deg @ 1 m, 2 m, 3 m, 4 m, 5 m, 10 m, 20 m & 30 m:
data_5cm5mP_1m_RombPEC45deg = import_hfss_element_patterns(element_list,'
    WG_21x1_5cm5mPole_RombPEC45deg_AutoMesh_0dot005conv_1meterZ_FEBIandIE_20240429_Linux_E_');
data_5cm5mP_2m_RombPEC45deg = import_hfss_element_patterns(element_list,'
    WG_21x1_5cm5mPole_RombPEC45deg_AutoMesh_0dot005conv_2meterZ_FEBIandIE_20240429_Linux_E_');
data_5cm5mP_3m_RombPEC45deg = import_hfss_element_patterns(element_list,'
    WG_21x1_5cm5mPole_RombPEC45deg_AutoMesh_0dot005conv_3meterZ_FEBIandIE_20240429_Linux_E_');
data_5cm5mP_4m_RombPEC45deg = import_hfss_element_patterns(element_list,'
    WG_21x1_5cm5mPole_RombPEC45deg_AutoMesh_0dot005conv_4meterZ_FEBIandIE_20240429_Linux_E_');
data_5cm5mP_5m_RombPEC45deg = import_hfss_element_patterns(element_list,'
    WG_21x1_5cm5mPole_RombPEC45deg_AutoMesh_0dot005conv_5meterZ_FEBIandIE_20240429_Linux_E_');
data_5cm5mP_10m_RombPEC45deg = import_hfss_element_patterns(element_list,'
    WG_21x1_5cm5mPole_RombPEC45deg_AutoMesh_0dot005conv_10meterZ_FEBIandIE_20240429_Linux_E_');
data_5cm5mP_20m_RombPEC45deg = import_hfss_element_patterns(element_list,'
    WG_21x1_5cm5mPole_RombPEC45deg_AutoMesh_0dot005conv_20meterZ_FEBIandIE_20240429_Linux_E_');
data_5cm5mP_30m_RombPEC45deg = import_hfss_element_patterns(element_list,'
    WG_21x1_5cm5mPole_RombPEC45deg_AutoMesh_0dot005conv_30meterZ_FEBIandIE_20240429_Linux_E_');
% Pole + RombABS @ 3 m, 30 deg & 37.5 deg:
data_5cm5mP_3m_RombABS30deg = import_hfss_element_patterns(element_list,'
    WG_21x1_5cm5mPole_RombABS30deg_30mmMesh_0dot05conv_3meterZ_FEBIandFEBI_20240515_Linux_E_');
data_5cm5mP_3m_RombABS37dot5deg = import_hfss_element_patterns(element_list,'
    WG_21x1_5cm5mPole_RombABS37dot5deg_30mmMesh_0dot05conv_3meterZ_FEBIandFEBI_20240515_Linux_E_');
% Pole + RombBAS45deg @ 1 m, 2 m, 3 m, 4 m, 5 m, 10 m, 20 m & 30 m:
data_5cm5mP_1m_RombABS45deg = import_hfss_element_patterns(element_list,'
    WG_21x1_5cm5mPole_RombABS45deg_20mmMesh_0dot005conv_1meterZ_FEBIandFEBI_20240507_Linux_E_');
data_5cm5mP_2m_RombABS45deg = import_hfss_element_patterns(element_list,'
    WG_21x1_5cm5mPole_RombABS45deg_20mmMesh_0dot005conv_2meterZ_FEBIandFEBI_20240507_Linux_E_');
data_5cm5mP_3m_RombABS45deg = import_hfss_element_patterns(element_list,'
    WG_21x1_5cm5mPole_RombABS45deg_20mmMesh_0dot005conv_3meterZ_FEBIandFEBI_20240507_Linux_E_');
data_5cm5mP_4m_RombABS45deg = import_hfss_element_patterns(element_list,'
    WG_21x1_5cm5mPole_RombABS45deg_20mmMesh_0dot005conv_4meterZ_FEBIandFEBI_20240507_Linux_E_');
data_5cm5mP_5m_RombABS45deg = import_hfss_element_patterns(element_list,'
    WG_21x1_5cm5mPole_RombABS45deg_20mmMesh_0dot005conv_5meterZ_FEBIandFEBI_20240507_Linux_E_');
data_5cm5mP_10m_RombABS45deg = import_hfss_element_patterns(element_list,'
    WG_21x1_5cm5mPole_RombABS45deg_20mmMesh_0dot005conv_10meterZ_FEBIandFEBI_20240507_Linux_E_');
data_5cm5mP_20m_RombABS45deg = import_hfss_element_patterns(element_list,'
    WG_21x1_5cm5mPole_RombABS45deg_20mmMesh_0dot005conv_20meterZ_FEBIandFEBI_20240507_Linux_E_');
data_5cm5mP_30m_RombABS45deg = import_hfss_element_patterns(element_list,'
    WG_21x1_5cm5mPole_RombABS45deg_20mmMesh_0dot005conv_30meterZ_FEBIandFEBI_20240507_Linux_E_');
% Pole + RombDiPEC45deg @ 1 m, 2 m, 3 m, 4 m, 5 m, 10 m, 20 m & 30 m:
data_5cm5mP_1m_RombDiPEC45deg = import_hfss_element_patterns(element_list,'
    WG_21x1_5cm5mPole_RombDiPEC45deg_AutoMesh_0dot05_1meterZ_FEBIandFEBI_20240506_E_');
data_5cm5mP_2m_RombDiPEC45deg = import_hfss_element_patterns(element_list,'
    WG_21x1_5cm5mPole_RombDiPEC45deg_AutoMesh_0dot05_2meterZ_FEBIandFEBI_20240506_E_');
data_5cm5mP_3m_RombDiPEC45deg = import_hfss_element_patterns(element_list,'
    WG_21x1_5cm5mPole_RombDiPEC45deg_AutoMesh_0dot05_3meterZ_FEBIandFEBI_20240506_E_');
data_5cm5mP_4m_RombDiPEC45deg = import_hfss_element_patterns(element_list,'
    WG_21x1_5cm5mPole_RombDiPEC45deg_AutoMesh_0dot05_4meterZ_FEBIandFEBI_20240506_E_');
data_5cm5mP_5m_RombDiPEC45deg = import_hfss_element_patterns(element_list,'
    WG_21x1_5cm5mPole_RombDiPEC45deg_AutoMesh_0dot05_5meterZ_FEBIandFEBI_20240506_E_');
data_5cm5mP_10m_RombDiPEC45deg = import_hfss_element_patterns(element_list,'
    WG_21x1_5cm5mPole_RombDiPEC45deg_AutoMesh_0dot05_10meterZ_FEBIandFEBI_20240514_E_');
data_5cm5mP_20m_RombDiPEC45deg = import_hfss_element_patterns(element_list,'
    WG_21x1_5cm5mPole_RombDiPEC45deg_AutoMesh_0dot05_20meterZ_FEBIandFEBI_20240514_E_');
data_5cm5mP_30m_RombDiPEC45deg = import_hfss_element_patterns(element_list,'
    WG_21x1_5cm5mPole_RombDiPEC45deg_AutoMesh_0dot05_30meterZ_FEBIandFEBI_20240514_E_');
% Pole diameter 10 cm:
% Pole @ 1 m, 2 m, 3 m, 4 m, 5 m, 10 m, 20 m & 30 m:
data_10cm5mP_1m = import_hfss_element_patterns(element_list,'
    WG_21x1_10cm5mPole_NoAbs_30mmMesh_0dot005conv_1000mmZ_FEBIandFEBI_20240315_E_');
data_10cm5mP_2m = import_hfss_element_patterns(element_list,'
    WG_21x1_10cm5mPole_NoAbs_30mmMesh_0dot005conv_2000mmZ_FEBIandFEBI_20240315_E_');
data_10cm5mP_3m = import_hfss_element_patterns(element_list,'
    WG_21x1_10cm5mPole_NoAbs_30mmMesh_0dot005conv_3000mmZ_FEBIandFEBI_20240315_E_');
```

```
data_10cm5mP_4m = import_hfss_element_patterns(element_list,'
    WG_21x1_10cm5mPole_NoAbs_30mmMesh_0dot005conv_4000mmZ_FEBIandFEBI_20240315_E_');
data_10cm5mP_5m = import_hfss_element_patterns(element_list,'
    WG_21x1_10cm5mPole_NoAbs_30mmMesh_0dot005conv_5000mmZ_FEBIandFEBI_20240315_E_');
data_10cm5mP_10m = import_hfss_element_patterns(element_list,'
    WG_21x1_10cm5mPole_NoAbs_30mmMesh_0dot005conv_10meterZ_FEBIandIE_20240327_E_');
data_10cm5mP_20m = import_hfss_element_patterns(element_list,'
    WG_21x1_10cm5mPole_NoAbs_30mmMesh_0dot005conv_20meterZ_FEBIandIE_20240327_E_');
data_10cm5mP_30m = import_hfss_element_patterns(element_list,'
    WG_21x1_10cm5mPole_NoAbs_30mmMesh_0dot005conv_30meterZ_FEBIandIE_20240327_E_');
% Pole + FGM125 @ 1 m, 2 m, 3 m, 4 m, 5 m, 10 m, 20 m & 30 m:
data_10cm5mP_1m_FGM125 = import_hfss_element_patterns(element_list,'
    WG_21x1_10cm5mPole_FGM125_30mmMesh_0dot005conv_1000mmZ_FEBIandFEBI_20240320_E_');
data_10cm5mP_2m_FGM125 = import_hfss_element_patterns(element_list,'
    WG_21x1_10cm5mPole_FGM125_30mmMesh_0dot005conv_2000mmZ_FEBIandFEBI_20240320_E_');
data_10cm5mP_3m_FGM125 = import_hfss_element_patterns(element_list,'
    WG_21x1_10cm5mPole_FGM125_30mmMesh_0dot005conv_3000mmZ_FEBIandFEBI_20240320_E_');
data_10cm5mP_4m_FGM125 = import_hfss_element_patterns(element_list,'
    WG_21x1_10cm5mPole_FGM125_30mmMesh_0dot005conv_4000mmZ_FEBIandFEBI_20240320_E_');
data_10cm5mP_5m_FGM125 = import_hfss_element_patterns(element_list,'
    WG_21x1_10cm5mPole_FGM125_30mmMesh_0dot005conv_5000mmZ_FEBIandFEBI_20240320_E_');
data_10cm5mP_10m_FGM125 = import_hfss_element_patterns(element_list,'
    WG_21x1_10cm5mPole_FGM125_30mmMesh_0dot005conv_10meterZ_FEBIandFEBI_20240410_Linux_E_');
data_10cm5mP_20m_FGM125 = import_hfss_element_patterns(element_list,'
    WG_21x1_10cm5mPole_FGM125_30mmMesh_0dot005conv_20meterZ_FEBIandFEBI_20240410_Linux_E_');
data_10cm5mP_30m_FGM125 = import_hfss_element_patterns(element_list,'
    WG_21x1_10cm5mPole_FGM125_30mmMesh_0dot005conv_30meterZ_FEBIandFEBI_20240410_Linux_E_');
% Pole + RombPEC @ 3 m, 30 deg & 37.5 deg:
data_10cm5mP_3m_RombPEC30deg = import_hfss_element_patterns(element_list,'
    WG_21x1_10cm5mPole_RombPEC30deg_20mmMesh_0dot005conv_3meterZ_FEBIandIE_20240423_Linux_E_');
data_10cm5mP_3m_RombPEC37dot5deg = import_hfss_element_patterns(element_list,'
    WG_21x1_10cm5mPole_RombPEC37dot5deg_20mmMesh_0dot005conv_3meterZ_FEBIandIE_20240423_Linux_E_');
% Pole + RombPEC45deg @ 1 m, 2 m, 3 m, 4 m, 5 m, 10 m, 20 m & 30 m:
data_10cm5mP_1m_RombPEC45deg = import_hfss_element_patterns(element_list,'
    WG_21x1_10cm5mPole_RombPEC45deg_AutoMesh_0dot005conv_1meterZ_FEBIandIE_20240429_Linux_E_');
data_10cm5mP_2m_RombPEC45deg = import_hfss_element_patterns(element_list,'
    WG_21x1_10cm5mPole_RombPEC45deg_AutoMesh_0dot005conv_2meterZ_FEBIandIE_20240429_Linux_E_');
data_10cm5mP_3m_RombPEC45deg = import_hfss_element_patterns(element_list,'
    WG_21x1_10cm5mPole_RombPEC45deg_AutoMesh_0dot005conv_3meterZ_FEBIandIE_20240429_Linux_E_');
data_10cm5mP_4m_RombPEC45deg = import_hfss_element_patterns(element_list,'
    WG_21x1_10cm5mPole_RombPEC45deg_AutoMesh_0dot005conv_4meterZ_FEBIandIE_20240429_Linux_E_');
data_10cm5mP_5m_RombPEC45deg = import_hfss_element_patterns(element_list,'
    WG_21x1_10cm5mPole_RombPEC45deg_AutoMesh_0dot005conv_5meterZ_FEBIandIE_20240429_Linux_E_');
data_10cm5mP_10m_RombPEC45deg = import_hfss_element_patterns(element_list,'
    WG_21x1_10cm5mPole_RombPEC45deg_AutoMesh_0dot005conv_10meterZ_FEBIandIE_20240429_Linux_E_');
data_10cm5mP_20m_RombPEC45deg = import_hfss_element_patterns(element_list,'
    WG_21x1_10cm5mPole_RombPEC45deg_AutoMesh_0dot005conv_20meterZ_FEBIandIE_20240429_Linux_E_');
data_10cm5mP_30m_RombPEC45deg = import_hfss_element_patterns(element_list,'
    WG_21x1_10cm5mPole_RombPEC45deg_AutoMesh_0dot005conv_30meterZ_FEBIandIE_20240429_Linux_E_');
% Pole + RombABS @ 3 m, 30 deg & 37.5 deg:
data_10cm5mP_3m_RombABS30deg = import_hfss_element_patterns(element_list,'
    WG_21x1_10cm5mPole_RombABS30deg_30mmMesh_0dot05conv_3meterZ_FEBIandFEBI_20240515_Linux_E_');
data_10cm5mP_3m_RombABS37dot5deg = import_hfss_element_patterns(element_list,'
    WG_21x1_10cm5mPole_RombABS37dot5deg_30mmMesh_0dot05conv_3meterZ_FEBIandFEBI_20240515_Linux_E_');
% Pole + RombBAS45deg @ 1 m, 2 m, 3 m, 4 m, 5 m, 10 m, 20 m & 30 m:
data_10cm5mP_1m_RombABS45deg = import_hfss_element_patterns(element_list,'
    WG_21x1_10cm5mPole_RombABS45deg_30mmMesh_0dot005conv_1meterZ_FEBIandFEBI_20240510_Linux_E_');
data_10cm5mP_2m_RombABS45deg = import_hfss_element_patterns(element_list,'
    WG_21x1_10cm5mPole_RombABS45deg_30mmMesh_0dot005conv_2meterZ_FEBIandFEBI_20240510_Linux_E_');
data_10cm5mP_3m_RombABS45deg = import_hfss_element_patterns(element_list,'
    WG_21x1_10cm5mPole_RombABS45deg_30mmMesh_0dot005conv_3meterZ_FEBIandFEBI_20240510_Linux_E_');
data_10cm5mP_4m_RombABS45deg = import_hfss_element_patterns(element_list,'
    WG_21x1_10cm5mPole_RombABS45deg_30mmMesh_0dot005conv_4meterZ_FEBIandFEBI_20240510_Linux_E_');
data_10cm5mP_5m_RombABS45deg = import_hfss_element_patterns(element_list,'
    WG_21x1_10cm5mPole_RombABS45deg_30mmMesh_0dot005conv_5meterZ_FEBIandFEBI_20240510_Linux_E_');
data_10cm5mP_10m_RombABS45deg = import_hfss_element_patterns(element_list,'
    WG_21x1_10cm5mPole_RombABS45deg_30mmMesh_0dot005conv_10meterZ_FEBIandFEBI_20240510_Linux_E_');
data_10cm5mP_20m_RombABS45deg = import_hfss_element_patterns(element_list,'
    WG_21x1_10cm5mPole_RombABS45deg_30mmMesh_0dot005conv_20meterZ_FEBIandFEBI_20240510_Linux_E_');
```

```
data_10cm5mP_30m_RombABS45deg = import_hfss_element_patterns(element_list,'
    WG_21x1_10cm5mPole_RombABS45deg_30mmMesh_0dot005conv_30meterZ_FEBIandFEBI_20240510_Linux_E_');
% Pole + RombDiPEC45deg @ 1 m, 2 m, 3 m, 4 m, 5 m, 10 m, 20 m & 30 m:
data_10cm5mP_1m_RombDiPEC45deg = import_hfss_element_patterns(element_list,'
    WG_21x1_10cm5mPole_RombDiPEC45deg_AutoMesh_0dot05_1meterZ_FEBIandFEBI_20240506_E_');
data_10cm5mP_2m_RombDiPEC45deg = import_hfss_element_patterns(element_list,'
    WG_21x1_10cm5mPole_RombDiPEC45deg_AutoMesh_0dot05_2meterZ_FEBIandFEBI_20240506_E_');
data_10cm5mP_3m_RombDiPEC45deg = import_hfss_element_patterns(element_list,'
    WG_21x1_10cm5mPole_RombDiPEC45deg_AutoMesh_0dot05_3meterZ_FEBIandFEBI_20240506_E_');
data_10cm5mP_4m_RombDiPEC45deg = import_hfss_element_patterns(element_list,'
    WG_21x1_10cm5mPole_RombDiPEC45deg_AutoMesh_0dot05_4meterZ_FEBIandFEBI_20240506_E_');
data_10cm5mP_5m_RombDiPEC45deg = import_hfss_element_patterns(element_list,'
    WG_21x1_10cm5mPole_RombDiPEC45deg_AutoMesh_0dot05_5meterZ_FEBIandFEBI_20240506_E_');
data_10cm5mP_10m_RombDiPEC45deg = import_hfss_element_patterns(element_list,'
    WG_21x1_10cm5mPole_RombDiPEC45deg_AutoMesh_0dot05_10meterZ_FEBIandFEBI_20240513_E_');
data_10cm5mP_20m_RombDiPEC45deg = import_hfss_element_patterns(element_list,'
    WG_21x1_10cm5mPole_RombDiPEC45deg_AutoMesh_0dot05_20meterZ_FEBIandFEBI_20240513_E_');
data_10cm5mP_30m_RombDiPEC45deg = import_hfss_element_patterns(element_list,'
    WG_21x1_10cm5mPole_RombDiPEC45deg_AutoMesh_0dot05_30meterZ_FEBIandFEBI_20240513_E_');

%% Rearrange data:
diam_poles = [5, 10]; % Pole diameters [cm]
dist_poles = [1, 2, 3, 4, 5, 10, 20, 30]; % Pole distances [m]
data_ref = data_WG21x1;
data_5cm5mP_poles = [data_5cm5mP_1m; data_5cm5mP_2m; data_5cm5mP_3m; data_5cm5mP_4m; data_5cm5mP_5m;
    data_5cm5mP_10m; data_5cm5mP_20m; data_5cm5mP_30m]; % rows: different pole distance
data_10cm5mP_poles = [data_10cm5mP_1m; data_10cm5mP_2m; data_10cm5mP_3m; data_10cm5mP_4m;
    data_10cm5mP_5m; data_10cm5mP_10m; data_10cm5mP_20m; data_10cm5mP_30m]; % rows: different pole
    distance
data_poles = [data_5cm5mP_poles, data_10cm5mP_poles]; % cols: different pole diameter, (pole distances,
    pole diameters)
legend_shells = ["S1","S2","S3","S4","S2'","S3'"];
% Shell 1: FGM-125
data_5cm5mP_FGM125_poles = [data_5cm5mP_1m_FGM125; data_5cm5mP_2m_FGM125; data_5cm5mP_3m_FGM125;
    data_5cm5mP_4m_FGM125; data_5cm5mP_5m_FGM125; data_5cm5mP_10m_FGM125; data_5cm5mP_20m_FGM125;
    data_5cm5mP_30m_FGM125];
data_10cm5mP_FGM125_poles = [data_10cm5mP_1m_FGM125; data_10cm5mP_2m_FGM125; data_10cm5mP_3m_FGM125;
    data_10cm5mP_4m_FGM125; data_10cm5mP_5m_FGM125; data_10cm5mP_10m_FGM125; data_10cm5mP_20m_FGM125;
    data_10cm5mP_30m_FGM125];
data_poles_FGM125 = [data_5cm5mP_FGM125_poles, data_10cm5mP_FGM125_poles];
% Shell 2: RombPEC
data_5cm5mP_RombPEC_poles = [data_5cm5mP_1m_RombPEC45deg; data_5cm5mP_2m_RombPEC45deg;
    data_5cm5mP_3m_RombPEC45deg; data_5cm5mP_4m_RombPEC45deg; data_5cm5mP_5m_RombPEC45deg;
    data_5cm5mP_10m_RombPEC45deg; data_5cm5mP_20m_RombPEC45deg; data_5cm5mP_30m_RombPEC45deg];
data_10cm5mP_RombPEC_poles = [data_10cm5mP_1m_RombPEC45deg; data_10cm5mP_2m_RombPEC45deg;
    data_10cm5mP_3m_RombPEC45deg; data_10cm5mP_4m_RombPEC45deg; data_10cm5mP_5m_RombPEC45deg;
    data_10cm5mP_10m_RombPEC45deg; data_10cm5mP_20m_RombPEC45deg; data_10cm5mP_30m_RombPEC45deg];
data_poles_RombPEC = [data_5cm5mP_RombPEC_poles, data_10cm5mP_RombPEC_poles];
% Shell 3: RombABS
data_5cm5mP_RombABS_poles = [data_5cm5mP_1m_RombABS45deg; data_5cm5mP_2m_RombABS45deg;
    data_5cm5mP_3m_RombABS45deg; data_5cm5mP_4m_RombABS45deg; data_5cm5mP_5m_RombABS45deg;
    data_5cm5mP_10m_RombABS45deg; data_5cm5mP_20m_RombABS45deg; data_5cm5mP_30m_RombABS45deg];
data_10cm5mP_RombABS_poles = [data_10cm5mP_1m_RombABS45deg; data_10cm5mP_2m_RombABS45deg;
    data_10cm5mP_3m_RombABS45deg; data_10cm5mP_4m_RombABS45deg; data_10cm5mP_5m_RombABS45deg;
    data_10cm5mP_10m_RombABS45deg; data_10cm5mP_20m_RombABS45deg; data_10cm5mP_30m_RombABS45deg];
data_poles_RombABS = [data_5cm5mP_RombABS_poles, data_10cm5mP_RombABS_poles];
% Shell 4: RombDiPEC
data_5cm5mP_RombDiPEC_poles = [data_5cm5mP_1m_RombDiPEC45deg; data_5cm5mP_2m_RombDiPEC45deg;
    data_5cm5mP_3m_RombDiPEC45deg; data_5cm5mP_4m_RombDiPEC45deg; data_5cm5mP_5m_RombDiPEC45deg;
    data_5cm5mP_10m_RombDiPEC45deg; data_5cm5mP_20m_RombDiPEC45deg; data_5cm5mP_30m_RombDiPEC45deg];
data_10cm5mP_RombDiPEC_poles = [data_10cm5mP_1m_RombDiPEC45deg; data_10cm5mP_2m_RombDiPEC45deg;
    data_10cm5mP_3m_RombDiPEC45deg; data_10cm5mP_4m_RombDiPEC45deg; data_10cm5mP_5m_RombDiPEC45deg;
    data_10cm5mP_10m_RombDiPEC45deg; data_10cm5mP_20m_RombDiPEC45deg; data_10cm5mP_30m_RombDiPEC45deg];
data_poles_RombDiPEC = [data_5cm5mP_RombDiPEC_poles, data_10cm5mP_RombDiPEC_poles];
% Shell 2', RombPEC @ 3 m, 30 deg, 37.5 deg & 45 deg
FillOut = data_5cm5mP_3m_RombPEC45deg;
data_5cm5mP_RombPEC_3poles3m = [data_5cm5mP_3m_RombPEC30deg; data_5cm5mP_3m_RombPEC37dot5deg;
    data_5cm5mP_3m_RombPEC45deg; FillOut; FillOut; FillOut; FillOut; FillOut];
FillOut = data_10cm5mP_3m_RombPEC45deg;
```

```
data_10cm5mP_RombPEC_3poles3m = [data_10cm5mP_3m_RombPEC30deg; data_10cm5mP_3m_RombPEC37dot5deg;
    data_10cm5mP_3m_RombPEC45deg; FillOut; FillOut; FillOut; FillOut; FillOut];
data_3poles3m_RombPEC = [data_5cm5mP_RombPEC_3poles3m, data_10cm5mP_RombPEC_3poles3m];
% Shell 3', test of angles:
FillOut = data_5cm5mP_3m_RombABS45deg;
data_5cm5mP_RombABS_3poles3m = [data_5cm5mP_3m_RombABS30deg; data_5cm5mP_3m_RombABS37dot5deg;
    data_5cm5mP_3m_RombABS45deg; FillOut; FillOut; FillOut; FillOut; FillOut];
FillOut = data_10cm5mP_3m_RombABS45deg;
data_10cm5mP_RombABS_3poles3m = [data_10cm5mP_3m_RombABS30deg; data_10cm5mP_3m_RombABS37dot5deg;
    data_10cm5mP_3m_RombABS45deg; FillOut; FillOut; FillOut; FillOut; FillOut];
data_3poles3m_RombABS = [data_5cm5mP_RombABS_3poles3m, data_10cm5mP_RombABS_3poles3m];
data_poles_shells = [data_poles_FGM125, data_poles_RombPEC, data_poles_RombABS, data_poles_RombDiPEC,
    data_3poles3m_RombPEC, data_3poles3m_RombABS];

% Select/define the desired data:
pol = 2; % Phi polarization (=vertical!)
fc = 9.5*10^9; % Frequency [Hz]
N = length(element_list); Nx = N; % Number of elements in one direction (e.g. 31x3 array then N=93 and
    Nx=31)
phi_plot = 0; % The phi values [deg] for plot, e.g. [0, 10, 20, 30];
phi_slice = 0; % One value of phi [deg]
taylor_nn_sl = [3, 31]; % [nn, sl] for TAYLORTAP_LIN(length,nn,sl)
% length: number of elements, nn: number of equally large sidelobes before the attenuation is increased,
     sl: number of dB the first sidelobe should be attenuated
% Default matlab colors:
mat_blue = [0, 0.4470, 0.7410];
mat_red = [0.8500, 0.3250, 0.0980];
mat_yellow = [0.9290, 0.6940, 0.1250];
mat_purple = [0.4940, 0.1840, 0.5560];
mat_green = [0.4660, 0.6740, 0.1880];
mat_lightblue = [0.3010, 0.7450, 0.9330];
mat_winered = [0.6350, 0.0780, 0.1840];
mat_colors = [mat_blue; mat_red; mat_yellow; mat_purple; mat_green; mat_lightblue; mat_winered];
% Default matlab colors, somewhat lighter:
mat_blue_old = [122, 202, 255]/255;
mat_red_old = [255, 165, 126]/255;
mat_yellow_old = [255, 226, 158]/255;
mat_purple_old = [198, 132, 212]/255;
mat_green_old = [197, 235, 148]/255;
mat_lightblue_old = [200, 238, 255]/255;
mat_winered_old = [224, 123, 142]/255;
mat_colors_old = [mat_blue_old; mat_red_old; mat_yellow_old; mat_purple_old; mat_green_old;
    mat_lightblue_old; mat_winered_old];

%% Calculate realized gain and ASLL for steering_angle [deg], for U taper and specified T taper
steering_angle = 0; % Steering angle [deg]
% Calculate realized gain and ASLL for steering_angle [deg], for uniform taper and taylor taper:
[RG_data_ref_U,RG_data_ref_T, ASLL_data_ref_U, ASLL_data_ref_T] = sa_RG_ASLL(data_ref,pol,fc,phi_slice,
    phi_plot,steering_angle, N, Nx, taylor_nn_sl);
% Initialize for further calculations, (rows: pole distances, cols: theta values)
init_poles = zeros(length(data_ref.ax1),length(dist_poles),length(diam_poles)); % Assumes the same theta
     resolution of the exported data (which we do have though)
init_poles_shells = zeros(length(data_ref.ax1),length(dist_poles),length(diam_poles),length(
    legend_shells)); % Assumes the same theta resolution of the exported data (which we do have though)
RG_data_poles_U = init_poles; RG_data_poles_T = init_poles; % (RG, pole distances, pole diameters)
ASLL_data_poles_U = init_poles; ASLL_data_poles_T = init_poles;
RG_data_poles_shells_U = init_poles_shells; RG_data_poles_shells_T = init_poles_shells;
ASLL_data_poles_shells_U = init_poles_shells; ASLL_data_poles_shells_T = init_poles_shells;
for k=1:length(dist_poles) % Go through all pole distances
    % Calculate realized gain and ASLL for steering_angle [deg], for uniform taper and taylor taper:
    for d=1:length(diam_poles) % Go through all pole diameters
        % Poles:
        [RG_data_poles_U(:,k,d),RG_data_poles_T(:,k,d), ASLL_data_poles_U(:,k,d), ASLL_data_poles_T(:,k,
            d)] = sa_RG_ASLL(data_poles(k,d), pol,fc, phi_slice, phi_plot, steering_angle, N, Nx,
            taylor_nn_sl);
        % Poles + shells:
        for s=1:length(legend_shells) % For all types of shells (pole+shell)
            % d+2*(s-1) such that each struct is found correctly!
            [RG_data_poles_shells_U(:,k,d,s),RG_data_poles_shells_T(:,k,d,s), ASLL_data_poles_shells_U
                (:,k,d,s), ASLL_data_poles_shells_T(:,k,d,s)] = sa_RG_ASLL(data_poles_shells(k, d+2*(s
```

```
                -1)), pol, fc, phi_slice, phi_plot, steering_angle, N, Nx, taylor_nn_sl);
        end
    end
end
disp("Calculations of realized gain and ASLL for steering angle "+steering_angle+"° complete!"))

%% Calculate realized gain and ASLL for steering_angles [deg], for U taper and specified T taper
steering_angles = -45:1:+45; % Steering angles [deg]
select_MRG_at_sa = true; % true/false
[RGmaxdB_data_ref_U, RGmaxdB_data_ref_T, ASLLdB_data_ref_U, ASLLdB_data_ref_T] = sas_MaxRG_ASLL(data_ref
    ,pol,fc,phi_slice,phi_plot,steering_angles, N, Nx, taylor_nn_sl,select_MRG_at_sa);
% Initialize for further calculations, (rows: pole distances, cols: theta values)
init_poles_ = zeros(length(steering_angles),length(dist_poles),length(diam_poles));
init_poles_shells_ = zeros(length(steering_angles),length(dist_poles),length(diam_poles),length(
    legend_shells));
RGmaxdB_data_poles_U = init_poles_; RGmaxdB_data_poles_T = init_poles_; % (RGmaxdB, pole distances, pole
     diameters)
ASLLdB_data_poles_U = init_poles_; ASLLdB_data_poles_T = init_poles_;
RGmaxdB_data_poles_shells_U = init_poles_shells_; RGmaxdB_data_poles_shells_T = init_poles_shells_;
ASLLdB_data_poles_shells_U = init_poles_shells_; ASLLdB_data_poles_shells_T = init_poles_shells_;
for k=1:length(dist_poles) % Go through all pole distances
    % Calculate realized gain and ASLL for steering_angle [deg], for uniform taper and taylor taper:
    for d=1:length(diam_poles) % Go through all pole diameters
        % Poles:
        [RGmaxdB_data_poles_U(:,k,d),RGmaxdB_data_poles_T(:,k,d), ASLLdB_data_poles_U(:,k,d),
            ASLLdB_data_poles_T(:,k,d)] = sas_MaxRG_ASLL(data_poles(k,d),pol,fc,phi_slice,phi_plot,
            steering_angles, N, Nx, taylor_nn_sl,select_MRG_at_sa);
        disp("For pole diameter "+diam_poles(d)+" cm:  Pole @ "+dist_poles(k)+" m solved!  ("+k+"/"+
            length(dist_poles)+")")
        % Poles + shells:
        for s=1:length(legend_shells) % For all types of shells (pole+shell)
            % d+2*(s-1) such that each struct is found correctly!
            [RGmaxdB_data_poles_shells_U(:,k,d,s),RGmaxdB_data_poles_shells_T(:,k,d,s),
                ASLLdB_data_poles_shells_U(:,k,d,s), ASLLdB_data_poles_shells_T(:,k,d,s)] =
                sas_MaxRG_ASLL(data_poles_shells(k, d+2*(s-1)),pol,fc,phi_slice,phi_plot,
                steering_angles, N, Nx, taylor_nn_sl,select_MRG_at_sa);
            disp("For pole diameter "+diam_poles(d)+" cm:  Pole + shell @ "+s+" @ "+dist_poles(k)+
                " m solved!  ("+k+"/"+length(dist_poles)+"), ("+s+"/"+length(legend_shells)+")")
        end
    end
end
disp("Calculations of realized gain and ASLL for steering angles "+min(steering_angles)+" to "+max(
    steering_angles+"° complete!"))

%% Plot results of the antenna without obstruction and with obstructions, with uniform taper and Taylor
    taper
close all; clc

% Select what to plot:
% Tapers to plot:
uniform_taper = 1; taylor_taper  = 0; % true/false
% Plot ref, poles or shells:
ref  = 1; % true/false
poles_plt  = 1;  % true/false
shell1_plt = 0; % true/false
shell2_plt = 0; % true/false
shell3_plt = 0; % true/false
shell4_plt = 0; % true/false
shell2prim_plt = 0; shell3prim_plt = 0; % true/false

% Distances to plot:
% Poles:    % Poles+S1:    % Poles+S2:     % Poles+S3:     % Poles+S4:
p1m  = 1;   p1m_s1  = 1;   p1m_s2   = 1;   p1m_s3   = 1;   p1m_s4    = 1; % true/false
p2m  = 1;   p2m_s1  = 1;   p2m_s2   = 1;   p2m_s3   = 1;   p2m_s4    = 1; % true/false
p3m  = 1;   p3m_s1  = 1;   p3m_s2   = 1;   p3m_s3   = 1;   p3m_s4    = 1; % true/false
p4m  = 1;   p4m_s1  = 1;   p4m_s2   = 1;   p4m_s3   = 1;   p4m_s4    = 1; % true/false
p5m  = 1;   p5m_s1  = 1;   p5m_s2   = 1;   p5m_s3   = 1;   p5m_s4    = 1; % true/false
p10m = 1;   p10m_s1 = 1;   p10m_s2  = 1;   p10m_s3  = 1;   p10m_s4   = 1; % true/false
p20m = 1;   p20m_s1 = 1;   p20m_s2  = 1;   p20m_s3  = 1;   p20m_s4   = 1; % true/false
p30m = 1;   p30m_s1 = 1;   p30m_s2  = 1;   p30m_s3  = 1;   p30m_s4   = 1; % true/false
```

```
% Select angles to plot @ 3 m for S2' and S3':
p3m_s2prim_30deg     = 1; p3m_s3prim_30deg     = 1; % true/false
p3m_s2prim_37dot5deg = 1; p3m_s3prim_37dot5deg = 1;% true/false
p3m_s2prim_45deg     = 1; p3m_s3prim_45deg     = 1;% true/false
% Pole diameters to plot:
p5cm_dp  = 1; p10cm_dp = 1; % true/false

th = data_ref.ax1; % Theta values for reference data (for plt it is assumed that all the data has the same resolution/theta values)
dist_poles_plt = [p1m, p2m, p3m, p4m, p5m, p10m, p20m, p30m]*poles_plt; % Distances to plot (true/false)
diam_poles_plt = [p5cm_dp, p10cm_dp]; % Diameters to plot (true/false)
dist_shell1_plt = [p1m_s1, p2m_s1, p3m_s1, p4m_s1, p5m_s1, p10m_s1, p20m_s1, p30m_s1]; % Distances to plot (true/false)
dist_shell2_plt = [p1m_s2, p2m_s2, p3m_s2, p4m_s2, p5m_s2, p10m_s2, p20m_s2, p30m_s2]; % Distances to plot (true/false)
dist_shell3_plt = [p1m_s3, p2m_s3, p3m_s3, p4m_s3, p5m_s3, p10m_s3, p20m_s3, p30m_s3]; % Distances to plot (true/false)
dist_shell4_plt = [p1m_s4, p2m_s4, p3m_s4, p4m_s4, p5m_s4, p10m_s4, p20m_s4, p30m_s4]; % Distances to plot (true/false)
angl_shell2prim_plt = [p3m_s2prim_30deg, p3m_s2prim_37dot5deg, p3m_s2prim_45deg, 0, 0, 0, 0, 0]; % Angles to plot (true/false)
angl_shell3prim_plt = [p3m_s3prim_30deg, p3m_s3prim_37dot5deg, p3m_s3prim_45deg, 0, 0, 0, 0, 0]; % Angels to plot (true/false)
% Obey to above overwrite:
dist_shell1_plt = dist_shell1_plt*shell1_plt; % Unchanged if plt is true, all set to false if plt is false
dist_shell2_plt = dist_shell2_plt*shell2_plt; % Unchanged if plt is true, all set to false if plt is false
dist_shell3_plt = dist_shell3_plt*shell3_plt; % Unchanged if plt is true, all set to false if plt is false
dist_shell4_plt = dist_shell4_plt*shell4_plt; % Unchanged if plt is true, all set to false if plt is false
angl_shell2prim_plt = angl_shell2prim_plt*shell2prim_plt; % Unchanged if plt is true, all set to false if plt is false
angl_shell3prim_plt = angl_shell3prim_plt*shell3prim_plt; % Unchanged if plt is true, all set to false if plt is false
dist_poles_shells_plt = [dist_shell1_plt; dist_shell2_plt; dist_shell3_plt; dist_shell4_plt; angl_shell2prim_plt; angl_shell3prim_plt]; % (shells, dist_poles)

% Select what type of calculated data to plot:
plttitle_Data_types = ["Realized gain in H-plane for steering angle Ø=0°", "Realized gain in H-plane", "ASLL in H-plane"];
plttitle_Data_type = plttitle_Data_types(1);

if plttitle_Data_type == plttitle_Data_types(1) % RG
    pltxylabel = {'Azimuth angle \theta [°]','Realized gain [dBi]'}; xplt = th;
    yplt_data_ref_U = 20*log10(abs(RG_data_ref_U)); yplt_data_ref_T = 20*log10(abs(RG_data_ref_T));
    yplt_data_poles_U = 20*log10(abs(RG_data_poles_U)); yplt_data_poles_T = 20*log10(abs(RG_data_poles_T));
    yplt_data_poles_shells_U = 20*log10(abs(RG_data_poles_shells_U)); yplt_data_poles_shells_T = 20*log10(abs(RG_data_poles_shells_T));
elseif plttitle_Data_type == plttitle_Data_types(2) % MRG
    pltxylabel = {'Steering angle in H-plane ∅ [°]','Realized gain [dBi]'}; xplt = steering_angles;
    yplt_data_ref_U = RGmaxdB_data_ref_U; yplt_data_ref_T = RGmaxdB_data_ref_T;
    yplt_data_poles_U = RGmaxdB_data_poles_U; yplt_data_poles_T = RGmaxdB_data_poles_T;
    yplt_data_poles_shells_U = RGmaxdB_data_poles_shells_U; yplt_data_poles_shells_T = RGmaxdB_data_poles_shells_T;
elseif plttitle_Data_type == plttitle_Data_types(3) % ASLL
    pltxylabel = {'Steering angle in H-plane ∅ [°]','Realized gain [dBi]'}; xplt = steering_angles;
    yplt_data_ref_U = ASLLdB_data_ref_U; yplt_data_ref_T = ASLLdB_data_ref_T;
    yplt_data_poles_U = ASLLdB_data_poles_U; yplt_data_poles_T = ASLLdB_data_poles_T;
    yplt_data_poles_shells_U = ASLLdB_data_poles_shells_U; yplt_data_poles_shells_T = ASLLdB_data_poles_shells_T;
end
% Plot the selected data!
figure()
plt_gendata_ref_genpoles_genshells(plttitle_Data_type,pltxylabel,yplt_data_ref_U,yplt_data_ref_T,
    yplt_data_poles_U,yplt_data_poles_T,yplt_data_poles_shells_U,yplt_data_poles_shells_T,xplt,N,Nx,
    uniform_taper,taylor_taper,diam_poles,diam_poles_plt,ref,dist_poles,dist_poles_plt,
    dist_poles_shells_plt,legend_shells)
```

A.2 Function *import_hfss_element_patterns()*

```
% Reads in exported (embedded) far field element patterns calculated with
% HFSS. The embedded data is exported using the tab 'Compute Antenna
% Parameters', either by manually exporting embedded solutions of the data
% with the 'Export fields' option, or by letting HFSS create the embedded
% solutions (which however will/might yield numeric rounding errors). For
% the latter option, it is important that the first created antenna element
% (e.g. the first element in the source list in the edit sources tab)
% has the effect 1 W and all others 0 W, otherwise the embedded data will
% become incorrectly scaled.
function [data] = import_hfss_element_patterns(element_list,filename_prefix_text)
% INPUT
% element_list : list of the number if elements, e.g. 1:N where N is the
% number of elements
% filename_prefix_text : string if the file name prefix (excluding the element
% number), e.g. 'exported_HFSS_embedded_element_data_E_'
% OUTPUT
% data : struct with MATLAB readable data
% EXAMPLE
% data = import_hfss_element_patterns(1:N,exported_HFSS_embedded_element_data_E_)
% will read the file for each element:
% exported_HFSS_embedded_element_data_E_1.ffd
% exported_HFSS_embedded_element_data_E_2.ffd
%                 :
% exported_HFSS_embedded_element_data_E_N.ffd
% and, further, create a struct 'data' with:
% data.ax1 = theta axis
% data.ax2 = phi axis
% data.f = frequency
% data.E = E-field, on the form E(element,ax1,ax2,polarisation,frekvens)
% Read in calculated rE-field for all embedded element files (*.ffd):
data.f = [];
for nr_e = element_list
    filename = [filename_prefix_text num2str(nr_e) '.ffd'];
    disp(['Reading file : ' filename]);
    tmp = readHFSSff(filename);
    if isnumeric(tmp)
        error(['File ' filename ' does not exist!']);
    end
    if isempty(data.f)
        data.f = tmp.Frequency;
    else
        if length(data.f) ~= length(tmp.Frequency)
            error(['File ' filename ' contains a different number of frequencies than previous file(s)!'
                ]);
        else
            data.f = tmp.Frequency;
        end
    end
    data.ax1  = tmp.ThetaValues(:);
    data.ax2  = tmp.PhiValues(:).';
    data.E(nr_e,:,:,1,:) = permute(tmp.Eth,[2 1 4 3]);
    data.E(nr_e,:,:,2,:) = permute(tmp.Eph,[2 1 4 3]);
end
% Recalculate to realized gain:
for nr_e = element_list
    data.E(nr_e,:,:,:,:) = sqrt(2*pi*abs(data.E(nr_e,:,:,:,:).^2/376.7)).*exp(1i*angle(data.E(nr_e
        ,:,:,:,:)));
end
% Note that the realized gain for an element array has to be scaled/normalized by
% multiplying it with A_scale = sqrt(1/(sum(abs(A_vec).^2))) where A_vec is the (possibly complex)
% beamforming vector at the read and beamforming stage!
return
```

A.3 Function $readHFSSff()$

```
% Reads the contents of a HFSS far field data file (*.ffd):
function data = readHFSSff(HFSSffdfile)
% INPUT
% HFSSffdfile : HFSS far field data file (*.ffd)
% OUTPUT
% data : the far field data in a MATLAB compatible/readable format
% More specifically, the data is stored in a structure according to:
% data = struct('Frequency',[],'Eth',[],'Eph',[],'ThetaValues',[],'PhiValues',[]);
%
% Both data.Eth and data.Eph will be matrices of the size nPh x nTh x nFr
% where nTh and nPh are the numbers och theta and phi angles respectively
% nd nFr is the number of frequencies
% Eth <=> theta component (a+ib format)
% Eph <=> phi component (a+ib format)
% plot(abs(data.Eth(1,:))) — plots a theta cut for first phi angle
% plot(abs(data.Eth(:,1))) — plots a phi cut for first theta angle
%
% Example: data = readHFSSff('test.ffd')
%
% Initiate data structure
data=struct('Frequency',[],'Eth',[],'Eph',[],'ThetaValues',[],'PhiValues',[]);
fid=fopen(HFSSffdfile,'r');
if fid == -1 % The function returns -1 if the specified file does not exist
    data = -1;
    return
end
% Get theta, phi and frequency info from file
thInfo=textscan(fid,'%f %f %f\n',1);
phInfo=textscan(fid,'%f %f %f\n',1);
frInfo=textscan(fid,'%s %d\n',1);
% Theta values, phi values no frequencies, no theta points, no phi points
thDeg=linspace(thInfo{1},thInfo{2},thInfo{3});
phDeg=linspace(phInfo{1},phInfo{2},phInfo{3});
nFr=frInfo{2};
nTh=thInfo{3};
nPh=phInfo{3};
% Get the data
for ii=1:1:nFr
    allFr=textscan(fid,'Frequency %f\n',1);
    freq(1,ii)=allFr{1};
    allData=textscan(fid,'%f %f %f %f',nTh*nPh);
    reimData(:,:,ii)=cell2mat(allData);
end
data.Eth=reshape(complex(reimData(:,1,:),reimData(:,2,:)),nPh,nTh,nFr);
data.Eph=reshape(complex(reimData(:,3,:),reimData(:,4,:)),nPh,nTh,nFr);
data.Frequency=freq;
data.ThetaValues=thDeg;
data.PhiValues=phDeg;
fclose(fid);
```

A.4 Function $sa\_\_RG\_\_ASLL()$

```
% Convert imported element patterns from HFSS (converted using
% 'import_hfss_element_patterns.m' with 'readHFSSff.m') to realized gain
% and ASLL for a desired steering angle [deg] and slice of phi.
function [RelGain_data,RelGain_data_T, ASLLdB_data, ASLLdB_data_T] = sa_RG_ASLL(data,pol,fc,phi_slice,
    phi_plot,steering_angle, N, Nx, taylor_nn_sl)
% INPUT
% data : the data exported from HFSS using 'import_hfss_element_patterns' and 'readHFSSff'
% pol : the desired polarization (1 (phi) or 2 (theta))
% fc : the single (centre) frequency you want to obtain the results for
% phi_slice : the slice of phi the ASLL should be calculated for
```

```
% phi_plot : the value(s) of phi the realized gain should be calculated for
% steering_angle : the single steering angle the realized gain should be beamformed/steered to
% N : number of elements in the antenna
% Nx: number of elements in one direction (used such that calculations/beamforming is correctly applied
    on matrixes of elements, e.g. for 31x3 antenna)
% (E.g. (N)x(N/Nx) antenna array, for 21x1 then N=Nx=21 whereas for 31x3 then N=93 and Nx=31)
% taylor_nn_sl : specifications of nn and sl for Taylor taper
% OUTPUT
% RelGain_data : the calculated realized gain for uniform taper steered to steering_angle [deg]
% RelGain_data_T : the calculated realized gain for Taylor taper steered to steering_angle [deg]
% ASLL_data : the corresponding calculated ASLL for the uniform taper realized gain
% ASLL_data_T : the corresponding calculated ASLL for the Taylor taper realized gain
plot1 = false; plot2 = false; % Do not plot the resulting realized gain
relative = false; % Relative ASLL not desired
plot0 = false; % Do not plot the ASLL calculation results
th = data.ax1; % Theta values for the realized gain
main_dir = steering_angle; % The steering angle of the realized gain data, specified to be used
% for plot0 in RelGain2AvgSLL(), however not used bc plot0 is set to false
A_mag = ones(1,N); % Obtain magnitude vector for uniform taper
A_mag_T = taylortap_lin(Nx,taylor_nn_sl(1),taylor_nn_sl(2)); % Obtain magnitude vector for Taylor taper
% The magnitude vector is desired to be an array and not matrix, but the
% same beamforming vector should be applied to each row of the antenna,
% e.g. for 31x3 antenna the 31 element vector should be repeated three
% times in an array
if not(N/Nx==1) % Fix Taylor taper if the antenna is a matrix of elements
    A_mag_T_temp = A_mag; % Required temporary save
    for i=1:N/Nx
        A_mag_T = [A_mag_T,A_mag_T_temp]; % Repeat the taper
    end
end
A_vec = []; A_vec_T = []; % Initialize beamforming vector for uniform and Taylor tapers
for n=1:Nx:N % Steer in main_dir direction
    % (n:n+Nx-1) such that the phase shift is applied to the correct
    % elements even if the antenna is a matrix of elements, e.g. 31x3
    A_vec = [A_vec, phase2A(A_mag(n:n+Nx-1),main_dir)];
    A_vec_T = [A_vec_T, phase2A(A_mag_T(n:n+Nx-1),main_dir)];
end
RelGain_data = E2RelGain(data,pol,fc,A_vec,phi_plot,plot1,plot2);
ASLLdB_data = RelGain2AvgSLL(RelGain_data,th,relative,phi_slice,main_dir,plot0);
RelGain_data_T = E2RelGain(data,pol,fc,A_vec_T,phi_plot,plot1,plot2);
ASLLdB_data_T = RelGain2AvgSLL(RelGain_data_T,th,relative,phi_slice,main_dir,plot0);
end
```

A.5 Function $sas\_MaxRG\_ASLL()$

```
% Calculate max realized gain and average side lobe level for all steering
% angles in the array steering_angles, for uniform and Taylor tapers.
function [realized_gain_dB_max,realized_gain_dB_max_T, avg_SLL_dB, avg_SLL_dB_T] = sas_MaxRG_ASLL(data,
    pol,fc,phi_slice,phi_plot,steering_angles, N, Nx, taylor_nn_sl, select_MRG_at_sa)
% INPUT
% data : the data exported from HFSS using 'import_hfss_element_patterns' and 'readHFSSff'
% pol : the desired polarization (1 (phi) or 2 (theta))
% fc : the single (centre) frequency you want to obtain the results for
% phi_slice : the slice of phi the ASLL should be calculated for +
% phi_plot : the value(s) of phi the realized gain should be calculated for
% steering_angles : the steering angles the realized gain should be beamformed/steered to
% N : number of elements in the antenna
% Nx: number of elements in one direction (used such that calculations/beamforming is correctly applied
    on matrixes of elements, e.g. for 31x3 antenna)
% (E.g. (N)x(N/Nx) antenna array, for 21x1 then N=Nx=21 whereas for 31x3 then N=93 and Nx=31)
% taylor_nn_sl : specifications of nn and sl for Taylor taper
% select_MRG_at_sa : true/false, if the max realized gain [dB] should be selected from the actual
    steering angle or from the maximum value of the solution (e.g. from any steering angle such that
    the steering is allowed to be slightly off)
% OUTPUT
```

```
% realized_gain_dB_max : the calculated max realized gain [dB] for uniform taper steered to
    steering_angles [deg]
% realized_gain_dB_max_T : the calculated max realized gain [dB] for Taylor taper steered to
    steering_angles [deg]
% avg_SLL_dB : the corresponding calculated ASLL for the uniform taper max realized gain
% avg_SLL_dB_T : the corresponding calculated ASLL for the Taylor taper max realized gain
plot1 = false; plot2 = false; % Do not plot the resulting realized gain
relative = false; % Relative ASLL not desired
th = data.ax1; % Theta values for the realized gain
realized_gain_dB_max = []; avg_SLL_dB = []; % Initialize
realized_gain_dB_max_T = []; avg_SLL_dB_T = []; % Initialize
for a = 1:length(steering_angles) % For all steering angles
    main_dir = steering_angles(a); % Select steering angle [degrees]
    A_mag = ones(1,N); % Obtain magnitude vector for uniform taper
    A_mag_T = taylortap_lin(Nx,taylor_nn_sl(1),taylor_nn_sl(2)); % Obtain magnitude vector for Taylor
        taper
    if not(N/Nx==1) % Fix Taylor taper if the antenna is a matrix of elements
        A_mag_T_temp = A_mag; % Required temporary save
        for i=1:N/Nx
            A_mag_T = [A_mag_T,A_mag_T_temp]; % Repeat the taper
        end
    end
    A_vec = []; A_vec_T = []; % Initialize beamforming vector for uniform and Taylor tapers
    for n=1:Nx:N % Steer in main_dir direction
        % (n:n+Nx-1) such that the phase shift is applied to the correct
        % elements even if the antenna is a matrix of elements, e.g. 31x3
        A_vec = [A_vec, phase2A(A_mag(n:n+Nx-1),main_dir)];
        A_vec_T = [A_vec_T, phase2A(A_mag_T(n:n+Nx-1),main_dir)];
    end
    Realized_Gain = E2RelGain(data,pol,fc,A_vec,phi_plot,plot1,plot2);
    Realized_Gain_T = E2RelGain(data,pol,fc,A_vec_T,phi_plot,plot1,plot2);
    if select_MRG_at_sa % If the max realized gain should be selected at the current steering angle
        realized_gain_dB_max = [realized_gain_dB_max, 20*log10(abs(Realized_Gain(find(main_dir==th),find
            (phi_slice==phi_plot))))]; % Select the realized gain value at the desired th
        realized_gain_dB_max_T = [realized_gain_dB_max_T, 20*log10(abs(Realized_Gain_T(find(main_dir==th
            ),find(phi_slice==phi_plot))))]; % Select the realized gain value at the desired th
    else % If the max realized gain should be selected at any steering angle (e.g. it can be slightly
        off)
        realized_gain_dB_max = [realized_gain_dB_max, max(20*log10(abs(Realized_Gain(:,find(phi_slice==
            phi_plot)))))];
        realized_gain_dB_max_T = [realized_gain_dB_max_T, max(20*log10(abs(Realized_Gain_T(:,find(
            phi_slice==phi_plot)))))];
    end
    % Check avg side lobe level for the solution:
    AvgSideLobeLvl = RelGain2AvgSLL(Realized_Gain(:,find(phi_slice==phi_plot)),th,relative,phi_slice,
        main_dir,false);
    AvgSideLobeLvl_T = RelGain2AvgSLL(Realized_Gain_T(:,find(phi_slice==phi_plot)),th,relative,phi_slice
        ,main_dir,false);
    avg_SLL_dB = [avg_SLL_dB, AvgSideLobeLvl];
    avg_SLL_dB_T = [avg_SLL_dB_T, AvgSideLobeLvl_T];
end
end
```

A.6 Function *E2RelGain()*

```
% Convert imported element patterns from HFSS (converted using
% 'import_hfss_element_patterns.m' with 'readHFSSff.m') to realized gain
% and plot (2D and/or 3D) if desired. An embedded element pattern referrs to
% the pattern of one element obtained as it's effect is set to 1 W whilst all
% other elements' effect is set to 0 W.
function Realized_Gain = E2RelGain(data,pol,fc,A_vec,phi_plot,plot1,plot2)
% INPUT
% data : the data exported from HFSS using 'import_hfss_element_patterns' and 'readHFSSff'
% pol : the desired polarization (1 (phi) or 2 (theta))
% fc : the (centre) frequency you want to obtain the results for
```

```
% A_vec : amplitude vector, possibly modified in amplitude in phase
% phi_plot : vector of the phi values (degrees) you want to plot, e.g. [0, 10, 20, 30]
% plot1 : true/false, if you want to plot realized gain in 2D or not
% plot2 : true/false, if you want to plot realized gain in 3D or not
% OUTPUT
% Realized_Gain : the realized gain, for the phi values that were selected
th = data.ax1;  % Theta values [degrees]
phi = data.ax2; % Phi values [degrees]
f = data.f; % Frequency values [Hz]
A_scale = sqrt(1/(sum(abs(A_vec).^2))); % Array scaling factor
for i=1:length(th) % For all theta
    for j=1:length(phi_plot) % For all (desired) phi (e.g. select not all/a few for fast computation)
        % Sum field of all N elements for all theta and all (desired) phi values
        export_vector = data.E(:,i,find(phi==phi_plot(j)),pol,find(f==fc)); % Extract imported data
        export(i,j) = sum(A_vec.*export_vector.')*A_scale; % Apply beamforming with A_vec, sum and scale
    end
    if plot2==true && not(length(phi_plot)==length(phi)) % In case a 3D plot is desired
        for j_=1:length(phi) % For ALL phi (slightly slower computation for all phi)
            % Sum field of all N elements for all theta and all phi values
            export_vector2 = data.E(:,i,j_,pol,find(f==fc)); % Again, extract imported data
            export2(i,j_) = sum(A_vec.*export_vector2.')*A_scale; % OBS, .' for nonconjugate transpose
        end
    end
end
Realized_Gain = export; % To return
if plot1==true % Plot 2D?
    figure(1)
    for idx=1:length(phi_plot) % Plot result of the selected phi values
        plot(th,20*log10(abs(export(:,idx))),'LineWidth',1); hold on; grid on; % 2D rectangular
    end
    legend("$\phi =$ "+phi_plot+"°",'Location','southwest');
    xlabel('Azimuth angle $\theta$ [°]'); ylabel('Realized gain [dBi]'); title('Realized gain')
end
if plot2==true % Plot 3D?
    Realized_Gain = export2; % In case more data was collected, return it all
    figure(2)
    PatternPlotOptions(Transparency=0.1);
    colorbar;
    caxis([-62.5 25]);
    %patternCustom(20*log10(abs(export2.')),th,phi,"CoordinateSystem","polar",Slice="phi",SliceValue=0);
          % 2D polar
    patternCustom(20*log10(abs(export2.')),th,phi); % 3D polar
end
end
```

A.7 Function *RelGain2AvgSLL()*

```
% Calculate the average sidelobe level (ASLL) of the realized gain for one
% slice of phi.
function AvgSideLobeLvldB = RelGain2AvgSLL(Realized_Gain,th,relative,phi_slice,main_dir,plot0)
% INPUT
% Realized_Gain : array of realized gain
% th : the theta values for the array (e.g. data.ax1)
% relative : true/false for relative ASLL or not
% phi_slice : the phi value, only required for specification in plot!
% main_dir : direction [deg] the beam is steered into, only required for
% specification in plot!
% plot0 : true/false, if the result should be plotted or not
% OUTPUT
% AvgSideLobeLvl : scalar of the average sidelobe level
mat_blue = [0, 0.4470, 0.7410]; mat_red = [0.8500, 0.3250, 0.0980]; % Plot colors
if not(size(Realized_Gain,2)==1) % Make sure only an array of realized gain is input
    disp('The size of RelGain should be (th,1), e.g. only for one phi value!')
end
% Find max value. This should be equal to main beam. But with beamforming
```

```
% this might not be the case (e.g. low gain in desired direction if
% nulling), so let's also overwrite with our desired direction...
[max_val,max_idx] = max(Realized_Gain);
% From the maximum idx, loop through all gain values in both directions
% until a minimum is found, then you know the width of the main lobe from
% null to null
RG_left = 20*log10(abs(flip(Realized_Gain(1:max_idx,1)))); % Max and left side of it
RG_right = 20*log10(abs(Realized_Gain(max_idx:end,1))); % Max and right side of it
null_idx_r = []; null_idx_l = []; % Initialize
for r=1:length(RG_right)-1 % Loop through right side and find null idx
    if RG_right(r+1)>RG_right(r)
        null_idx_r = r-1;
        break; % Breaks out of for-loop (bc idx found)
    end
end
if isempty(null_idx_r) % If no right side lobes
    null_idx_r = length(RG_right)-1; % Last idx
end
for l=1:length(RG_left)-1 % Loop through left side and find null idx
    if RG_left(l+1)>RG_left(l)
        null_idx_l = l-1;
        break; % Breaks out of for-loop (bc idx found)
    end
end
if isempty(null_idx_l) % If no left side lobes
    null_idx_l = length(RG_left)-1; % Last idx
end
% Remove main lobe from original vector (with the realized gain)
% Also store it for plot to check that it was removed correctly
RG_mainlobe = Realized_Gain((max_idx-null_idx_l):max_idx+null_idx_r,1);
th_mainlobe = th((max_idx-null_idx_l):max_idx+null_idx_r,1);
RG_sidelobes_l = Realized_Gain(1:(max_idx-null_idx_l));
RG_sidelobes_r = Realized_Gain(max_idx+null_idx_r:end);
th_sidelobes_l = th(1:(max_idx-null_idx_l));
th_sidelobes_r = th(max_idx+null_idx_r:end);
RG_sidelobes = [RG_sidelobes_l;RG_sidelobes_r]; % Array of the sidelobes
AvgSideLobeLvldB = mean(20*log10(abs(RG_sidelobes))); % in dB
if not(relative)
    if plot0
        figure()
        plot(th_mainlobe,20*log10(abs(RG_mainlobe)),'LineWidth',1,'Color',mat_blue); hold on; grid on;
        plot(th_sidelobes_l,20*log10(abs(RG_sidelobes_l)),'LineWidth',1,'Color',mat_red); hold on;
        plot(th_sidelobes_r,20*log10(abs(RG_sidelobes_r)),'LineWidth',1,'Color',mat_red); hold on;
        plot(th,ones(1,length(th))*AvgSideLobeLvldB,'--','LineWidth',1,'Color',mat_red)
        xline(main_dir,'--g','LineWidth',1); hold on;
        xlabel('Azimuth angle \theta [°]'); ylabel('Realized gain [dBi]'); title(
            "Average side lobe level ASLL = "+AvgSideLobeLvldB+" dBi for \phi ="+phi_slice+"°");
    end
end
if relative
    RG_mainlobe_rel = RG_mainlobe/max_val;
    RG_sidelobes_l_rel = RG_sidelobes_l/max_val;
    RG_sidelobes_r_rel = RG_sidelobes_r/max_val;
    AvgSideLobeLvl_rel = mean(20*log10(abs(RG_sidelobes/max_val)));
    if plot0
        figure()
        plot(th_mainlobe,20*log10(abs(RG_mainlobe_rel)),'LineWidth',1,'Color',mat_blue); hold on; grid
            on;
        plot(th_sidelobes_l,20*log10(abs(RG_sidelobes_l_rel)),'LineWidth',1,'Color',mat_red); hold on;
        plot(th_sidelobes_r,20*log10(abs(RG_sidelobes_r_rel)),'LineWidth',1,'Color',mat_red); hold on;
        plot(th,ones(1,length(th))*AvgSideLobeLvl_rel,'--','LineWidth',1,'Color',mat_red); hold on;
        xlabel('Azimuth angle \theta [°]'); ylabel('Relative realized gain [dBi]'); title(
            "Relative average side lobe level ASLL = "+AvgSideLobeLvl_rel+" dBi for \phi ="+phi_slice+"°")
            ;
    end
    AvgSideLobeLvldB = AvgSideLobeLvl_rel;
end
end
```

A.8 Function *phase2A()*

```
% Apply phase shift to magnitude vector for antenna beamforming
function A_lin_phase_shift = phase2A(A,steering_angle)
% INPUT
% A: amplitude/magnitute vector for antenna array
% steering_angle : the angle the vector should be steered to (linearly)
% OUTPUT
% A_lin_phase_shift : linearly phase shifted antenna beamforming array
N = length(A); % Number of elements in one direction
d_phase = rad2deg(pi*sin(deg2rad(steering_angle)))*ones(1,N); % Array with phase shifts
for k=1:N % For all elements
    A(k)=A(k)*exp(1j*deg2rad(-d_phase(k)*(k-1))); % Apply its phase shift
end
A_lin_phase_shift = A; % A_vec
end
```

A.9 Function *taylortap_lin()*

```
% Calculate excitations for a linear group antenna with equal distances between the antenna elements
function excitation=taylortap_lin(length,nn,sl)
% INPUT
% length: Number of antenna elements
% nn : number of equally high sidelobes before the attenuation is increased
% sl : Number of dB the first sidelobe should be attenuated with
% Example:
% taylortap_lin(21,3,31) : Calculates the excitation for 21 elements where
% the first 3 sidelobes on each side are attenuated with 31 dB in relation
% to the main lobe, after which the following sidelobes are attenuated
% further with sin(x)/x
% OUTPUT
% excitation : the resulting excitation (as described above)
[m,q]=meshgrid(1:(nn-1),1:(nn-1)); % Suitable help matrixes for the calculation
% Check if the number of elements is odd or even and assign to N
if mod(length,2)==1 % If odd
        N=(length-1)/2;
else % If even
        N=length/2;
end
% See Villeneuves Taylorpatterns for discrete arrays:
ny=10^(sl/20);
uo=cosh(1/(length-1)*log(ny+sqrt(ny^2-1)));
phi=2*acos(cos((2*q-1)*pi/(2*(length-1)))/uo);
omega=nn*pi/(length*acos(1/uo*cos((2*nn-1)*pi/(2*(length-1)))));
phiprim=omega*phi;
% Help functions used for calculation of E:
A=sin(m*pi/length-phiprim/2).*sin(m*pi/length+phiprim/2);
B=sin((m-q)*pi/length).*sin((m+q)*pi/length);
% Remove zero elements in B:
zero_elements = find( B==0 );
B(zero_elements) = 1;
% Calculate E:
E=length*(-1).^m(1,:).*prod(A)./(sin(m(1,:)*pi/length).*sin(2*m(1,:)*pi/length).*prod(B));
% Help functions used for calculation of E0:
C=(sin(phiprim/2)).^2;
D=(sin(q(:,1)*pi/length)).^2;
% Calculate E0:
E0=length*prod(C(:,1))/prod(D);
% Create suitable matrixes of m and E:
M=ones(length,1)*m(1,:);
E=ones(length,1)*E;
% Calculate the excitation (different dependent on if the number of elements is even or odd)
if mod(length,2)==1 % If odd
```

```
        [p]=meshgrid(-N:N,1:nn-1);
        excitation=1/length*(E0+2*sum((E.*cos(p'.*M*2*pi/length))'));
else % If even
        [p]=meshgrid(-(N-1):N,1:nn-1);
        excitation=1/length*(E0+2*sum((E.*cos((p'-0.5).*M*pi/N))'));
end
% Normalize the excitation:
excitation=excitation/max(excitation);
```

A.10 Function *plt_gendata_ref_genpoles_genshells()*

```
% A general shell/almost GUI that can be used to plot combinations of
% different/desired types of calculated data for different antenna setups.
% The shell can be used or modified as desired but the intended setup is to input:
% 1) One antenna + no obstruction reference (e.g. antenna result without obstruction)
% 2) A general number of antenna + obstruction references (e.g. antenna result with poles in front of it)
% 3) Any amount of shells with the same general number (e.g. for the same amount of pole distances) of antenna + obstruction + shell solutions (e.g. antenna result with poles with shell in front of it)
function plt_gendata_ref_genpoles_genshells(plttitle_Data_type,pltxylabel,yplt_data_ref_U,yplt_data_ref_T,yplt_data_poles_U,yplt_data_poles_T,yplt_data_poles_shells_U,yplt_data_poles_shells_T,xplt,N,Nx,uniform_taper,taylor_taper,diam_poles,diam_poles_plt,ref,dist_poles,dist_poles_plt,dist_poles_shells_plt,legend_shells)
% INPUT
% plttitle_Data_type(1) : string which first letter should be capitalized, denoting what type of data is input (e.g. "Realized gain"). The string is only used to specity the data type in the plot title.
% pltxylabel{1:2} : Vector with two strings used only for xlabel (pltxylabel{1}) and ylabel (pltxylabel{2})
% yplt_data_ref_U(length(realized gain)) : Array of uniform taper reference data to be plotted on yaxis
% yplt_data_ref_U(length(realized gain)) : Array of Taylor taper reference data to be plotted on yaxis
% yplt_data_poles_U(:,k,d) : Multiple dim. matrix of uniform taper pole data to be plotted on yaxis. The matrix is of size (length(realized gain), length(dist_poles), length(diam_poles))
% yplt_data_poles_T(:,k,d) : Multiple dim. matrix of Taylor taper pole data to be plotted on yaxis. The matrix is of size (length(realized gain), length(dist_poles), length(diam_poles))
% yplt_data_poles_shells_U(:,k,d) : Multiple dim. matrix of uniform taper pole+shell data to be plotted on yaxis. The matrix is of size (length(realized gain), length(dist_poles), length(diam_poles), nr of shells)
% yplt_data_poles_shells_T(:,k,d) : Multiple dim. matrix of Taylor taper pole+shell data to be plotted on yaxis. The matrix is of size (length(realized gain), length(dist_poles), length(diam_poles), nr of shells)
% xplt(:) : Array of data to be plotted along the xaxis (e.g. theta values or steering angles)
% N: number of elements in the antenna (used for specification in plot text)
% Nx: number of elements in one direction (used for specification in plot text, used such that calculations/beamforming is correctly applied on matrixes of elements, e.g. for 31x3 antenna)
% (E.g. (N)x(N/Nx) antenna array, for 21x1 then N=Nx=21 whereas for 31x3 then N=93 and Nx=31)
% uniform_taper : single true/false, if uniform taper solutions should be plotted or not
% taylor_taper : single true/false, if Taylor taper solutions should be plotted or not
% diam_poles() : array of the solutions' pole diameters with unit cm (e.g. [5, 10];)
% diam_poles_plt() : array of trues/falses of the same length as diam_poles controlling which pole diameter(s) should be plotted
% ref : single true/false, controlling if the reference (e.g. antenna without obstruction should be plotted)
% dist_poles() : array of the solutions' pole distances with unit m (e.g. [1, 2, 3, 4, 5, 10, 20, 30];)
% dist_poles_plt() : array of trues/falses of the same length as dist_poles controlling which pole distance(s) should be plotted
% dist_poles_shells_plt() : array of trues/falses of the same length as dist_poles controlling which pole+shell distance(s) should be plotted
% legend_shells() : array of string(s) specifying the type(s) of shell(s), e.g. absorbent "FGM125", which will be included in plot legend text
% Default matlab colors:
mat_blue = [0, 0.4470, 0.7410];
mat_red = [0.8500, 0.3250, 0.0980];
mat_yellow = [0.9290, 0.6940, 0.1250];
mat_purple = [0.4940, 0.1840, 0.5560];
mat_green = [0.4660, 0.6740, 0.1880];
```

```
mat_lightblue = [0.3010, 0.7450, 0.9330];
mat_winered = [0.6350, 0.0780, 0.1840];
mat_pink = [1, 0.6667, 0.8980];
mat_colors = [mat_blue; mat_red; mat_yellow; mat_purple; mat_green; mat_lightblue; mat_winered; mat_pink];
% Default matlab colors, somewhat lighter:
mat_blue_light = [122, 202, 255]/255;
mat_red_light = [255, 165, 126]/255;
mat_yellow_light = [255, 226, 158]/255;
mat_purple_light = [198, 132, 212]/255;
mat_green_light = [197, 235, 148]/255;
mat_lightblue_light = [200, 238, 255]/255;
mat_winered_light = [224, 123, 142]/255;
mat_pink_light = [255,211,242]/255;
mat_colors_light = [mat_blue_light; mat_red_light; mat_yellow_light; mat_purple_light; mat_green_light; mat_lightblue_light; mat_winered_light; mat_pink_light];
% Desired plot variations:
lw_diam_poles = [1, 1.5]; % Linewidth for 5 cm and 10 cm pole diameter plots
ls_shells = {'--','-.',':'}; % Linestyle for the different shells
figure() % Plot results
set(gcf,'Color','w');
if uniform_taper == true % If uniform taper should be plotted
    legend_taper_type_U = "uniform (U)"; % For plt title
    legend_poles_U = []; % Initialize (this will become a string)
    legend_poles_shells_U = []; % Initialize (this will become a string)
    legend_poles_polesshells_U = []; % Initialize (to store diam_poles in correct order)
    if ref % If the reference should be plotted
        plot(xplt,yplt_data_ref_U,'LineWidth',1,'Color','k'); hold on; grid on;
        legend_ref_U = "U: No obstruction";
    else % If not, exclude the legend
        plot(NaN,NaN); legend_ref_U = "";
    end
    for d=1:length(diam_poles) % For all pole diameters
        if diam_poles_plt(d) % If the pole diameter should be plotted
            for i=1:length(dist_poles) % For all pole distances
                if dist_poles_plt(i) % If the pole distance should be plotted
                    plot(xplt,yplt_data_poles_U(:,i,d),'LineWidth',lw_diam_poles(d),'Color',mat_colors(i,:)); hold on; grid on;
                    legend_i = "U: "+diam_poles(d)+" cm diameter pole @ "+dist_poles(i)+" m"; % Create the legend for distance i
                else % If not, exclude the legend
                    plot(NaN,NaN); legend_i = "";
                end
                legend_poles_U = [legend_poles_U, legend_i]; % Save the legend for distance i
            end
            for s=1:length(legend_shells) % For all pole shells
                for a=1:length(dist_poles) % For all pole distances
                    if dist_poles_shells_plt(s,a) % If the pole shell should be plotted
                        plot(xplt,yplt_data_poles_shells_U(:,a,d,s),'LineStyle',ls_shells{s},'LineWidth',lw_diam_poles(d),'Color',mat_colors_light(a,:)); hold on; grid on;
                        legend_a = "U: "+diam_poles(d)+" cm diameter pole + "+legend_shells(s)+" @ "+dist_poles(a)+" m"; % Create the legend for distance a
                    else % If not, exclude the legend
                        plot(NaN,NaN); legend_a = "";
                    end
                    legend_poles_shells_U = [legend_poles_shells_U, legend_a]; % Save the legend for distance a
                end
            end
            legend_poles_polesshells_U = [legend_poles_polesshells_U, legend_poles_U, legend_poles_shells_U]; % For a desired order in legend
            legend_poles_U = []; legend_poles_shells_U = []; % Clear for next pole diameter
        end
    end
else
    legend_taper_type_U = []; legend_ref_U = []; legend_poles_polesshells_U = []; % Required to define a variable for the implemented plot setup
end
if taylor_taper == true % If Taylor taper
    legend_taper_type_T = "Taylor (T)"; % For plt title
```

```
97      legend_poles_T = []; % Initialize (this will become a string)
98      legend_poles_shells_T = []; % Initialize (this will become a string)
99      legend_poles_polesshells_T = []; % Initialize (to store diam_poles in correct order)
100     if ref % If the reference should be plotted
101         plot(xplt,yplt_data_ref_T,'LineWidth',1,'Color','k'); hold on; grid on;
102         legend_ref_T = "T: No obstruction";
103     else % If not, exclude the legend
104         plot(NaN,NaN); legend_ref_T = "";
105     end
106     for d=1:length(diam_poles) % For all pole diameters
107         if diam_poles_plt(d) % If the pole diameter should be plotted
108             for i=1:length(dist_poles) % For all pole distances
109                 if dist_poles_plt(i) % If the pole distance should be plotted
110                     plot(xplt,yplt_data_poles_T(:,i,d),'LineWidth',lw_diam_poles(d),'Color',mat_colors(i
                            ,:)); hold on; grid on;
111                     legend_i = "T: "+diam_poles(d)+" cm diameter pole @ "+dist_poles(i)+" m"; % Create
                            the legend for distance i
112                 else % If not, exclude the legend
113                     plot(NaN,NaN); legend_i = "";
114                 end
115                 legend_poles_T = [legend_poles_T, legend_i]; % Save the legend for distance i
116             end
117             for s=1:length(legend_shells) % For all the pole shells
118                 for a=1:length(dist_poles) % For all the pole distances
119                     if dist_poles_shells_plt(s,a) % If the pole shell should be plotted
120                         plot(xplt,yplt_data_poles_shells_T(:,a,d,s),'LineStyle',ls_shells{s},'LineWidth'
                                ,lw_diam_poles(d),'Color',mat_colors_light(a,:)); hold on; grid on;
121                         legend_a = "T: "+diam_poles(d)+" cm diameter pole + "+legend_shells(s)+" @ "+
                                dist_poles(a)+" m"; % Create the legend for distance a
122                     else % If not, exclude the legend
123                         plot(NaN,NaN); legend_a = "";
124                     end
125                     legend_poles_shells_T = [legend_poles_shells_T, legend_a]; % Save the legend for
                            distance a
126                 end
127             end
128             legend_poles_polesshells_T = [legend_poles_polesshells_T, legend_poles_T,
                    legend_poles_shells_T]; % For a desired order in legend
129             legend_poles_T = []; legend_poles_shells_T = []; % Clear for next pole diameter
130         end
131     end
132 else
133     legend_taper_type_T = []; legend_ref_T = []; legend_poles_polesshells_T = []; % Required to define a
            variable for the implemented plot setup
134 end
135 if uniform_taper & taylor_taper
136     legend_taper_type = "uniform (U) and Taylor (T)"
137 else
138     legend_taper_type = [legend_taper_type_U,legend_taper_type_T]; % Either U or T
139 end
140 % Plot the results:
141 legend([legend_ref_U,legend_poles_polesshells_U,legend_ref_T,legend_poles_polesshells_T]); xlabel(
        pltxylabel{1}); ylabel(pltxylabel{2});
142 title(plttitle_Data_type+" for "+N/Nx+"x"+Nx+" waveguide antenna with "+legend_taper_type+" taper");
        grid minor
```

B

Ansys HFSS simulation setups and meshing methods

In this chapter, Section B.1 details how the implemented antenna and obstruction simulation described in Section 3.2 was constructed with the use of a FE-BI boundary around the array antenna and a FE-BI boundary or an IE region around the obstruction. Further, Section B.2 describes the setup for simulating an obstruction and incident electromagnetic waves in an enclosed environment using the PML boundary and a Lattice Pair. Lastly, Section B.3 details the simulation setup for characterisation of any absorbent using the Floquet Port and Lattice Pairs.

B.1 Antenna and obstruction simulation setup using the FE-BI boundary and the IE region

For simulation of an antenna as an obstruction is located far away from it in vacuum, a FE-BI boundary can be placed around the antenna and, depending on the material of the obstruction (e.g. if it is a single structure of PEC or not), an IE region or a FE-BI boundary can be assigned to/around the obstruction which enables faster meshing and, thus, a significantly reduced simulation time. Figure B.1 exemplifies an Ansys HFSS model setup (e.g. the one implemented in this project) for which the described setup is useful. In this section, an introduction is given of Ansys HFSS's IE region and FE-BI boundary, both of which were implemented for the antenna and obstruction simulations described in Section 3.2.

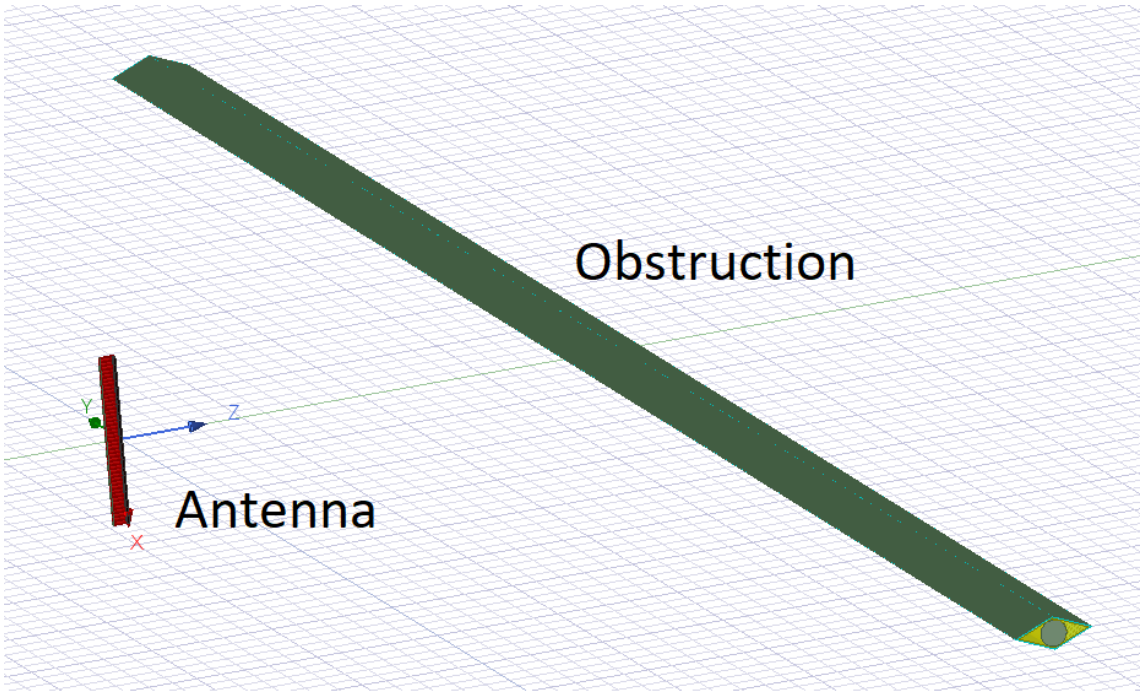

Figure B.1: Exemplification of an Ansys HFSS model with an array antenna and an obstruction located at a large distance (e.g. 1 m) from it in vacuum, for which the meshing and simulation time can be reduced significantly through the implementation of a FE-BI boundary around the antenna and an IE region or a FE-BI boundary around the obstruction.

Implementation of the IE region is effective when meshing a singular large object made out of PEC/metal. In order to assign an IE region to a structure, the structure's surface or all of its faces should be selected, after which "Assign Hybrid" followed by "IE Region" should be selected after right-clicking in the Modeler Window. Please note that for this option to appear, the project solution type needs to be defined as "HFSS with Hybrid and Arrays". Distinct from the IE region that can only be applied to a singular PEC structure, the FE-BI boundary can handle meshing structures that consist of multiple components of different materials and varying sizes. Hence, a FE-BI boundary is, for instance, useful for meshing and simulating array antennas or other more complicated arbitrary designs. A FE-BI boundary is assigned around an object by covering it with an air box, selecting all the faces of the air box, right-clicking in the Modeler Window and selecting "Assign Boundary" followed by "FE-BI...", as exemplified by Figure B.2. When adding the air box around the object to measure, in order for the software to make accurate calculations, Ansys HFSS recommends adding extra air space around the object such that there is at least a twentieth of the simulation wavelength ($\lambda/20$) from the object to the air box edge everywhere.

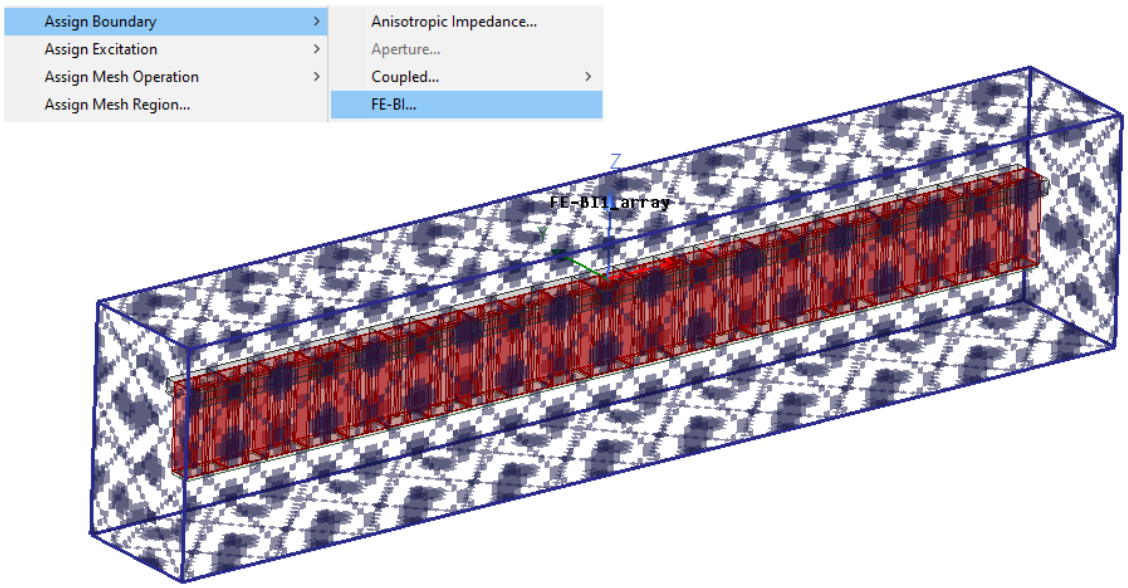

Figure B.2: Exemplification of how to assign a FE-BI boundary to all the selected faces of an added air box around the model to measure/simulate.

B.2 Setup for simulating waves incident on an obstruction in an enclosed environment using the PML boundary and a Lattice Pair

The PML boundary is short for "perfectly matched layer" due to it being a complex anisotropic fictitious material that fully absorbs all incident electromagnetic waves. This makes the PML boundary suitable for terminating electromagnetic waves that travel outside a defined space. As can be seen in the multiple electric field plots shown in Section 3.3, the electric waves do not reflect on the walls of the enclosing PML boundary, allowing the scattering at the obstruction to be observed without interference. This section details how to employ the Ansys HFSS simulation environment used to simulate and plot the resulting electric fields as incident waves were propagated toward an obstruction.

In order to reduce the required simulation time and computer power (e.g. the required computer or server RAM and CPU performance), the obstruction length in the y-axis was reduced to a couple of mm (e.g. instead of the full 5 m pole length employed in this project) after which the obstruction shortened in the y-axis and its surrounding volume were covered in an air cell and, later, extended into infinity with the use of a Lattice Pair. Reducing both the simulation time and increasing the accuracy of the results with the use of the Lattice Pair was possible through enclosing the simulation environment with boxes and assigning them to be a uniform PML boundary, and through adding top and bottom sheets covering the upper and lower xz-planes of the whole model (e.g. including the PML boundary boxes) that the Lattice Pair sides could be assigned to, respectively. As PML boundaries are perfectly matched layers the enclosing boundaries were perfect absorbents for the

incoming electromagnetic waves and, hence, the added PML boundaries did not introduce scattering at the edges. Hence, the affect that the obstruction had on the incident waves could be evaluated in a completely enclosed environment.

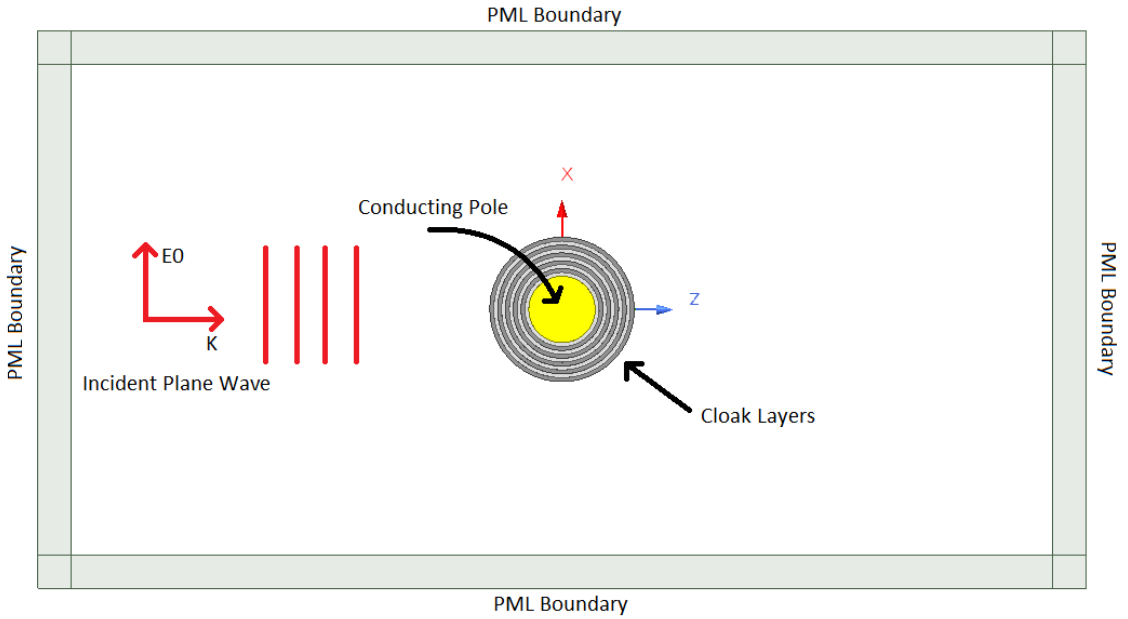

Figure B.3: Setup of the PML boundaries and the incident plane wave in HFSS for simulation of the resulting electric fields as incident waves were propagated towards an obstruction. The figure exemplifies illumination of a wave with incident angle 0° with TM/horizontal illumination where the electric field is polarized along the x-axis. Instead, for TM/vertical polarization, the electric field vector should be modified to be aligned with the y-axis/the cylinder axis.

Figure B.3 describes the setup of the PML boundaries enclosing the volume of the obstruction and its surrounding environment and the setup of the incident plane wave. For all simulations/shown incident wave plots in this project, the air cell was designed with the area 400×800 mm^2 in the xz-plane and with heights ranging from 5 to 10.5 mm in the y-plane. The simulation environment can be seen in 3D in figure B.4, which also details how the Lattice Pair, respectively, should be assigned to the top and bottom xz-plane sheets covering the whole model.

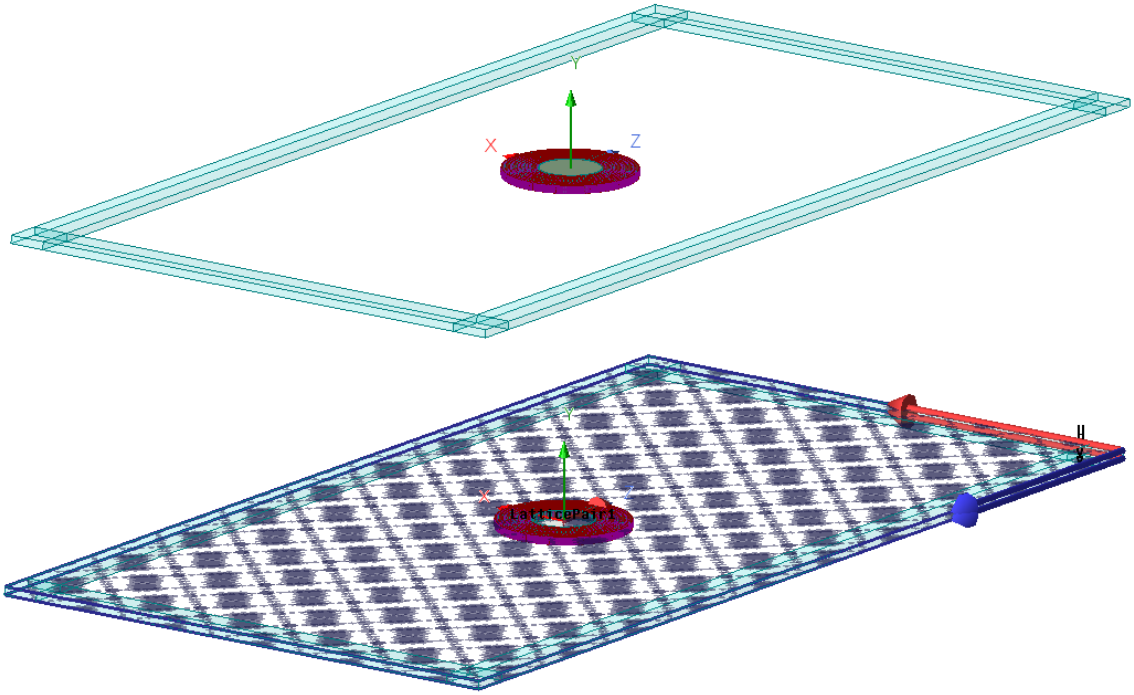

Figure B.4: Visualization of the set up environment in Ansys HFSS for simulation of the resulting electric fields as incident waves were propagated toward the obstruction at ($x = 0$, $y = 0$, $z = 0$). The top image shows the environment as a whole and the bottom image visualizes how the Lattice Pair sides were assigned to the top and bottom xz-plane sheets covering the whole model, respectively.

B.3 Simulation setup for absorbent characterisation using the Floquet Port and Lattice Pairs

This section details how to simulate a material in Ansys HFSS such that the material's absorbent characteristics can be evaluated. Figure B.5 shows the absorbent material to be characterised (in pink) placed in front of a PEC box (in green) corresponding to an obstruction as well as an added longer air box (in transparent white) in front of the absorbent box. Further, Figure B.5 exemplifies how a Floquet Port should be assigned to the short end of the air box, and how linked Lattice Pairs should be placed on each opposite long sides of the model (e.g. including the sides of the air box, the absorbent box and the PEC box). Using this setup, incident waves of the desired polarization can be simulated for different incident angles, such that the measured reflected effect ratio S_{11} [dB] at the Floquet Port corresponds to the return loss RL=$|S_{11}|$. Hence, through viewing the simulated return loss RL=$|S_{11}|$ for the polarization of interest with respect to the frequency for different incident angles, the absorbent characteristics can be evaluated as low reflections (e.g. less than -10 dB) imply high absorption by the material and a high return loss of more than 10 dB. Figure B.5 exemplifies the simulation of the FGM-125 absorbent, as described in Section 3.3.1, for which the defined dimensions are specified in Table B.1, however it follows that an absorbent of any thickness or material can be simulated

through extending the absorbent into the negative z-direction and moving the PEC box along with it, and through defining the desired material properties.

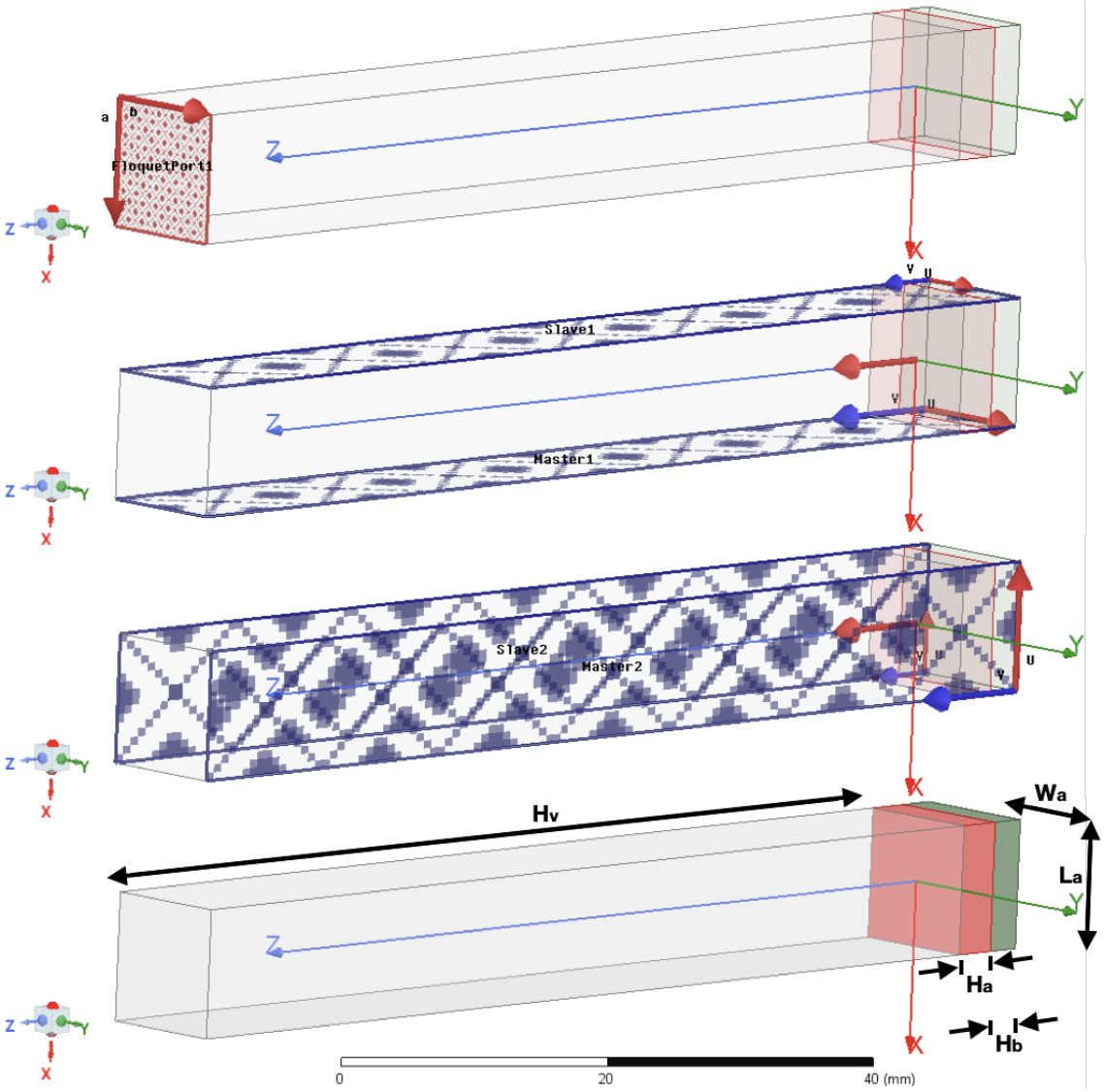

Figure B.5: Visualization of the Ansys HFSS setup for simulating the reflected effect in the air box (in transparent white) from an absorbent (in pink) in front of a PEC box (in green), together with specifications of how to employ the Floquet Port and Lattice Pairs.

Table B.1: Specification of the FGM-125 absorbent reflected effect simulation's dimensions, defined in Figure B.5.

Variable	L_a	W_a	H_a	H_b	H_v
Value [mm]	10.0	10.0	3.18	2.70	80.0

C

Meta-material parameter extraction

This chapter describes how the relative permittivity ϵ_r and relative permeability μ_r of an arbitrary material can be retrieved through the use of both Ansys HFSS and MATLAB [3][4]. Through simulating a slab of the material in Ansys HFSS such that its S-parameters S_{11} and S_{21} can be obtained (e.g. corresponding to return loss RL=$|S_{11}|$ and insertion loss IL=$|S_{21}|$, respectively), the results can be exported to MATLAB for calculations of the material's electromagnetic properties. In order to simulate the material in Ansys HFSS, the material has to be encapsulated by an air box as exemplified in Figure C.1 for a split ring resonator [1]. Further, the opposite air box faces aligned with the xz-plane and with the xy-plane need to be assigned perfect electric boundaries and perfect magnetic boundaries, respectively, as described by Figure C.2.

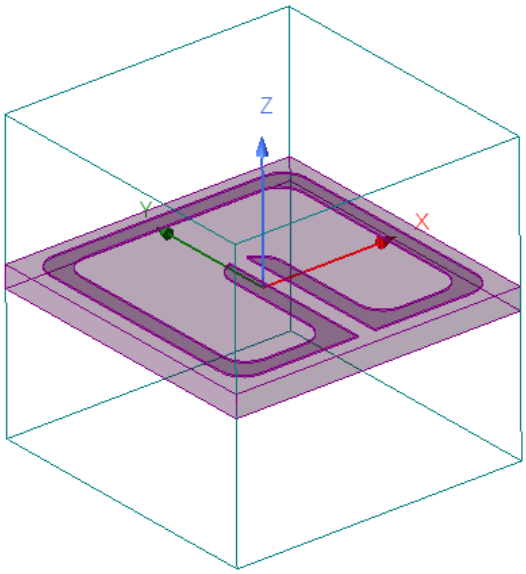

Figure C.1: Visualization of how to encapsulate the material in an air box for later S-parameter extractions and calculations of the material's electromagnetic properties. The material exemplified in the figure is an emulated split ring resonator [1][4].

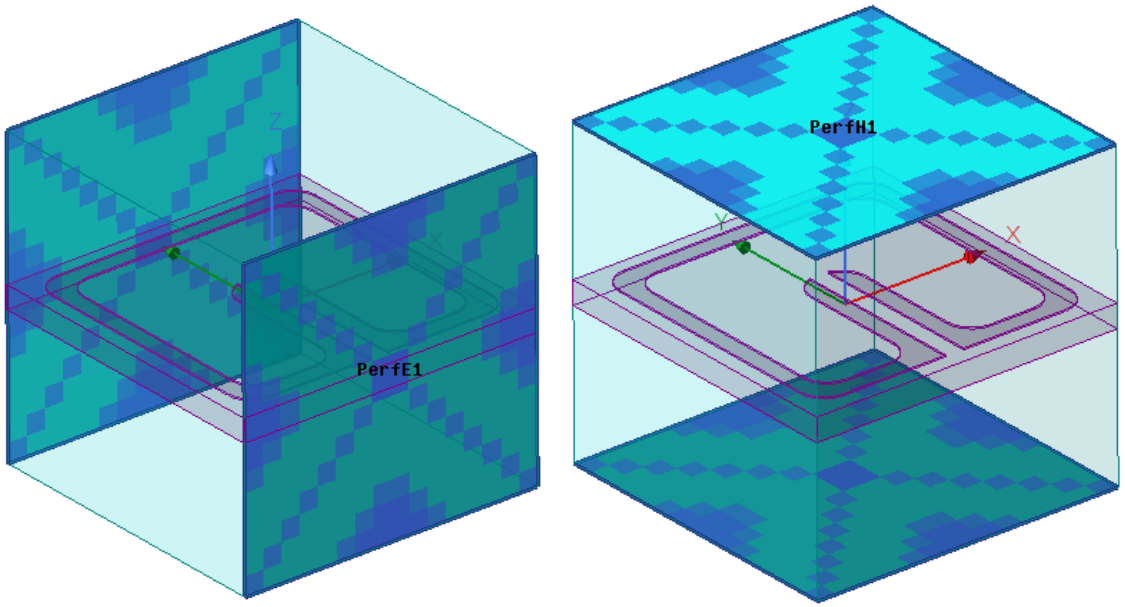

a) Perfect electric boundary on air cell faces. b) Perfect magnetic boundary on air cell faces.

Figure C.2: Assignment of boundaries on opposite air cell faces [4].

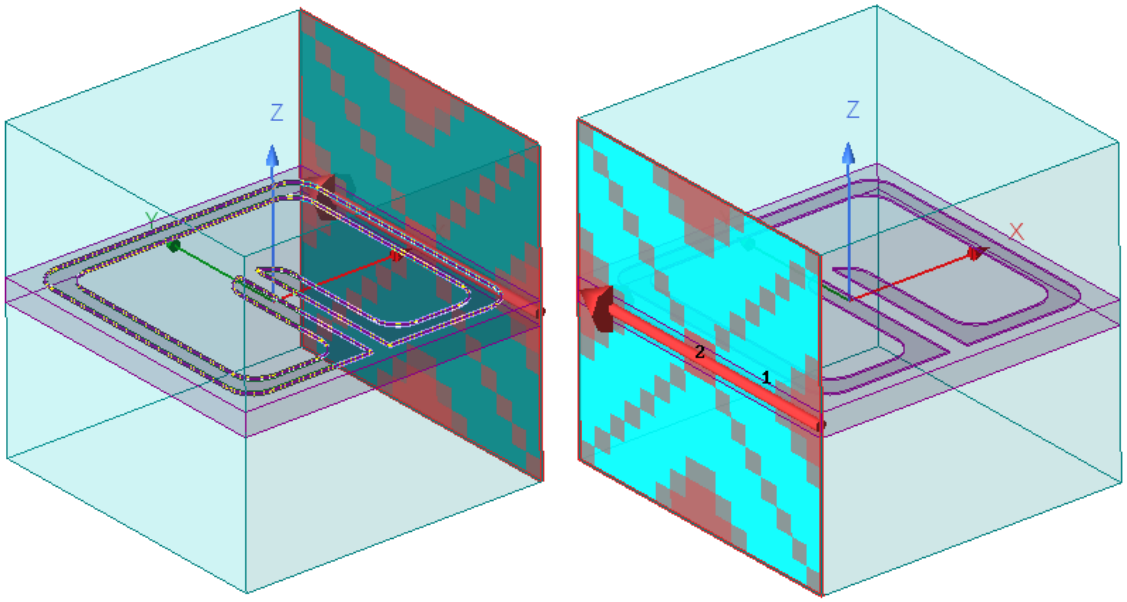

a) Wave port 1. b) Wave port 2.

Figure C.3: Assignment of wave port 1 and 2 on the opposite air box faces aligned with the yz-plane on the negative and positive x-axis, respectively [4].

After the Ansys HFSS simulation is finished, the S-parameters S_{11} and S_{21} need to be exported to MATLAB for calculations of the relative permittivity ϵ_r and the relative permeability μ_r. For instance, the S-parameters can be exported through plotting the desired results in Ansys HFSS, right-clicking in the plot window and exporting the desired file format (e.g. *.csv) after selecting the tab "Export...". Having exported the required S-parameters to MATLAB, the relative permittivity

ϵ_r and relative permeability μ_r can be obtained through first calculating the material's impedance z and refractive index n. The impedance z of the material can be calculated as

$$z = \pm\sqrt{\frac{(1+S_{11})^2 - S_{21}^2}{(1-S_{11})^2 - S_{21}^2}} \tag{C.1}$$

where S_{11} and S_{21} are the simulated and extracted S-parameters. Further, having obtained the material impedance z from Equation (C.1) the refractive index n of the material can be calculated as

$$n = \frac{1}{dk_0}\Big(\ln\left(e^{jndk_0}\right) + 2m\pi - j\ln\left(e^{indk_0}\right)\Big) \tag{C.2}$$

where m is an integer, d [m] is the largest length dimension in the unit cell and where

$$k_0 = \frac{2\pi}{(c/f_c)} \tag{C.3}$$

is the wave number in free space (e.g. the wavelength of the signal divided by the speed of light in vacuum), c is the speed of light in vacuum and f_c is the simulated frequency implemented for the S-parameter solution [4]. Further, the relation

$$e^{jndk_0} = \frac{S_{21}}{1 - S_{11}(z-1)/(z+1)} \tag{C.4}$$

can be used to calculate the remaining quantity in Equation (C.2). The integer variable m in Equation (C.2) affecting only the real part of the refractive index is used for compensation of the phase shift inside the simulated material with a modulo 2π due to it being difficult to measure the absolute phase shift in the material [3]. For simulations of the split ring resonator visualized in Figure C.1, the integer was selected to be $m = 0$ because the air cell encapsulating the simulated material was much smaller than the simulated wavelength. The consequence of selecting an unsuitable value of m is incorrect results of the refractive index and, hence propagating errors as other quantities are calculated (and, thus, if for some reason larger material slabs are to be simulated, more thought is required for the selection of this parameter). Having calculated quantities for the impedance z and the refractive index n, the relative permittivity ϵ_r and the relative permeability μ_r can be calculated as

$$\epsilon_r = \frac{n}{z} \tag{C.5}$$

and

$$\mu_r = nz \tag{C.6}$$

respectively. Figure C.4 shows examples of calculated real and imaginary refractive index n and impedance z of the material simulated in Ansys HFSS for a range of frequencies, and Figure C.5 shows the resulting real and imaginary relative permittivity ϵ_r and relative permeability μ_r.

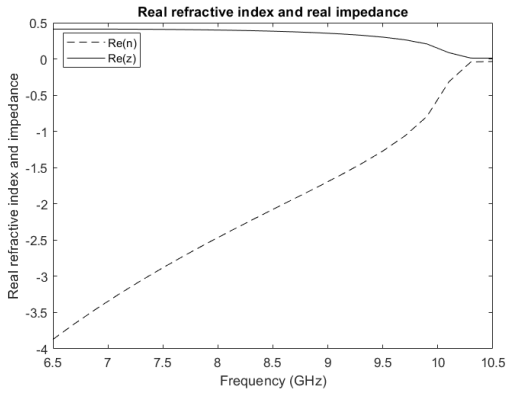

a) Real n and z.

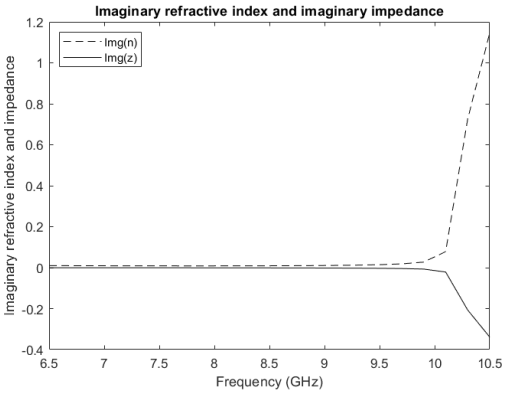

b) Imaginary n and z.

Figure C.4: Calculated real and imaginary refractive index n and impedance z over a range of frequencies for which the S-parameters S_{11} and S_{21} were simulated and exported from Ansys HFSS.

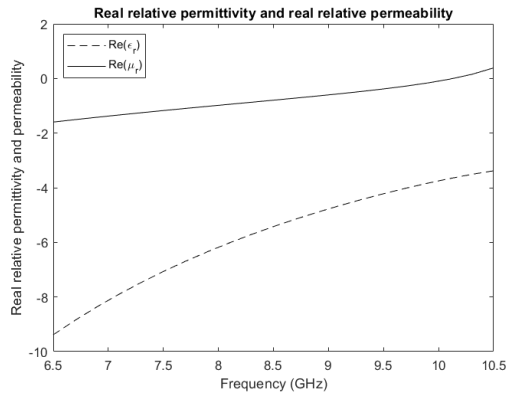

a) Real ϵ_r and μ_r.

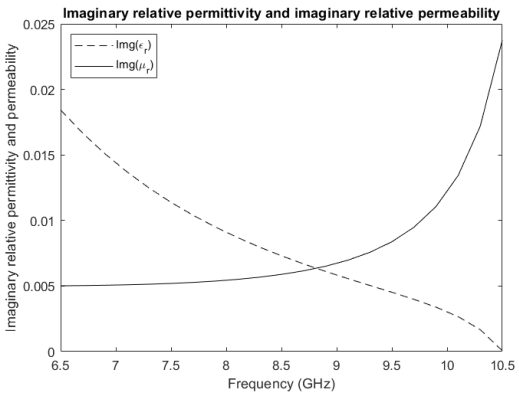

b) Imaginary ϵ_r and μ_r.

Figure C.5: Calculated real and imaginary relative permittivity ϵ_r and relative permeability μ_r over a range of frequencies for which the S-parameters S_{11} and S_{21} were simulated and exported from Ansys HFSS.

DEPARTMENT OF ELECTRICAL ENGINEERING
CHALMERS UNIVERSITY OF TECHNOLOGY
Gothenburg, Sweden
www.chalmers.se

CHALMERS
UNIVERSITY OF TECHNOLOGY